Speckle Tracking for Cardiac Strain Imaging in Ultrasound Imaging and Contrast Enhancement in Photoacoustic Imaging

by

Congxian Jia

A dissertation submitted in partial fulfillment
of the requirements for the degree of
Doctor of Philosophy
(Biomedical Engineering)
in The University of Michigan
2010

Doctoral Committee:

Professor Matthew O'Donnell, Chair
Professor Douglas C. Noll
Professor Jonathan M. Rubin
Professor J. Brian Fowlkes
Associate Professor Theodore J Kolias
Associate Professor Cheri Xiaoyu Deng
Assistant Professor Kang Kim, University of Pittsburgh

2010

To My Family

ACKNOWLEDGMENTS

I am very grateful to all the people who have accompanied, helped, guided, and encouraged me throughout my graduate years to get to this point.

First and foremost, I would like to thank my parents, my brother and all my relatives in China for their unconditional love and endless support. You are always the source of my strength no matter who I am and where I am.

I would like to thank my thesis advisor, Matthew O'Donnell, for the privilege to work with him during my graduate studies. I thank Matt for giving me an opportunity to gather strength to start this journey when I was heartbroken and felt lost in my world. I thank Matt for being my role model in my life time, for being passionate for work, patient for teaching, incisive for discussion, insightful for leadership, active for life, honest for ethics and kind for people. I feel so fortunate to have experienced how Matt can shape and speed the world surrounding him.

I would like to thank and acknowledge Professor Douglas C. Noll, Professor Jonathan M. Rubin, Professor J. Brian Fowlkes, Professor Theodore J Kolias, Professor Cheri Xiaoyu Deng and Professor Kang Kim for their time and guidance, serving on my dissertation committee. I thank Professor Douglas C. Noll for all the help and support from BME department of University of Michigan through these years when Matt was not around and when we were in Seattle. I thank Professor Kang Kim, Professor Jonathan M. Rubin, Professor Theodore J

Kolias, Professor William F. Weitzel for maintaining and attending elasticity group meetings, giving great discussion and suggestion for my research, and continuous support especially when Matt is not around. I thank Professor Cheri Xiaoyu Deng for sharing lab space with us. I am very grateful to the support from all the staff members in BME Department of University of Michigan and the Bioengineering Department of University of Washington, especially Jane MacKie, Maria E. Steele, Tonya Y. Thompson, Ruth Halsey, Chuck Nicholas, Ruth Woods, Shirley Alcantara, Danielle Elias, Lina Nguyen, Norbert Berger, Sonia Honeydew, Jeff Magula, and Andrea Perkins for their help and coordination.

I would like to sincerely thank all the wonderful BUL labmates and friends for their help, support and joy from both research and ordinary life. I would like to particular thank my lab partner Ragnar Olafsson for doing rabbit experiments overnights through cold winter to hot summer, sharing the frustrating and successful moments during the experiment, providing wonderful suggestions and teaching me how to use instruments. I thank Hua Xie for her introduction and guidance to elasticity imaging, her valuable advice and sincere care for my life and future. I thank Sheng-Wen Huang for his guidance in experiments, sincere advice for life, assistance during the transition from Ann Arbor to Seattle, and support in a new environment. I thank Xunchang Chen for his help in elasticity imaging, Timothy Hall for all his help during experiments in Ann Arbor, Marwa Zhody, Todd Erpelding, Christine Tse, Becca Booi, Zhen Xu, Jessi Parsons for their help and suggestions in the lab, intergrating me in to their life circle and providing a home feeling since I first stepped into the BUL Lab, Tzu-Yin Wang for

hosting me and communicating needed information, Zhen-Zhen Fang for transferring material, Yang Hou for communicating information, Chi Hyung Seo, Lingyun Huang, Janet F. Eary and Jinjun Xie for their support and suggestion in the experiments and dissertation. I would also like to thank Russ Witte, Shai Ashkenazi, Frank Winterroth, Yan Shi, Tak Buma, Kyle Hollman, Javier de Ana, Fong Ming Hooi, Michael S . Richards, Binh Tran, Adam D Maxwell, Yun Zhou, Alex Chiao, Ronald E Kumon, Yohan Kim, and the rest of the BULlies, for their kindness, support and encouragement through all these years. I would like to thank my collaborates Yongdong Jin, Xiaoge Hu, and Xiaohu Gao from the University of Washington, Ping Yan, Albert J. Sinusas, Donald P. Dione and James S. Duncan from Yale Univeristy, and Qifeng Wei and Karl Thiele from Philips Medical Systems for their support, help, suggestion and data acquisition for both phantom and animal experiments in this research. I would like to thank Nancy Roeser and Kimberly Ives for their generous help and training for animal experiments, Adam Lauver and Erin Booth for their help with the Langendorff setup, Marty Schlicht for lending the pressure transducer and Prof. Shuichi Takayama for letting me has access to the equipments in his lab

I would like to thank the National Institutes of Health Grants HL-082640, HL-67647, HL-68658, CA-109440, EB-003451, BME Department of University of Michigan, Bioengineering Department of University of Washington for their funding support. I thank Philips for supplying ultrasound scanners.

TABLE OF CONTENTS

LIST OF FIGURES

LIST OF APPENDICES

Chapter 1 INTRODUCTION

1.1 Speckle Formation

Ultrasound (US) and photoacoustic (PA) imaging, as coherent imaging modalities, are characterized by the presence of speckle [1]. Speckle is a random, deterministic granular structure produced as a result of constructive or destructive interference of backscattered echoes from scatterers in the imaged object [2]. In ultrasound, speckle arises when many scatterers exist in one resolution cell and their size is small compared to an incident wavelength. The amplitude of fully developed speckle in a B-mode image follows a Rayleigh distribution.

Speckle formation and statistics are directly related to the details of the imaging system and underlying tissue microstructure [3]. The speckle size in the axial direction is inversely proportional to the interrogating pulse bandwidth, and in the lateral direction is proportional to the transducer F# and the incident wavelength [2]. The formation of speckle structure is affected by local ultrasonic scattering determined by the acoustic properties of tissue structure. The microstructure, such as the composition of cells or blood vessels, is believed to contribute to the acoustic scattering. When the underlying tissue moves, the motion repositions the scatterer structure, causing the speckle to move along with it [4]. Speckle structure in ultrasound images represents a spatial marker

that can be used to track tissue motion [3]. Speckle tracking is a newly developed technique to measure this speckle motion and then characterize the mechanical properties of tissue [5].

1.2 Image-based Motion Tracking Methods

When an object in continuous motion is recorded by a sequence of images, motion information such as the new location or deformation of the object can be estimated by analyzing these recorded images using imaged-based motion tracking methods. These methods are appealing for non-invasive, quantitative assessment of human internal organs such as heart. They leverage recent advances in medical imaging technologies, such as computed tomography and diagnostic ultrasound, and can significantly impact clinical diagnosis and treatment. Image-based motion tracking methods can be sorted into two categories: feature-based tracking methods and texture-based tracking methods [6].

Feature-based tracking methods need to extract some features, which can be reliably detected across many images, and estimate the motion of the object by gathering motion information from these features. Features can be derived from surface shape properties such as local curvatures [7] or edges [8] and some keypoints with scale-invariant properties [9]. Texture-based tracking methods consider the texture or appearance of the object in one image to be highly correlated with the texture of the corresponding object in consecutive images. Regional motion of the object in the reference image can be estimated by

searching the most similar texture in the following image using a predefined similarity measurement such as the cross correlation coefficient or the sum of squared differences. Texture-based tracking methods can provide denser displacement estimates than feature-based methods since in the latter, only a limited number of well-defined features can be extracted in a typical biomedical image.

Speckle tracking can be categorized as a texture-based method. Speckle structure is the texture carrying motion information of the underlying tissue or object. Both US and PA imaging are formed from coherent summation of scattered sound waves originally transmitted from an US probe or generated by thermal expansion due to local light absorption. As discussed in Section 1.1, both US and PA images exhibit speckle. By recording an US or PA image sequence, underlying tissue motion can be estimated using speckle tracking. In this dissertation, we demonstrate that the derived motion information can be used to non-invasively assess the contractility of the heart wall in US imaging and increase the specific contrast of contrast agents in PA imaging.

1.3 Speckle Tracking for Cardiac Strain Imaging

1.3.1 Myocardial Ischemia

Coronary heart disease (CHD) is one of the leading causes of death in the United States. It often results from insufficient blood (or oxygen) supply to the myocardium due to a coronary artery narrowed by extensive plaque accumulation. Plaque rupture of a coronary artery also leads to the formation of a

blood clot partially or completely blocking the artery. Immediately after occlusion, myocardial cells begin to experience ischemia and then injury. Prolonged occlusion will result in necrosis of myocardial cells, or myocardial infarction (MI) [10] as illustrated in Fig. 1.1.

After an injury to the left ventricle (LV), the ventricular mass, chamber size and shape (wall thinning, chamber dilation and increased ventricular sphericity [11]), and heart function will change. This alteration is called LV remodeling. Ultimately, LV remodeling will diminish contractile (systolic) function, reduce stroke volume, decrease the performance of the LV, and may lead to LV dysfunction. In 2006 alone, CHD mortality was 425,425, causing about 1 of every 6 deaths in the United States. Among CHD mortality, 33% died due to MI [12].

At the cellular level, LV remodeling pathologically involves three stages: myocyte hypertrophy, fibroblast hyperplasia accompanied by an increase in collagen deposition, and structural remodeling of myocardial scar tissue. Each stage leads to the structural rearrangement of myocardial muscle components in the LV and consequently changes in mechanical properties such as myocardial muscle stiffness [13-16]. During the first stage, myocardial fibers in the infarcted region lose their ability to generate systolic force, converting from an active, force-generating material to a passive, viscoelastic material throughout the cardiac cycle. Systolic circumferential and longitudinal shortening and radial thickening of normal myocardium is replaced by circumferential and longitudinal stretching and radial thinning of diseased myocardium [16]. Therefore, even though mechanical properties such as stiffness haven't changed within a short

time of ischemia, the regional internal deformation pattern in the heart wall changes because of myocardial muscles' conversion from active contraction to passive stretching. When the infarction enters the fibrotic phase, new collagen deposition becomes the primary determinant of structural and mechanical changes. The available evidence suggests infarct stiffness increases and peaks during this phase, roughly correlating with collagen content. This elevated stiffness is confirmed by the passive pressure-segment length relationship reported by Theroux [16]. The slope varies from six to nine times control values depending on end diastolic pressure [16, 17]. In the third phase, collagen content deposition in the infarct slows but cross-linking increases. However, the mechanical properties of the infarct do not continue to rely on collagen content. Changes in mechanical properties of myocardial muscles result in changes of their deformation ability, reducing pump function of the LV and leading to death from heart failure.

MIs are categorized into two types in terms of location: transmural infarction and subendocardial infarction. Subendocardial infarctions involve about 30% of the ventricular wall thickness, while transmural infarctions occupy 75% to 90% of the wall thickness. Because endocardial and subendcardial zones are the least perfused region of the heart wall, they are the most vulnerable to ischemia. Acute myocardial infarction usually begins subendocardially and then extends to a transmural infarction [18]. Accurate analysis of the size and transmurality of myocardial injury and MI is critical to evaluate and manage patients with CHD,

and provide important prognostic information about adverse LV remodeling post-MI.

1.3.2 Current Technologies for Assessing Myocardial Function

Early identification of ischemic myocardium and monitoring of LV remodeling can offer important diagnostic and therapeutic information. A number of diagnostic procedures have been used for this purpose. They include the electrocardiogram (ECG), biochemical markers, 2-D echocardiography, magnetic resonance imaging (MRI) and radionuclide imaging. Electrocardiography (ECG) is a simple, easily accessible and painless procedure. However, more than 50% of patients with MI show nonspecific findings on the initial ECG obtained [19]. Routine biochemical confirmation is usually made. For example, MB isoenzyme of creatine kinase (MBCK) has about 90% specificity after 6 hours of MI [20]. But its sensitivity may not be satisfactory less than 4 hours from the onset of chest pain [19]. Both these methods provide global information and cannot be used to analyze regional function of the heart wall.

Radionuclide imaging, 2-D echocardiography and MRI have played important roles in cardiac global and regional function measurements through wall thickness analysis based on epicardial and endocardial boundary shape and contour. Radionuclide imaging requires an injection of radioactive material to the patients. This modality has a relatively poor spatial resolution. For example, a gated single photon emission computed tomography (SPECT) myocardial perfusion imaging (MPI) has a spatial resolution about 10 mm [21]. Radionuclide

imaging's temporal resolution is not high. Gated with the patient's ECG, 8-16 frames for a single cardiac cycle can be collected through multiple heart beats.

Cardiac MRI has an in-plane spatial resolution of about 1-2 mm and provides a good contrast in cardiac anatomy. But MRI's image sequence is usually acquired over multiple cardiac cycles gated with the ECG. Respiratory motion artifacts can degrade image quality. A breath-hold duration of 15-20s is needed, which is often hard to maintain in sick patients. Two-dimensional echocardiography is more commonly used in the management of MI because it is inexpensive, portable, and bed-side accessible. It evaluates global and regional myocardial function by visualizing the entire ventricular myocardium in different tomographic planes at a frame rate that typically exceeds 100 frames per heart cycle. The spatial resolution is about 1 mm along the beam propagation direction and about 1– 3 mm along the azimuthal direction, varying with depth for a central frequency of 3.5 MHz. However, routine clinical evaluation of regional myocardial function is still dependent on the visual assessment of wall motion and frequently overestimates the true extent of the area of infarction in both experimental models [22, 23] and humans [24]. Therefore, true quantitative analysis about the size and transmural extent of MI is lacking for these three imaging methods.

To overcome the above limitation, myocardial strain and strain rate (SR) have been proposed as appealing clinical metrics to more precisely and quantitatively analyze regional LV deformation and contractility, assess myocardial injury, and monitor LV remodeling [25]. There are two types of contraction producing internal deformation in myocardial muscle: active and

passive. As described above, during acute MI, the mechanical properties of infarcted muscle haven't changed. But the infarcted muscle loses its active contractility and only contracts passively, which leads to changes of the internal deformation pattern. In addition, the typical contraction of normal myocardial muscles in the short interval during systole characterized by SR will be lost as well. Therefore, strain and SR [26] can be used to differentiate between the active contraction of live muscle and passive contraction of dead muscle.

During remodeling post MI, the stiffness of chronic infarcted muscles increases because of changes in its structure as described above and further affects the passive mechanical deformation pattern of the heart wall. Therefore, the strain pattern of heart wall can also be used to evaluate changes in diseased myocardial muscles' mechanical properties compared to surrounding healthy myocardial muscles during different stages of the post-MI period.

MRI tagging and US strain imaging are two competing noninvasive approaches to evaluate myocardial deformation and potentially quantify injury and remodeling. 2-D and 3-D tagged MRI images have been used to measure deformation by tracking the tag grid lines created at a certain position at one point in the cardiac cycle. The spatial resolution of the strain computed from the tagged images is determined by the distance between two adjacent tags [27]. In 3-D MRI tagging, the tag line distance in plane is typically 6-7 mm; the distance between contiguous image slices is 7-10 mm [28]. So the spatial resolution of strain calculated from MRI tagging is relatively low. In addition, tag lines decay with time, which degrade strain estimates. Data acquisitions required to

assemble 3-D information in MRI require multiple breath-holds through several heart cycles. So MRI cannot resolve short-lived, highly dynamic cardiac events and suffers from an inherent tradeoff between high spatial resolution and high signal-to-noise ratio (SNR) [29, 30].

Unlike MRI, US imaging is a bedside scanning tool with real-time display, relative low cost, and excellent spatial resolution [31]. This makes it an attractive choice as a clinical imaging modality. US strain and SR have been proposed to measure myocardial deformation through the heart cycle. Compared to MRI tagging, ultrasound strain imaging can achieve a better spatial resolution and lead to more precise estimates of the size and transmural extent of MI to help better guide disease management in the clinic.

1.3.3 Ultrasound Strain Imaging

Ultrasound strain or strain rate imaging has been proposed to quantitatively assess regional myocardial contractility [32-36], and non-invasively detect myocardial ischemia and infarction to overcome observer-dependency related to interpreting wall motion anomalies [37-38]. Auto-correlation based tissue Doppler imaging (TDI) [33, 34, 36] and cross-correlation based 2-D speckle tracking (ST) [35, 39, 40] are two major ultrasound techniques to measure myocardial strain for this application [38, 41-42]. Both have been widely studied in the past two decades.

Auto-correlation based TDI was first introduced to image myocardial velocity by McDicken et al. in 1992 [43]. TDI-derived strain rate using the velocity

gradient to quantify wall thickness was first introduced by Fleming et al. in 1994 [32] and regional myocardial contraction by Uematsu et al. in 1995 [33]. This method has been investigated in phantom experiments [44], animal experiments [34] and human experiments [45, 46], demonstrating the feasibility of clinical application for myocardial ischemia or infarction detection [47].

Cross-correlation based phase-sensitive 2-D ST using radio-frequency (RF) signals was developed by several groups [48-53] for tumor detection, such as breast cancer, and later introduced to assess myocardial function [35, 54, 55]. It has been evaluated in a simulated heart [39], phantom experiments [56], animal experiments [40, 57], and human experiments [58].

TDI is generally recognized as a 1-D method sensitive to beam angle. Its strain estimation suffers from decorrelation due to lateral or elevational motion and low strain signal-to-noise ratio (strain SNR, the ratio of mean strain to standard deviation of strain error [49]) because a high pulse repetition frequency (PRF) is required to avoid aliasing on velocity estimation [40, 41, 46, 59, 60]. 2-D ST was introduced to mitigate these problems by estimating 2-D in-plane displacements with moderate frame rates. In addition to these general considerations, the details of TDI and 2-D ST are fundamentally different and directly affect estimation accuracy, even of the same parameters. As detailed in Chapter 2, this dissertation will demonstrate that traditional TDI derived instantaneous axial normal strain and/or strain rate has a larger variance and accumulated axial normal strain has greater errors due to incorrect registration than 2-D ST.

For instantaneous axial strain or strain rate, TDI measures the average velocity of myocardial tissue passing through a fixed spatial position (e.g., image pixel labeled with red box in Fig. 1.2 (a) and (b)) using multiple beams over a certain time interval. Note: Fig.1.2 and Fig. 2.1 in chapter 2 are the same one. The partial overlap of signals scattered from the same tissue at different time instants, as illustrated by Fig. 1.2 (a), results in decorrelation along the axial direction in addition to decorrelation due to motion transverse to the beam direction. Consequently, it exhibits larger variance in velocity estimation based on autocorrelation even with spatial averaging to match 2-D ST estimation resolution. Unlike TDI, 2-D ST estimates the displacement (or velocity) at the identical pixel by following the same speckle pattern centered on that pixel from a reference frame through time (*cf*. Fig. 1.2 (b)). Speckle formation and statistics are directly related to the details of the imaging system and underlying tissue microstructure. Speckle structure represents a spatial marker that can be used to track tissue motion [4]. Therefore, as illustrated in Section II in Chapter 2, even if motion is only along the beam propagation direction, tracking a speckle pattern over time rather than averaging at a fixed position enhances signal similarity and leads to more accurate displacement estimates.

For accumulated axial normal strain, additional error is produced using TDI due to incorrect spatial registration. Traditional TDI simply sums the averaged strain rates of different myocardial tissue passing through a pixel. The result is defined as natural strain. Because accumulation cannot follow the same tissue from the beginning of the observation time through the total time of accumulation,

deformation estimated in this way cannot be unambiguously referenced to the first frame (Lagrangian point of view) or referenced to the current accumulated frame (Eulerian point of view). Using the formula shown in Section II of Chapter 2, TDI natural strain can be converted to approximate Lagrangian strain. But the error will be large for large strains, as is the case at the end of systole [43]. 2-D ST can significantly reduce this accumulation error because it can correctly register the same myocardium by recording the in-plane position over the estimation interval. Accumulated results can be presented in either Lagrangian or Eulerian frameworks.

An alternative approach to strain imaging using 2-D non-Doppler speckle tracking can minimize the above limitation of Doppler-based methods by estimating in-plane 2-D strain components. Non-Doppler speckle tracking can be divided into two categories according to different input data: phase-insensitive speckle tracking using B-mode gray-scale images [61, 62] and phase-sensitive speckle tracking using RF data [35, 36, 39, 50, 52, 53, 63]. Phase-insensitive 2-D tracking has poor precision in both dimensions whereas phase-sensitive tracking has good precision along the propagation direction and relatively poor precision orthogonal to the propagation direction [49].

It has been shown that phase-insensitive tracking can overcome Doppler based TDI-derived strain imaging's angle dependence in animal experiments [62] [64] and clinical patient investigations [61, 65, 66]. Without phase information, however, the results depend highly on spatial and temporal smoothing, and

traces of strain components only represent the overall behavior of large segments.

In contrast, phase-sensitive speckle tracking using RF images can refine tracking results along the propagation direction using the calculated phase zero-crossing position [49], and this improvement in one direction leads to higher accuracy in the accumulated results in both directions. Therefore, phase-sensitive speckle tracking not only can overcome the angle limitation of Doppler-based methods, but also provide more accurate results with higher spatial resolution for each strain component, an important feature to derive coordinate-independent principal axes and strains based on the principal stretches along these axes. The accuracy and higher spatial resolution is valuable to detect the transmurality of myocardial ischemia or infarction. In this study, phase-sensitive speckle tracking is used to estimate myocardial deformation.

In continuum mechanics, deformation at one point in a solid body can be fully characterized by strains based on the principal stretches along the principal axes, where a proper coordinate rotation is applied to eliminate all shear components [67]. These parameters are only related to the deformation status at that point and are theoretically independent of coordinates. In Chapter 3, we propose to use in-plane strains based on the principal stretches along the principal axes to characterize the contractility of heart muscle and the directional change of the principal axes to detect abnormal motion.

Note that strains [31, 68] obtained by deriving the principal stretches from the right Cauchy deformation tensor are different from the principal strains [69] calculated using the finite Lagrange deformation tensor. The latter overestimates or underestimates the fractional deformation compared to the original length in large strain situations, such as the accumulated deformation at the end of the systole, as shown in the Appendix.

Estimation of strains based on principal stretches and their principal axes is independent of the coordinate system or the orientation of the probe. These strains are derived from the eigenvalues and eigenvectors of the right Cauchy deformation tensor. The tensor captures the deformation status at that point and moment regardless of the probe's orientation. However, the accuracy and precision of estimated strains and their principal axes depend on the probe's orientation. Because displacements used to estimate the right Cauchy deformation tensor are estimated by multi-dimensional, phase-sensitive speckle tracking, they exhibit higher variance in the lateral direction than the axial direction due to the availability of phase information only along the ultrasound propagation direction [70]. Unequal estimation variances between displacements along the beam and those perpendicular to it lead to the unequal estimation variances of the components in the right Cauchy deformation tensor. Therefore, the accuracy and precision of estimated strains and their principal axes derived from the right Cauchy deformation tensor depend on the direction of ultrasound propagation relative to the principal axes.

Another challenging issue with cardiac elasticity imaging is that heart motion is 3-D and complex. Currently available 2-D elasticity imaging techniques are limited by significant out-of-imaging plane motion. 3-D tracking algorithms have also been developed recently in different groups [59 and 71]. However, the frame rate of cardiac data acquisition using current 2-D probes is not high enough. It's not easy to evaluate tracking algorithms on complex cardiac motion clinically. A well-controlled experimental setup is needed to validate all algorithms, such as 3-D speckle tracking, for displacement and strain estimation. In Chapter 4, a LV phantom [72] was constructed using Polyvinyl alcohol (PVA) cryogel and integrated with a pulsatile pump in combination with a pressure meter. We have compared 2-D and 3-D speckle tracking [73] performance on the LV phantom and a 3-D LV simulation.

1.4 Speckle Tracking for Contrast Enhancement in PA Imaging

1.4.1 PA Imaging

PA imaging is also called optocoustic or thermoacoustic imaging. It's a new medical imaging modality combining optical absorption with ultrasound imaging based on the photothermal effect. PA imaging can measure optical absorption of the imaged object determined by the optical absorption spectrum in tissue using acoustic signal detection while retaining the high resolution and penetration of US imaging [74-78]. When a tissue with optical absorption is illuminated by a pulse laser, the heat deposited by absorbing this electromagnetic energy causes

a rapid thermoelastic expansion in the tissue. Acoustic waves are generated due to this expansion and detected by an ultrasound transducer for imaging [74-77].

The above photoacoustic wave generation can be mathematically described as

$$\left(\nabla^2 - \frac{1}{v_s^2}\frac{\partial^2}{\partial t^2}\right) p = -\frac{\Gamma}{v_s^2}\frac{\partial H}{\partial t}, \tag{1.1}$$

Where p is the pressure generated due to photothermal expansion, v_s is this longitudinal wave speed in this medium, Γ is the dimensionless Grüneisen parameter denoted as $\frac{\beta v_s^2}{C_p}$ (where β is the thermal coefficient of volume expansion and C_p is the heat capacity at constant pressure), and H is the thermal energy per unit volume and per unit time due to laser illumination and its corresponding temperature rise [74, 79, 80]. If the laser pulse duration is less than a characteristic confinement time, referred as the stress confinement condition, the pressure magnitude can be estimated by a product of the Grüneisen parameter Γ, the local optical absorption coefficient μ_a ,and the optical fluence F at the absorber [74, 80].

There are two types of optical absorbers acting as sources of propagating ultrasound. One is the natural optical absorber in biological tissue, such as hemoglobin [81]. Since this natural absorber is part of biological tissue, its absorption spectrum changes in response to its metabolic state [76, 81]. PA image based on hemoglobin optical properties can be used to derive local tissue's physiological status such as the oxygen saturation of hemoglobin. The

other is an external optical contrast agent, such as gold nanorods [82, 83]. Sensitive contrast agents can be functionalized to target specific bimolecular markers of cancer cells. PA imaging measuring these targeted contrast agents can obtain significant clinical information about the disease at a molecular level. PA imaging has demonstrated great promise as a functional and molecular imaging tool with the help of these contrast agents.

1.4.2 Contrast Agents for PA Imaging

In PA imaging, contrast agents with high absorption in the near infrared (700-1000nm) have attracted the most attention because tissue has low absorption in this spectral range, allowing light to penetrate several centimeters into tissue. Different contrast agents, such as gold nanorods [82-84] and indocyanine-green-embedded ormosil nanoparticles [85], have been developed and investigated to increase specific contrast and sensitivity to some cancer cells.

One advantage of gold nanorods is the aspect ratio (length divided by the width) of the nanorod. The aspect ratio can be adjusted to achieve a different peak absorption wavelength. Gold nanorods with different aspect ratios can be functionalized to target different specific biomarkers at the same time. The second advantage of these contrast agents is that they can be used for photothermal cancer therapy since they can effectively convert radiant energy to local heat and destroy cancerous tissue. The performance of this photothermal therpy can be monitored using the calibrated linear relationship between PA signal magnitude and temperature rise [86]

Indocyanine-green-embedded ormosil nanoparticles have also been developed for multiple functions. First, these nanoparticles conjugated with HER-2 antibody can target breast cancer and prostate cancer cells and provide efficient absorption contrast for PA diagnosis. Second, they can be used as photodynamic therapy agents since the particles can generate toxic reactive oxygen for photoactivated chemotherapy treatment by radiant illumination [85].

These developed contrast agents can be used in PA imaging to increase specific contrast over background tissue absorption. However, in many anticipated clinical applications, such as in imaging prostate cancer, background tissue absorption, primarily due to blood pools, limit both the sensitivity and specificity of molecular imaging studies. As shown in Fig. 1.3, an oral epidermoid carcinoma tumor subcutaneously implanted in a mouse was clearly highlighted after gold rod targeting in PA imaging (right panel) compared to that (left panel) before the injection of the contrast agents [74, 87]. However, there are some other PA signals outside the tumor region even before the injection of the gold rods. In particular, background signals typically far exceed the minimum detectable PA signal level, thus limiting the linear concentration range for molecular contrast agents. If background signals can be suppressed, the molecular dynamic range of contrast agents can be greatly expanded, enhancing contrast and therefore the sensitivity and specificity of PA imaging [77, 88].

New developed iron oxide-gold core-shell nanoparticles [89] overcome the above limitation and also enable a new imaging mode, magnetomotive photoacoustic (mmPA) imaging with the help of speckle tracking. In this new

imaging modality, these particles are subjected to a time-varying magnetic field and create local motion in the surrounding tissue, which is synchronized with the magnetic field time variation. Like US imaging, mmPA image, as a coherent imaging modality, is also characterized by the presence of speckles. Speckle tracking can be used to estimate the motion due to magnetomotive manipulation of gold shell MNPs in a PA image sequence recorded during the time interval with magnetic field variation. The coherent motion processing of the PA image sequence (Fig. 1.4) can be used as a motion filter to reject diffuse or localized background signals and highlight the moving sources related to MNP-gold NPs. Compared to PA images using conventional nanoparticle contrast agents, mmPA can greatly enhance the specific contrast of the targeted region in this way as demonstrated in chapter 5.

1.5 Overview of this thesis

As described in the preceding sections, both US and PA imaging, as coherent imaging modalities, are characterized by the presence of speckle. Speckle can be treated as a spatial marker to derive underlying tissue motion or deformation using speckle-based tracking algorithms. This provides a foundation for both modalities to be applied for non-invasive and quantitative image-based disease diagnosis and therapy. The objective of this dissertation is to describe speckle tracking's application to cardiac strain imaging using US imaging and contrast enhancement in PA imaging.

Chapter 2 directly compares the accuracy of TDI and 2-D ST estimates of instantaneous axial normal strain and accumulated axial normal strain using a simulated heart. We then used an isolated rabbit heart model of acute ischemia produced by left descending anterior artery ligation to evaluate the performance of the two methods in detecting abnormal motion.

Chapter 3 introduces a well-controlled 2-D cardiac elasticity imaging technique using two coplanar and orthogonal linear probes simultaneously imaging an isolated retroperfused rabbit heart. Acute ischemia was generated by left anterior descending (LAD) artery ligation. An excitation-contraction decoupler, 2,3-butanedione monoxime, was applied at a 4mM concentration to reversibly reduce myocardial contractility. As demonstrated in this chapter, data from a single probe can detect directional changes in the in-plane principal deformation axes, helping to locate the bulging area due to LAD ligation. Results match well with corresponding Evans Blue staining, demonstrating that strains based on principal stretches can characterize heart muscle contractility.

Chapter 4 describes a LV phantom constructed using PVA cryogel and integrated with a pulsatile pump in combination with a pressure meter. A commercial 2-D phased array (Sonos 7500, Philips) was used to acquire 3-D RF data on the phantom with increased effective frame rate by reducing the stroke volume and the beats per minute of the pulsatile circulation system. 2-D and 3-D speckle tracking were tested on this 3-D data set. LV contraction and out-of-plane motion were also simulated and tracked using a computer model of cardiac imaging.

Chapter 5 demonstrates that PA contrast can be greatly increased by magnetically manipulating Au-shell-encapsulated magnetic nanoparticles (X. Gao's lab at the University of Washington). This coherent motion synchronized with the magnetic field variation in the PA image sequence can be estimated using speckle tracking method and used to distinguish between the targeted region and the unwanted background region without motion. In addition, mmPA imaging exhibits a potential for characterizing tissue's elasticity properties by measuring the relaxation time constant from the displacement time trace estimated using speckle tracking after magnetic field is turned off.

The dissertation concludes in Chapter 6 with a summary of the dissertation. This chapter also presents unsolved problems and future directions for biological application of speckle tracking for both modalities.

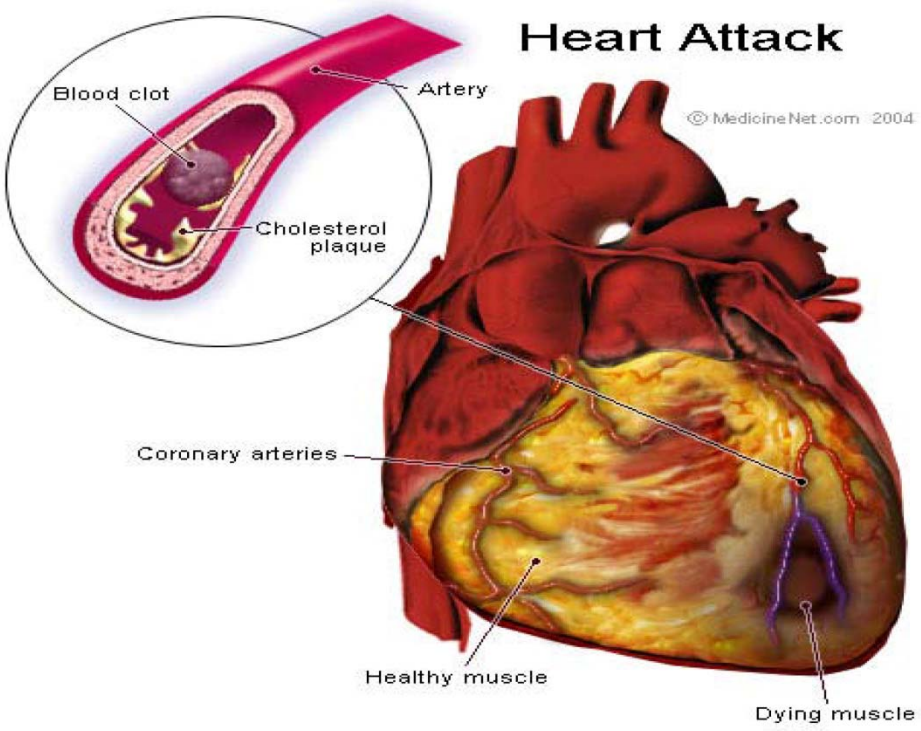

Figure 1.1 Illustration of myocardiac ischemia due to occlusion of a coronary artery. The image is obtained from MedicineNet.com. "Copyright (c) 1996 - 2005, WebMD, Inc. All rights reserved"

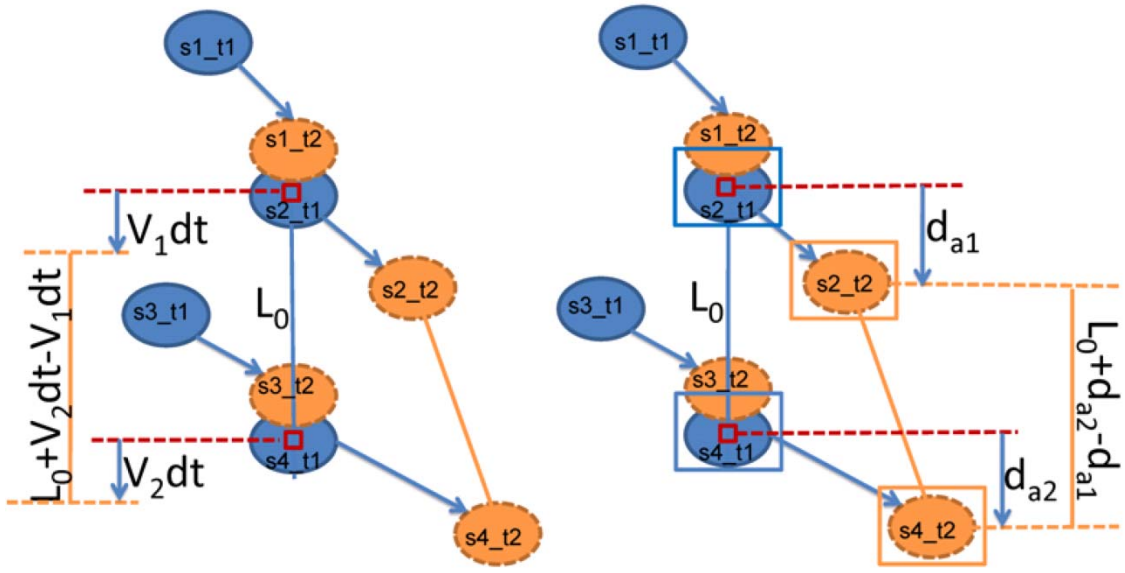

Figure 1.2 Axial normal strain estimation derived by TDI (a) and by 2-D ST (b). S1_t1 in blue means speckle 1 at time t1. S1_t2 in orange means speckle 1 at time t2. In TDI (a), V1 and V2 are TDI velocities in the interval dt = t2 − t1. The original axial distance between two points is L0. The axial distance changes to (L0+V2dt-V1dt). In 2-D ST (b), axial displacements (da1 and da2) of the same points labeled with red boxes are calculated by measuring the movement of speckles S2 and S4 shown in blue at time t1 and orange at time t2. Note: Fig.1.2 and Fig. 2.1 in chapter 2 are same.

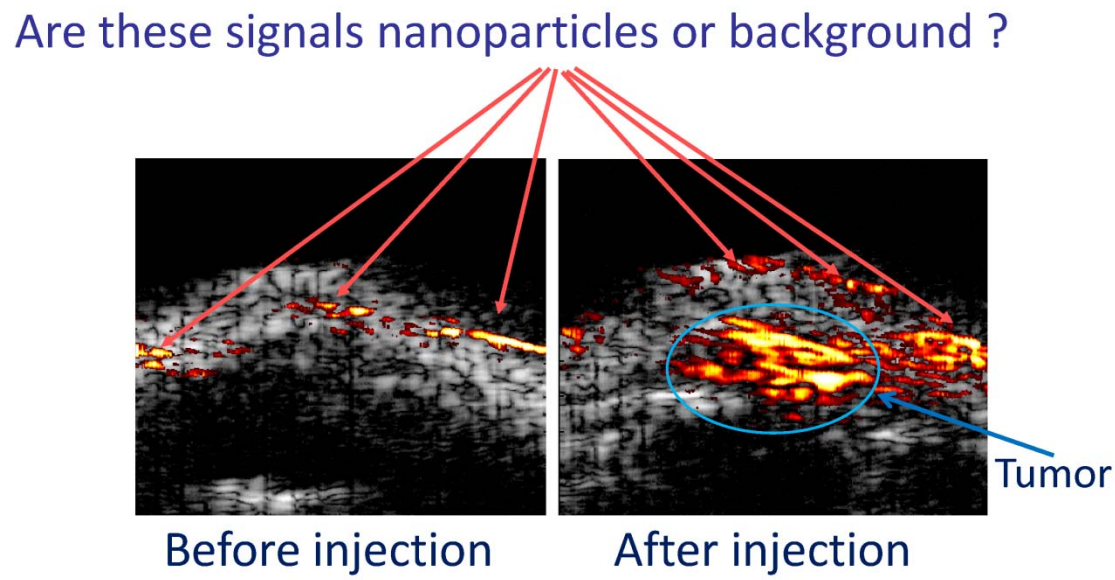

Figure 1.3 The existence of background signals before and after gold rod targeting in PA imaging. “Reprinted with permission from [74]. Copyright 2009, American Institute of Physics.”

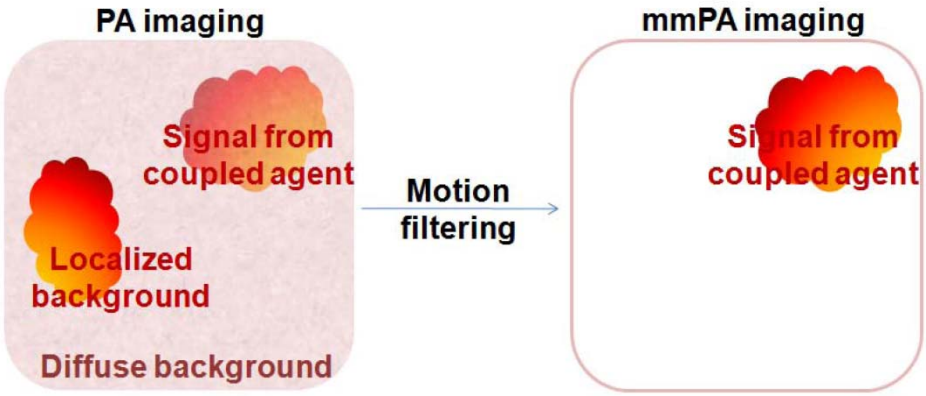

Figure 1.4 Schematic of contrast enhancement in mmPA imaging. mmPA imaging suppresses PA signals from localized or diffuse region and distinguishes moving regions due to the response of coupled agents to a magnetic field.

1.6 References

[1] J. W. Goodman, “Some fundamental properties of speckle,” *J. Opt. Soc. Am*, vol. 66, no. 11, pp. 1145–1150, Nov. 1976.

[2] R. F. Wagner, S. W. Smith, J. M. Sandrik, and H. Lopez, “Statistics of speckle in ultrasound B-scans,” *IEEE Transactions on Sonics and Ultrasonics*, vol. 30, no. 3, pp 156–163, May 1983.

[3] X. Zhong, M. A. Lubinski, N. Sanghvi, M. O’Donnell, and C. A. Cain, “Speckle tracking and motion compensation for ultrasound-based lesion localization”, *IEEE 1997 Ultrasonics Symposium Proceedings*, vol. 2, pp. 1381-1384, Oct. 1997.

[4] J. Meunier and M. Bertrand, “Ultrasonic texture motion analysis: theory and simulation,” *IEEE Transactions on Medical Imaging*, vol. 14, no. 2, pp. 293-300, Jun. 1995.

[5] M. O’Donnell, A. R. Skovoroda, B. M. Shapo, and S. Y. Emelianov, “Internal displacement and strain imaging using ultrasonic speckle tracking,” *IEEE Trans. Ultrason., Ferroelect., Freq. Contr.*, vol. 41, pp. 314-325, May 1994.

[6] M. Dewan, “Imaged-based tracking methods – Applications to improve motion compensation in cardiac MR and image-guided surgery”. *Dissertation*, Sep. 2007.

[7] P. Shi, A. J. Sinusas, R. T. Constable, E. Ritman, and J. S. Duncan, “Point-tracked quantitative analysis of left ventricular motion from 3D image sequences,” *IEEE Transactions on Medical Imaging*, vol. 19, no. 1 pp. 26-50, 2000.

[8] J. Canny, “A computational approach to edge-detection”, *IEEE Transactions on Pattern Analysis and Machine Intelligence*, vol. 8, no. 6, pp. 679-698, Nov. 1986

[9] D. G. Lowe, “Distinctive image features from scale-invariant keypoints,” *International Journal of Computer Vision*, vol. 60, no. 2, pp. 91-110, Jan. 2004.

[10] J.E.Udelson, R.D.Patten, and M.A.Konstam, “New concepts in post-infarction ventricular remodeling”, *Reviews in Cardiovascular Medicine*, vol. 4, Suppl.3, 2003.

[11] S.D. Zimmerman, J. Criscione, and J.W. Covell, “Remodeling in myocardium adjacent to an infarction in the pig left ventricle,” *Am J Physiol Heart Circ Physiol*, vol. 287, pp. H2697-H2704, 2004.

[12] American Hear Associate, “Heart disease and stroke statistics – 2010 update,” *American Heart Association*, 2010.

[13] M.A. Pfeffer, “Left ventricular remodeling after acute myocardial infarction,” *Annu.Rev.Med*, vol. 46, pp. 455-66, 1995.

[14] D. K. Bogen, S. A. Rabinowitz, A. Needleman, T. A. Mcmahon, and W. H. Abelmann, “An analysis of the mechanical disadvantage of myocardial infarction in the canine left ventricle,” *Circ. Res*., vol. 47, no. 5, pp. 727-741, 1980.

[15] D. K. Bogen, A. Needleman and T. A. McMahon, “An Analysis of Myocardial Infarction: the Effect of Regional Changes in Contractility,” *Circ. Res*., vol. 55, pp. 805-815, 1984.

[16] J. W. Holmes, T. K. Borg, and J. W. Covell, “Structure and mechanics of healing myocardial infarcts,” *Annu. Rev. Biomed. Eng*., vol. 7, pp. 223-53, 2005.

[17] P. Theroux, D. Franklin, J. Ross, Jr., and W. S. Kemper, “Regional myocardial function during acute coronary artery occlusion and its modification by pharmacologic agents in the dog,” *Circulation Research*, vol.35, Dec. 1974.

[18] W. D. Edwards, “Pathology of myocardial infarction and reperfusion,” *Acute Myocardial Infarction*, second Edition, pp. 16-50, 1996.

[19] J. k. Oh, R. a. Nishimura, “Echocardiography in acute myocardial infarction,” *Acute Myocardial Infarction*, second Edition, pp 189-219.

[20] A. S. Jaffe, “Biochemical detection of acute myocardial infarction,” *Acute Myocardial Infarction*, second Edition, pp. 136-162.

[21] W. A. Jaber, F. P. DiFilippo, abd M. D. Cerqueira, “Left ventricular hypertrophy and SPECT myocardial perfusion imaging: Finding the diamonds in the rough,” *Journal of Nuclear Cardiology*, vol. 14, no. 3, pp. 398-407, May 2007.

[22] H. L. Wyatt, S. Meerbaum, M. K. Heng, J. Rit, P. Gueret, and E. Corday, “Experimental evaluation of the extent of myocardial dyssynergy and Infarct size by two dimensional echocardiography,” *Circulation*, vol. 63, pp. 607-614, 1981.

[23] D. C. Homans, R. Asinger, K. J. Elsperger, D. Erlien, E. Sublett, F. Mikell, and R. J. Bache, “Regional function and perfusion at the lateral border of ischemic myocardium,” *Circulation*, vol. 71, pp. 1038-1047, 1985.

[24] H. L. Wyatt, J. S. Forrester, P. L. da Luz, G. A. Diamond, R. Chagrasulis, and H. J. Swan, “Functional abnormalities in nonoccluded regions of myocardium after experimental coronary occlusion,” *Am J Cardiol*, vol. 37, pp. 366-372, 1976.

[25] A. F. Frangi, W.J. Nissen, M.A. Viergever, “Three-dimensional modeling for functional analysis of cardiac images,” *IEEE Transactions on Medical Imaging*, vol. 20, no.1, Jan. 2001.

[26] M. Kowalski, T. Kukulski, F. Jamal, J. D’hooge, F. Weidemann, F. Rademakers, B. Bijnens, L. Hatle, and G. R. Sutherland, “Can natural strain and strain rate quantify regional myocardial deformation?”, *Ultrasound in Med. & Biol. v*ol. 27, no. 8, pp. 1087-1097, 2001.

[27] L. Axek, A. Montill, and D. Kim, “Tagged magnetic resonance imaging of the heart,” *Medical Image Analysis,* vol. 9, pp. 376-393, 2005.

[28] W. G. O’Dell and A.D. McCulloch, “Imaging three-dimensional cardiac function,” *Annu. Rev. Biomed.Eng*. vol. 2, pp. 431-56, 2000.

[29] E McVeigh, “Cardiac magnetic resonance imaging,” *Cardiology Clinics*, vol. 16, No. 2, May. 1998.
[30] N. Reichek, “MRI myocardial tagging,” *Journal of Magnetic Resource Imaging*, vol. 10, pp. 609-616, 1999.
[31] X. Chen, “Cardiac strain rate imaging using 2-D speckle tracking,” *Dissertation in the University of Michigan*, 2004.
[32] A.D. Fleming, X. Xia, W.N. Mcdicken, G.R. Sutherland, and L Fenn,“Myocardial velocity gradients detected by Doppler imaging,” *the British Journal of Radiology*, vol. 67, pp. 679-688, Jul. 1994.
[33] M. Uematsu, K. Miyatake, N. Tanaka, H. Matsuda, A. Sano, N. Yamazaki, M. Hirama, and M. Yamagishi, “Myocardial velocity-gradient as a new indicator of regional left-ventricular contraction - detection by a 2-dimensional tissue Doppler imaging technique,” *Journal of the American College of Cardiology*, vol. 26, no. 1, pp. 217-223, Jul. 1995.
[34] S. Urheim, T. Edvardsen, H. Torp, B. Angelsen, and O.A. Smiseth, “Myocardial strain by Doppler echocardiography - validation of a new method to quantify regional myocardial function,” *Circulation*, vol. 102, no. 10, pp. 1158-1164, 2000.
[35] K. Kaluzynski, X. C. Chen, S. Y. Emelianov, A. R. Skovoroda, and M. O'Donnell, “Strain rate imaging using two-dimensional speckle tracking,” *IEEE Transactions on Ultrasonics Ferroelectrics and Frequency Control*, vol. 48, no. 4, pp. 1111-1123, Jul. 2001.
[36] J. D'hooge, B. Bijnens, J. Thoen, F. Van de Werf, G.R. Sutherland, and P. Suetens, “Echocardiographic strain and strain-rate imaging: A new tool to study regional myocardial function,” *IEEE Transactions on Medical Imaging*, vol. 21, no. 9, pp. 1022-1030, Sep. 2002.
[37] J. J. Heger, A. E. Weyman, L. S. Wann, J. C. Dillon, and H. Feigenbaum, “Cross-sectional echocardiography in acute myocardial-infarction - detection and localization of regional left-ventricular asynergy,” *Circulation*, vol. 60, pp. 531-538, 1979.
[38] J. D. Thomas and Z. B. Popovic, “Assessment of left ventricular function by cardiac ultrasound,” *Journal of the American College of Cardiology*, vol. 48, pp. 2012-2025, 2006.
[39] W. - N. Lee, C. M. Ingrassia, S. D. Fung-Kee-Fung, K. D. Costa, J. W. Holmes, and E. E. Konofagou, “Theoretical quality assessment of myocardial elastography with In vivo validation,” *IEEE Trans. Ultrason. Ferroelectr. Freq. Control*, vol. 54, no. 11, pp. 2233-2245, 2007.
[40] C. Jia, R. Olafsson, K. Kim, T. Kolias, J. Rubin, W. Weitzel, R. Witte, S. Huang, M. Richards, C. Deng, and M. O'Donnell, “Two-dimensional strain imaging of controlled rabbit hearts,” *Ultrasound in Medicine & Biology*, vol. 35, no. 9, pp. 1488-1501, Sep. 2009.
[41] J. D'hooge, A. Heimdal, F. Jamal, T. Kukulski, B. Bijnens, F. Rademakers, L. Hatle, P. Suetens, and G. R. Sutherland, “Regional strain and strain rate measurements by cardiac ultrasound: principles, implementation and limitations,” *European Journal of Echocardiography*, vol. 1, no. 3, pp. 154-170, 2000.

[42] G. R. Sutherland, L. Hatle, P. Claus, J. D'hooge, and B.H. Bijnens, "Doppler myocardial imaging," Belgium: BSWK, bvba, 2006, ch.3-4.
[43] W. N. McDicken, G. R. Sutherland, C. M. Morgan, and L. N. Gordon, "Colour Doppler velocity imaging of the myocardium," *Ultrasound in Medicine and Biology*, vol.18, no. 6-7, pp. 651-654, 1992.
[44] K. Matre, A. B. Ahmed, H. Gregersen, A. Heimdal, T. Hausken, S. Ødegaard, and O. H. Gilja**, "**In vitro evaluation of ultrasound Doppler strain rate imaging: modification for measurement in a slowly moving tissue phantom," *Ultrasound Med. Biol.*, vol. 29, no. 12, pp. 1725-1734, Dec. 2003.
[45] A. Heimdal, A. Støylen, H. Torp, and T. Skjærpe**, "**Real-time strain rate imaging of the left ventricle by ultrasound," *Journal of the American Society of Echocardiography*, vol. 11, no. 11, pp. 1013-1019, Nov. 1998.
[46] T. Edvardsen, B. L. Gerber, J. Garot, D. A. Bluemke, J. A. C. Lima, and O. A. Smiseth**, "**Quantitative assessment of intrinsic regional myocardial deformation by Doppler strain rate echocardiography in humans - validation against three-dimensional tagged magnetic resonance imaging," *Circulation*, vol. 106, no. 1, pp. 50-56, Jul. 2002.
[47] G. R. Sutherland, G. D. Salvo, P. Claus, J. D'hooge, and B. Bijnens**, "**Strain and strain rate imaging: A new clinical approach to quantifying regional myocardial function," Journal *of the American Society of Echocardiography*, vol. 17, no. 7, pp.788-802, Jul. 2004.
[48] A. R. Skovoroda, S. Y. Emelianov, M. A. Lubinski, A. P. Sarazyan, and M. O'Donnell, "Theoretical analysis and verification of ultrasound displacement and strain imaging," *IEEE Trans. Ultrason., Ferroelect., Freq. Contr.*, vol. 41, pp. 302-313, May 1994.
[49] M. A. Lubinski, S. Y. Emelianov, and M. O'Donnell, "Speckle tracking methods for ultrasonic elasticity imaging using short time correlation," *IEEE Trans. Ultrason., Ferroelect., Freq. Contr.*, vol. 46, pp. 82-96, Jan. 1999.
[50] E. E. Konofagou and J. Ophir, "A new elastographic method for estimation and imaging of lateral strains, corrected axial strains and Poison's ratios in tissues," *Ultrasound in Medicine & Biology*, vol. 24, no. 8, pp. 1183-1199, Oct. 1998.
[51] F. Yeung, S. F. Levinson, and K. J. Parker, "Multilevel and motion model-based ultrasonic speckle tracking algorithms," *Ultrasound in Medicine & Biology*, vol. 24, no. 3, pp. 427-441, Mar. 1998.
[52] R. L. Maurice and R. Bertrand, "Lagrangian speckle model and tissue-motion estimation – Theory," *IEEE Transactions on Medical Imaging*, vol. 18, no. 7, pp. 593-603, Jul. 1999.
[53] E. Brusseau, J. Kybic, J. F. Deprez, and O. Basset, "2-D locally regularized tissue strain estimation from radio-frequency ultrasound images: Theoretical developments and results on experimental data", *IEEE Trans. on Medical Imaging*, vol. 27, no. 2, pp. 145-160, Feb. 2008.

[54] E. E. Konofagou, J. D'hooge, and J. Opir, "Myocardial elastography—a feasibility study in vivo," *Ultrasound in Medicine & Biology*, vol. 28, no.4, pp. 475-482, Apr. 2002.

[55] J. D'Hooge, E. E. Konofagou, F. Jamal, A. Heimdal, L. Barrios, B. Bijmens, J. Thoen, F. Van de Werf, G. Sutherland, and P. Suetens, "Two-dimensional ultrasonic strain rate measurement of the human heart in vivo," *IEEE Trans. Ultrason., Ferroelect., Freq. Contr.*, vol. 49, no. 2, pp. 281-286, Feb. 2002.

[56] S. Langeland, J. D'hooge, T. Claessens, P. Claus, P. Verdonck, P. Suetens, G. R. Sutherland, and B. Bijnens, "RF-based two-dimensional cardiac strain estimation: a validation study in a tissue-mimicking phantom," *IEEE Trans. Ultrason. Ferroelectr. Freq. Control*, vol. 51, no. 11, pp. 1537-1546, Nov. 2004.

[57] J. W. Luo and E. E. Konofagou, "High-frame rate, full-view myocardial elastography with automated contour tracking in murine left ventricles in vivo," *IEEE Trans. Ultrason. Ferroelectr. Freq. Control*, vol. 55, no. 1, pp. 240-248, Jan. 2008.

[58] W. - N. Lee, Z. Qian, C. Tosti, T. Brown, D. Metaxas, and E. E. Konofagou "Preliminary validation of angle-independent myocardial elastography using MR tagging in a clinical setting," *Ultrasound in Medicine & Biology*, vol. 34, no. 12, pp. 1980-1997, Dec. 2008.

[59] X. Chen, H. Xie, R. Erkamp, K. Kim, C. Jia, J. M. Rubin, and M. O'Donnell, "3-D correlation-based speckle tracking," *Ultrasonic Imaging*, vol. 27, pp. 21-36, 2005.

[60] C. Jia, R. Olafsson, K. Kim, T. J. Kolias, J. M. Rubin, H. Xie, and M. O'Donnell, "2D speckle tracking vs DTI-derived elasticity imaging on an isolated rabbit heart," *IEEE 2008 Ultrasonics Symposium Proceedings*, vols. 1-4 and Appendix, pp. 958-961, 2008.

[61] M. Leitman, P. Lysyansky, S. Sidenko, V. Shir, E. Peleg, M. Binenbaum, E. Kaluski, R. Krakover, and Z. Vered, "Two-dimensional strain - a novel software for real-time quantitative echocardiographic assessment of myocardial function," *Journal of the American Society of Echocardiography,* vol. 17, pp. 1021-29, 2004.

[62] R. Q. Migrino, X. G. Zhu, N. Pajewski, T. Brahmbhatt, R. Hoffmann, and M. Zhao, "Assessment of segmental myocardial viability using regional 2-dimensional strain echocardiography," *Journal of the American Society of Echocardiography*, vol. 20, pp. 342-51, 2007.

[63] R. G. P. Lopata, M. M. Nillesen, I. H. Gerrits, J. M. Thijssen, L. Kapusta, F. N. van de Vosse, and C. L. de Korte, "In vivo 3D cardiac and skeletal muscle strain estimation," *2006 IEEE Ultrasonics Symposium,* pp. 744-747, Oct. 2006.

[64] D. Rappaport, E. Konyukhov, D. Adam, A. Landesberg, and P. Lysyansky, "In vivo validation of a novel method for regional myocardial wall motion analysis based on echocardiographic tissue tracking," *Medical & Biological Engineering & Computing,* vol. 46, pp. 131-37, 2008.

[65] G. Y. Cho, J. Chan, R. Leano, M. Strudwick, and T. H. Marwick, “Comparison of two-dimensional speckle and tissue velocity based strain and validation with harmonic phase magnetic resonance imaging,” *American Journal of Cardiology*, vol. 97, pp. 661-66, 2006.

[66] G. Perk, P. A. Tunick, and I. Kronzon, “Non-Doppler two-dimensional strain imaging by echocardiography - From technical considerations to clinical applications,” *Journal of the American Society of Echocardiography,* vol. 20, pp. 234-43, 2007.

[67] R. J. Atkin and N. Fox, “An introduction to the theory of elasticity,” London, New York: Longman, 1980.

[68] C. Jia, R. Olafsson, K. Kim, R. S. Witte, S. - W. Huang, T. J. Kolias, J. M. Rubin, W. F. Weitzel, C. Deng, and M. O’Donnell. “Controlled 2D cardiac elasticity imaging on an isolated perfused rabbit heart,” *IEEE International Ultrasonics Symposium*, pp. 745-748, 2007.

[69] I. K. Zervantonakis, S. D. Fung-Kee-Fung, W. - N. Lee, E. E. Konofagou, “A novel, view-independent method for strain mapping in myocardial elastography: eliminating angle- and centroid-dependence,” *Physics in Medicine and Biology,* vol. 52, pp.4063-80, 2007.

[70] M. A. Lubinski, S. Y. Emelianov, K. R. Raghavan, A. E. Yagle, A. R. Skovoroda, and M. O'Donnell, “Lateral displacement estimation using tissue incompressibility,” *IEEE Transactions on Ultrasonics, Ferroelectrics, and Frequency Control,* vol. 43, pp. 234-46, 1996.

[71] A. F. Frangi, W. J. Nissen, M. A. Viergever, “Three-dimensional modeling for functional analysis of cardiac images: A Review,” *IEEE Transactions on Medical Imaging*, vol.20, no.1, Jan. 2001.

[72] C. Jia, K. Kim, T. J. Kolias, W. F. Weitzel, J. M. Rubin, and M. O’Donnell, “Left ventricular phantom with pulsatile circulation for ultrasound strain rate imaging,” *Proceedings of the 2006 IEEE Ultrasonics Symposium*, 2006.

[73] C. Jia, K. Kim, T. J. Kolias, J. M. Rubin, W. F. Weitzel, P. Yan, D. Dione, A. J. Sinusas, J. Duncan, and M. O’Donnell, “4D elasticity imaging of PVA LV phantom integrated with pulsatile circulation system using 2D phased array,” *Proceedings of the 2007 IEEE Ultrasonics Symposium*, 2007.

[74] S. Y. Emelianov, P. - C. Li, and M. O'Donnell, "Photoacoustics for molecular imaging and therapy," *Physics Today,* vol. 62, no. 5, pp. 34-39, 2009.

[75] A. A. Oraevsky, S. L. Jacques, R. O. Esenaliev, and F. K. Tittel, "Determination of tissue optical-properties by piezoelectric detection of laser-induced stress waves," *Proc. SPIE* 1882, pp. 86-101, 1993.

[76] L. W. Wang and M. Xu, "Photoacoustic imaging in biomedicine", *Rev. Sci. Instrum*. Vol. 77, 041101, 2006.

[77] S. - W. Huang, J. F. Eary, C. Jia, L. Huang, S. Ashkenazi, and M. O'Donnell, "Differential-absorption photoacoustic imaging," *Optics Letters*, vol. 34, no. 16, pp. 2393-2395, 2009.

[78] C. Jia, S. - W. Huang, Y. Jin, C. Seo, L. Huang, X. Gao, and M. O’Donnell, “Integration of Photoacoustic, Ultrasound and Magnetomotive System,” *2010 SPIE Photonics West*, San Francisco, CA, USA, Jan. 2010.

[79] A. C. TAM, “Applications of photoacoustic sensing technique,” *Reviews of Modern Physics*, vol. 58, no. 2, pp. 381-431, Apr. 1986.

[80] G. J. Diebold, T. Sun, “Properties of photoacsoutic waves in one-dimension, 2-dimension, and 3-dimension,” *Acustica*, vol. 80, no. 4, pp. 339-351, Jul.-Aug. 1994.

[81] X. Wang, X. Xie, G. Ku, L. V. Wang, and G. Stoica, “Noninvasive imaging of hemoglobin concentration and oxygenation in the rat brain using high-resolution photoacoustic tomography,” *J. Biomed.Opt*., vol. 11, 024015, 2006.

[82] P. - C. Li, C. - W. Wei, C. - K. Liao, C. - D. Chen, K. - C. Pao, C. - R. C. Wang, Y. - N. Wu, and D. -B. Shieh, “Multiple targeting in photoacoustic imaging using bioconjugated gold nanorods,” *Proc. SPIE 6086*,60860M, 2006.

[83] A. Agarwal, S.-W. Huang, M. O'Donnell, K. C. Day, M. Day, N. Kotov, and S. Ashkenazi, “Targeted gold nanorod contrast agent for prostate cancer detection by photoacoustic imaging”, *Journal of Applied Physics,* vol. 102, no. 6, 2007.

[84] A. Agarwal, S. - W. Huang, M. O’Donnell, K. C. Day, M. Day, N. Kotov, and S. Ashkenazia, “Targeted gold nanorod contrast agent for prostate cancer detection by photoacoustic imaging,” *Journal of Applied Physics*, 102, 064701, 2007.

[85] G. Kim, S. - W. Huang, K. C. Day, M. O’Donnell, R. R. Agayan, M. A. Day, R. Kopelman, and S. Ashkenazi, “Indocyanine-green-embedded PEBBLEs as a contrast agent for photoacoustic imaging,” *Journal of Biomedical Optics 124*, 044020 July/August 2007.

[86] J. Shah, S. Park, S. Aglyamov, T. Larson, L. Ma, K. Sokolov, K. Johnston, T. Milner, and S. Y. Emelianov, “Photoacoustic imaging and temperature measurement for photothermal cancer therapy,” *Journal of Biomedical Optics*, vol. 13, no. 3, 034024, MAY-JUN, 2008.

[87] P. –C. Li, C. –R. C. Wang, D. –B. Shieh, C. –W. Wei, C. –K. Liao, C. Poe, S. Jhan, A. –A. Ding, and Y. –N. Wu, “In vivo photoacoustic molecular imaging with simultaneous multiple selective targeting using antibody-conjugated gold nanorods,” *Optics Express,* vol. 16, no. 23, Nov. 2008.

[88] C. Jia, S. - W. Huang, Y. Jin, C. Seo, L. Huang, X. Gao, and M. O’Donnell, “Integration of photoacoustic, ultrasound and magnetomotive system,” *2010 SPIE Photonics West*, San Francisco, CA, USA, Jan. 2010.

[89]. Y. Jin, C. Jia, S.-W. Huang, M. O’Donnell, and X. Gao, “Multifunctional Nanoparticles as Coupled Contrast Agents,” *Nature Materials*, under revision, 2009.

Chapter 2 Comparison of 2-D Speckle Tracking and Tissue Doppler Imaging

2.1 Introduction

Section 1.3.3 stated that strain imaging derived from TDI or 2-D ST for clinical diagnosis must be interpreted correctly based on the way in which strains are derived since two methods have different accuracy in estimating even the same parameters such as instantaneous axial normal strain and accumulated axial normal strain. Unfortunately, these fundamental differences are mostly neglected when the strain or strain rate from either method is used to assess myocardial deformation.

In this chapter, we clearly address this issue using a simulated heart and a well-controlled rabbit heart model based on a Langendorff preparation. The performance of each method in detecting abnormal motion was compared using a rabbit heart model of ischemia generated by ligating the LAD coronary artery. The dramatic reduction of lesion detection's angle dependency for 2-D ST was also demonstrated by comparing the principal axes of deformation before and after LAD ligation.

In this study, TDI-derived and 2-D ST-derived axial normal strains are calculated using the same broadband transmit pulse typical for tissue B-mode imaging. This is different from traditional color Doppler imaging for blood,

typically acquired using a narrowband transmit pulse to get sufficient SNR by sacrificing axial resolution. However, SNR for imaging tissue velocities is much higher than that for blood velocity imaging. For myocardial imaging, both B-mode and Doppler imaging can use the same broadband pulse to maintain higher axial resolution [1, 2]. TDI requires knowledge of the central frequency to convert the measured phase shift into velocity. Frequency-dependent attenuation downshifts the central frequency of a broadband pulse [3], which affects the accuracy of TDI velocity estimates. We have demonstrated that 2-D ST-derived axial normal strain has less variance than TDI-derived ones at different bandwidths [4]. In this study, we compare the strain derived using these two methods from the same broadband transmit pulse, maintaining the same spatial resolution for both methods. To reduce the effect of frequency-dependent attenuation on TDI-derived strain, the simulated heart did not include frequency-dependent attenuation. The central frequency downshift due to attenuation is small in rabbit heart perfused using a Langendorff preparation. Therefore, one central frequency estimated from the top part of the heart wall was used for TDI velocity estimation in the whole heart.

2.2 Methods

2.2.1 TDI-derived Axial Normal Strain

TDI estimates myocardial velocity by estimating the frequency shift due to Doppler effects using the auto-correlation function at a fixed spatial location or point (i.e., image pixel) [5, 6]. One 2-D ultrasound image consists of multiple

ultrasound beams. Denote the complex baseband signal at each point as $s_i(b,m)$, where i is image number, b is beam number, and m is depth index. To estimate tissue velocity v at point (*b*, *m*), lag one of the 1-D autocorrelation function

$$R_{b,m}(1) = \frac{1}{N-1}\sum_{i=0}^{N-2} s_i^*(b,m)\cdot s_{i+1}(b,m),\ N \geq 2, \tag{2.1}$$

is first calculated, and then its phase $ang(R_{b,m}(1))$ is scaled as follows:

$$\mathrm{v(b,m)} = \frac{\mathrm{c}}{4\pi \mathrm{f_0 T}}\cdot \mathrm{ang(R_{b,m}(1))}, \tag{2.2}$$

where T is the pulse repetition time, f_0 is the central frequency of the ultrasound pulse, and c is the sound speed [5].

To avoid aliasing [2, 6], a high pulse repetition frequency (PRF = $\frac{1}{T}$) is required to satisfy $\left|ang(R_{b,m}(1))\right| \leq \pi$, limiting the maximum velocity to no more than $\frac{c}{4 f_0 T}$. This constraint directly limits the dynamic range of axial strain rate (SR) and instantaneous axial strain ε, where

$$\mathrm{SR(b,m)} = \frac{\mathrm{v(b,m+p)} - \mathrm{v(b,m-p)}}{2\mathrm{p}\cdot\Delta\mathrm{d}}, \tag{2.3}$$

and

$$\varepsilon(\mathrm{b,m}) = \mathrm{SR(b,m)}\cdot(\mathrm{N}-1)\cdot\mathrm{T} \tag{2.4}$$

are estimated using the spatial gradient of these velocities [7, 8]. Here *p* is a number of pixels along the axial direction, Δd is the distance per pixel in the same direction, and 2 $p \cdot \Delta d$ is the axial distance between the two points where the velocities are estimated. The instantaneous axial normal strain is the linear scaled version of SR according to Eq. (2.4).

Instantaneous axial normal strain is typically small and sensitive to noise due to the high PRF. It is integrated to obtain larger strains, such as the accumulated axial normal strain at the end of systole, to quantify myocardial function with higher strain SNR [9]. The most frequently used accumulated axial normal strain in TDI is called natural strain [1], defined as

$$\varepsilon_{\mathrm{N}}(\mathrm{b},\mathrm{m},\mathrm{l}) = \sum_{\mathrm{i}=0}^{\mathrm{l}-1} \left(\varepsilon_{\mathrm{i}}(\mathrm{b},\mathrm{m})\right). \tag{2.5}$$

To compare results with other methods or modalities (such as MRI), natural strain can be converted to approximate Lagrangian axial strain [1, 10] as

$$\varepsilon_{\mathrm{L}}(\mathrm{b},\mathrm{m},\mathrm{l}) = \exp(\varepsilon_{\mathrm{N}}(\mathrm{b},\mathrm{m},\mathrm{l}) - 1). \tag{2.6}$$

This approximation can produce significant errors as the strain magnitude increases [11].

2.2.2 2-D ST-derived Axial Normal Strain

Unlike TDI, 2-D ST displacement estimates are based on the similarity between the fine structure (speckle patterns) of two images [12]. As mentioned above, speckle formation and statistical properties are directly related to the

underlying tissue microstructure and can be used to track tissue motion as a spatial marker [13].

In 2-D ST, a complex correlation coefficient function, representing similarities between a speckle pattern centered at (b_0, m_0) in image *i* and speckle patterns centered around (b_0, m_0) in image (*i* + 1), is computed as

$$R_{b_0,m_0}(k,j) = \frac{\sum_{b=-B}^{B}\sum_{m=-M}^{M} s_i^*(b_0+b, m_0+m)\, s_{i+1}(b_0+b+k, m_0+m+j)}{\sqrt{\sum_{b=-B}^{B}\sum_{m=-M}^{M}\left|s_i(b_0+b, m_0+m)\right|^2}\sqrt{\sum_{b=-B}^{B}\sum_{m=-M}^{M}\left|s_{i+1}(b_0+b+k, m_0+m+j)\right|^2}}. \quad (2.7)$$

The 2-D displacement (d_a, d_l) is initially estimated by finding the peak position of the magnitude of the spatially filtered correlation coefficient function using a parabolic fit. The axial displacement d_a is then further refined by calculating the position of the phase zero-crossing around the peak correlation coefficient [14, 15, 12]. Since there is no phase information in the lateral direction, lateral displacement d_l estimates have much larger variance than axial ones [16].

Similar to the derivation of SR and/or strain in TDI, the axial normal strain can be estimated using the spatial gradient of the axial displacement as

$$\varepsilon_a(b,m) = \frac{d_a(b,m+n) - d_a(b,m-n)}{2n \cdot \Delta d}. \quad (2.8)$$

The derivation of axial normal strain using 2-D ST is different from that using TDI. As shown in Fig. 2.1, the axial normal strains, induced from time t1 (speckles shown in blue) to time t2 (speckles shown in orange), between the two points

labeled with two red boxes centered at speckles S2 and S4 are calculated using TDI and 2-D ST as

$$\varepsilon_{\mathrm{TDI}} = \frac{(L_0 + V_2 dt - V_1 dt) - L_0}{L_0} = (\frac{V_2 - V_1}{L_0}) \cdot dt \tag{2.9}$$

and

$$\varepsilon_{\mathrm{a}} = \frac{(L_0 + d_{a2} - d_{a1}) - L_0}{L_0} = \frac{d_{a2} - d_{a1}}{L_0}, \tag{2.10}$$

respectively.

In Fig. 2.1 (a), V_1 and V_2 are the average axial velocities computed from TDI of tissue passing through the two points during time duration dt = t2 − t1. A total of N beams are used to collect information on moving tissue using Eqs. (2.1) and (2.2). The contributing tissue to a pixel varies with the beam number or time, depending on the imaging system's point spread function. Reduced overlap of the same tissue during these N beams can directly degrade the autocorrelation function and increase variance of the strain estimate. In addition, to avoid velocity estimation aliasing, TDI requires high PRF, further amplifying the variance. In contrast, as confirmed in Section 3, with moderate frame rate, 2-D ST can reduce variance of strain estimates by following the same speckle patterns around those points (see Fig. 2.1 (b)) in-plane using the cross-correlation method presented in Eqs. (2.6) and (2.7). Even when velocities (or displacements) estimated by TDI are filtered to have the same spatial resolution as those using 2-D ST, TDI still has larger variance.

In 2-D ST, the accumulated axial displacement following the same tissue is obtained by tracing back recorded displacements through the tracking period using

$$d_{a,i_Q i_1}(b,m) = d_{a,i_{Q-1} i_1}(b,m) + d_{a,i_Q i_{Q-1}}(b + d_{l,i_{Q-1} i_1}(b,m), m + d_{a,i_{Q-1} i_1}(b,m)), \quad (2.11)$$

where $d_{a,i_Q i_1}(b,m)$ is the axial displacement at image frame *Q* referenced back to image frame 1, and $d_{l,i_{Q-1} i_1}(b,m)$ is the lateral displacement at frame *Q-1* referenced back to frame 1. Accumulated axial normal strain derived using 2-D ST can overcome the registration error in TDI.

2.2.3 Simulation

To evaluate the accuracy of TDI and 2-D ST, a thick annulus of outer radius b=14.9mm and inner radius a=8mm was used to simulate a 2-D rabbit left ventricle in short axis view. The simulated heart wall was subjected to uniform internal and external pressures p_a and p_b [17], resulting in lateral and axial displacements:

$$\begin{aligned} d_l &= \frac{1}{E}\left[-\frac{A}{r^2} + 2C - \gamma\left(\frac{A}{r^2} + 2C\right)\right]\cdot\frac{x}{r} \\ d_a &= \frac{1}{E}\left[-\frac{A}{r^2} + 2C - \gamma\left(\frac{A}{r^2} + 2C\right)\right]\cdot\frac{y}{r}, \end{aligned} \quad (2.12)$$

where $A = \frac{a^2 b^2 (p_b - p_a)}{b^2 - a^2}$, $C = \frac{p_a a^2 - p_b b^2}{2(b^2 - a^2)}$, $r = \sqrt{x^2 + y^2}$ is the distance between an imaging pixel at (x, y) and the origin of the coordinate system (the center of

left ventricle), E is Young's modulus, and γ is Poisson's ratio, set equal to 0.5 because the tissue is assumed incompressible here.

To simplify the simulation, we assume *C=0*. The internal pressure p_a through the heart cycle was linearly scaled to the left ventricular pressure curve recorded during the Langendorff rabbit heart experiment described in Section 2.2.4. RF data were generated by convolving scatterer distributions with the point spread function (PSF) of a simulated linear array with 128 elements and a pitch of 0.23mm at a central frequency of 5MHz [18]. The sampling frequency and PRF were 40MHz and 740Hz, respectively, and the electronic SNR was 40 dB. Frequency-dependent attenuation is not considered here. The same RF data were used to estimate velocities (or displacements) using TDI and 2-D ST. Results derived using TDI were filtered to have the same resolution of 0.9 mm axially and 1.1 mm laterally as those using 2-D ST. The spatial resolution was estimated using the full width at half maximum of the autocorrelation of the difference between the parameter's estimated values and a smooth fit to the values, as described in [19].

2.2.4 Experimental Procedure

To compare the performance of TDI and 2-D ST for assessing myocardial function and detecting abnormal motion, an *ex vivo* experiment was performed on an isolated rabbit heart before and after LAD coronary artery ligation, mimicking a healthy heart and a diseased heart with acute ischemia, respectively. Since TDI can only detect myocardial dysfunction along the axial direction, the

ischemic region of the anterior wall produced by ligating the LAD was positioned at 12 o'clock close to the probe, as shown in Fig. 2.2 (b).

The animal used in this study was treated according to a protocol approved by the Institutional Animal Care and Use Committee at the University of Washington. The detailed Langendorff preparation and procedure can be found in [4]. A brief description is given here. A New Zealand white rabbit (about 3 kg) was anesthetized and euthanized. The heart was excised, mounted, and retroperfused on a Langendorff setup with modified, oxygenated Krebs-Henseleit (K-H) buffer (pH 7.4; 37°C; 95% O2/5% CO_2) through the aorta with perfusion pressure between 40-50 mmHg. The K-H buffer includes 117 mM NaCl, 4.0 mM KCl, 1.2 mM $MgCl_2 \bullet 6H_2O$, 1.1 mM KH_2PO_4, 5.0 mM glucose, 5.0 mM L-glutamate, 2.0 mM pyruvic acid, 25.0 mM $NaHCO_3$, and 2.6 mM $CaCl_2 \bullet 2H_2O$.

The heart was paced at the apex at about 3Hz with two Teflon insulated tungsten wires attached to a function generator (5 V, 500μs square pulse, HP33120A, Agilent Technologies, Santa Clara, CA, USA). The ECG signal was recorded using three Teflon insulated tungsten wires and filtered through a differential amplifier with gain of 1000 and bandwidth 1-3000 Hz (AM502, Tektronix, Richardson, TX, USA). The LV pressure was recorded by a pressure meter through a latex balloon filled with water and inserted via the left atrium into the left ventricle. The LV pressure signal was filtered through a second differential amplifier with gain of 50 and bandwidth 0.1-3000 Hz (AM502, Tektronix). Both ECG and LV pressure signals were digitized simultaneously

using an oscilloscope (TDS1002, Tektronix) and transferred to a computer via GPIB.

A linear probe (L14-5/38) connected to a commercial US scanner (SonixRP, Ultrasonix, Richmond, BC, Canada) was used to acquire RF data. The pacing signal, LV pressure, ECG signal and RF capture were synchronized through a field programmable gate array chip (ezFPGA-C6-6, Dallas Logic, Plano, TX, USA).

During the experiment, two RF data sets were acquired before and after LAD ligation for TDI and 2-D ST velocity estimation. After data acquisition, the heart was detached from the Langendorff perfusion system and then retroperfused with 2ml of 0.4% Evan's Blue for about 10 seconds until the heart was stained uniformly [4, 20]. The heart was then cut and optical images were taken at the stained cross section corresponding to the short-axis view used for the experiment. The unstained area was the area at risk due to LAD ligation [20] and was used to validate the abnormal region determined by principal axes analysis.

To fully cover the heart and acquire RF data with high PRF, 17 partially overlapped beam packages (labeled segments) with 13 beams per package, as shown in Fig. 2.2 (b), were fired with a central frequency of 5 MHz. For each segment, RF data (firing package) were acquired over one heart cycle at a PRF of 740Hz. TDI velocities and 2-D ST displacements were estimated on the same RF data with the scheme shown in Fig. 2.2 (a). For the TDI method, every four consecutive frames were used to calculate the auto-correlation function using Eq.

(2.1) to estimate velocity. 2-D ST used the first and last frame from the same set to calculate cross-correlation using Eq. (2.7) to estimate corresponding displacement or velocity. TDI velocities were filtered two-dimensionally to achieve the same spatial resolution of 1.0 mm axially and 1.5 mm laterally as those acquired by 2-D ST. The spatial resolution was estimated in the same way as the simulation, as described in Section 2.2.3. Tracking results on the central five beams from each beam segment were used to reconstruct 2-D images.

2.3 Results

2.3.1 Instantaneous Axial Normal Strain

Instantaneous tracking results from TDI and 2-D ST (same spatial resolution) at peak strain rate during systole in the simulated heart are compared to the theoretical results in Fig. 2.3. Masks were applied to both simulation and experiment results to remove boundary effects. Axial and lateral directions in all figures are, respectively, defined to be along the y direction and the x direction shown in Fig. 2.3 (a). Both axial displacements (the first row) and axial normal strain (the second row) from 2-D ST (the middle column) and TDI (the right column) resemble the corresponding theoretical results (the left column). However, variations are more pronounced for TDI (Fig. 2.3 (c)) compared to 2-D ST (Fig. 2.3 (b)), and significantly amplified in the TDI derived axial normal strain image in Fig. 2.3 (f). Indeed, there is considerably more error in the TDI-derived axial norm strain error map (Fig. 2.4 (b)) compared to the 2-D ST one (Fig. 2.4

(a)). The averaged absolute error in strain units over the whole heart wall using TDI is 0.36%, four times that of 2-D ST (0.08% error).

In addition to the lower frame rate in comparison with the PRF used in TDI, one reason for this substantial error reduction is that 2-D ST is capable of estimating lateral displacements. As shown in Fig. 2.5, lateral displacement (Fig. 2.5 (b)) estimated by 2-D ST matches reasonably well the theoretical one (Fig. 2.5 (a)). This additional information improves 2-D ST's tracking performance in areas with large lateral displacements, such as both the left and right sides of the heart wall. However, equivalent errors are also found in the central part of both the top and bottom of the heart wall shown in Fig. 2.4(b), where small or zero lateral displacements occur. Axial displacements play a significant role in this part of the error. Signals used to calculate the autocorrelation function carry a different percentage of motion information from different tissues, causing greater variance in velocity and axial normal strain estimation even with spatial averaging to match 2-D ST's spatial resolution. 2-D ST overcomes this problem by maintaining the similarity between two images by following the same speckle pattern used as a spatial marker to estimate underlying tissue motion.

The difference in instantaneous axial normal strains estimated by the two methods is further demonstrated with the results from the Langendorff-prepared rabbit heart. As shown in Fig. 2.6, the axial normal strain before (the first row) and after (the second row) LAD ligation using 2-D ST (the first column) is much smoother than the equivalent results from TDI processing (the second column)

even though the spatial resolution of the two methods is identical. This is consistent with the findings in the simulated heart.

2.3.2 Accumulated Axial Normal Strain

Proper accumulation is crucial for estimating peak deformation at the end of systole, an important parameter characterizing systolic function. Traditional TDI calculates accumulated strain by summing the strain from different tissue regions passing through a given pixel using Eq. (2.5). In contrast, 2-D ST follows the same tissue region using Eq. (2.11), accumulating displacements to compute the total deformation at that pixel. Accumulation of TDI results can be improved by tracing back along the axial direction [1]. This method is nearly equivalent to that used for 2-D ST with the lateral displacement set to zero in Eq. (2.11). The traditional and new TDI accumulation methods are denoted as TDI 0D and TDI 1D, respectively.

The Lagrangian accumulated axial normal strains at the end of systole from 2-D ST and TDI with the same spatial resolution are compared in Fig. 2.7 to the theoretical ones in the simulated heart. The accumulated strain derived from 2-D ST (Fig. 2.7 (b)), TDI 0D (Fig. 2.7(c)), and TDI 1D (Fig. 2.7(d)) are similar to the theoretical result (Fig. 2.7 (a)). However, the strain measured with 2-D ST (Fig. 2.7 (b)) is much smoother than both of the TDI methods (Fig. 2.7(c) and (d)). This is evidenced by the larger error and greater variance in accumulated axial normal strain error maps using TDI 0D and 1D (Fig. 2.8 (b) and (c)) compared to 2-D ST (Fig. 2.8 (a)). Approximating Lagrangian strain from natural strain using Eq. (2.6)

is one possible error source [11, 17]. On the left and right sides of the heart wall, which correspond to the location with large lateral motion shown in Fig. 2.9 (a), large biases are found for both of the TDI accumulation schemes. This finding confirms that by ignoring lateral motion during accumulation, TDI produces error. Compared to TDI 0D, TDI 1D accumulation removes large error at the top and bottom boundary of the heart (Fig. 2.7 (c) vs. Fig. 2.7 (d), Fig. 2.8 (b) vs. Fig. 2.8 (c)). The averaged error over the whole heart wall using TDI 0D is reduced from 14% to 8% using TDI 1D. 2-D ST further reduces this error to 2% by correctly estimating the lateral displacements (Fig. 2.9 (b) vs. Fig. 2.9 (a)) and registering motion during accumulation.

A similar comparison between different accumulation schemes was performed on data from the isolated rabbit heart with/without LAD ligation. Since TDI can only detect myocardial dysfunction along the beam direction, the anterior wall was orientated to face the probe directly. As expected, accumulated axial normal strain at the end of systole calculated using TDI and 2-D ST methods detected wall thinning (negative accumulated axial normal strain), shown in Fig. 2.10 (d), (e) and (f), after LAD ligation in the anterior wall in contrast to wall thickening (positive accumulated axial normal strain) in the corresponding region shown in Fig. 2.10 (a), (b) and (c) before LAD ligation. Similar to the findings in the simulated heart, the accumulated axial normal strain at the end of systole shown in Fig. 2.10 before (the first row) and after (the second row) LAD ligation using 2-D ST (the first column) has less local variance than those using both TDI 0D (the second column) and TDI 1D (the third column). Fig. 2.11 shows the

lateral displacements estimated in 2-D ST. The improvement of TDI 1D on the boundary is not as obvious as the finding in the simulated heart shown in Fig. 2.7 (c) and (d). A possible reason is that incorrect registration due to lateral displacement dominates in this case.

2.3.3 Principal Axes

The ability of 2-D ST to provide 2-D displacement maps minimally affected by beam angle helps to accurately characterize deformations at any point in the heart wall. In Fig. 2.12, we present the principal axes corresponding to the positive strain based on a decomposition of the deformation into principal stretches [4] in every pixel at the end of systole for the simulated heart. As shown in appendix A and Section 3.2.6, deformation at one point in a solid body can be fully characterized by strains based on the principal stretches along the principal axes. The principal axes and the strains are derived from accumulated displacements estimated using phase-sensitive speckle tracking using Eqs. (A-1), to (A-4) in appendix A. Section 3.2.6 and 3.3.3 demonstrates that the principal axes indicates the direction in which heart wall thickens (positive strain) or thins (negative strain), and directional changes of these principal axes can be used to detect abnormal motion due to LAD ligation. The principle axis map for 2-D ST shown in Fig. 2.12 (b) is well aligned along the radial direction of the annulus, indicating wall thickening along the radial direction or positive radial strain. The theoretical principal axis map is shown in Fig. 2.12 (a). Unlike 2-D ST, TDI can only measure the strain along the axial direction and produce only an approximate axial projection of the principal axes.

Fig. 2.13 (a) and (b) show the principal axes (also corresponding to positive strain based on the principal stretch) within the anterior wall before and after LAD ligation, respectively. The principal direction changes from radial in Fig. 2.13 (a) to almost circumferential in Fig. 2.13 (b), indicating that anterior wall thickening changes to wall thinning due to LAD ligation. The corresponding dot product map between the principal axis before and after occlusion (Fig. 2.13 (c)) of these principal axes (Fig. 2.13 (a) and Fig. 2.13 (b)) clearly illustrates the region with abnormal motion, which matches well with the region unstained by Evan's Blue (Fig. 2.13 (d)). This approach does not require ultrasound beam alignment with wall motion, as must be done with TDI.

2.4 Discussion

Auto-correlation based TDI and cross-correlation based 2-D ST using RF data are two major ultrasound techniques for quantitatively assessing myocardial mechanics. TDI is recognized as a 1-D method and can measure myocardial deformation only along the beam direction. TDI-based strain estimation suffers from decorrelation due to both axial motion and motion transverse to the beam direction, and exhibits low strain SNR because a high PRF is required to avoid aliasing in velocity estimation. 2-D ST was introduced to myocardial imaging to overcome these limitations by estimating 2-D in-plane displacements with moderate frame rates. In both principle and detail, these two methods are very different, directly affecting estimation accuracy, even of the same parameters. These differences must be noted when parameters such as axial normal strain and strain rate from either method are applied clinically for myocardial

contractility characterization. In this study, we illustrated different estimation accuracy for the two methods using a simulated heart and a well-controlled rabbit heart model based on a Langendorff preparation. The performance of each method to detect abnormal wall motion was further compared in a rabbit heart model of ischemia generated by ligating the LAD coronary artery. The tremendous advantage of 2-D ST for lesion detection, due to its reduced sensitivity to beam angle, was demonstrated by deriving the principal axes of deformation.

The results in Section 2.3.1 have demonstrated that instantaneous axial normal strain derived using TDI produces larger variance than strains derived using ST given the same spatial resolution, as shown in Figs. 2.3 and 2.4 on the simulated heart and in Fig. 2.6 on the isolated rabbit heart. In the simulation, the averaged error using TDI is about four times that using 2-D ST. There are two reasons for this difference. First, the frame rate of 2-D ST was only one third of the TDI PRF. In fact, by skipping more frames before strain-induced decorrelation starts to dominate the tracking performance, the strain SNR of 2-D ST can be further improved. Second, unlike 2-D ST, TDI does not follow the motion of the tissue when measuring the myocardial velocity and therefore suffers from further decorrelation. Even with spatial averaging to match 2-D ST's estimation resolution, TDI cannot reduce estimation variance to the extent that 2-D ST can by following the same speckle pattern between two images.

For clinical diagnosis, the operator must avoid myocardium with large transverse motion to minimize the effect of transverse motion on TDI

measurements. This requirement limits TDI's general applicability to myocardial disease diagnosis. In addition, further decorrelation may still result from translation of the tissue along the beam direction. As shown in Fig. 2.4 (b), even with small or zero lateral motion, the central part of the heart wall has large variance.

The results in Section 2.3.1 demonstrate that the Lagrangian accumulated axial normal strains derived using TDI (for both accumulation schemes) have larger bias and more variance than those using 2-D ST due to incorrect registration given that accumulation using TDI data cannot trace back along the same tissue's path. TDI 1D accumulation, restricted to the direction of the beam, removes error only at the top and bottom boundary of the heart. Significant bias is evident in accumulated axial normal strain error maps using both TDI 0D and TDI 1D (Fig. 2.8 (b) and (c)), resulting from large lateral displacement (Fig. 2.9). That is, TDI cannot avoid registration error from complex heart motion. To reduce this error, TDI is limited to myocardial segments with minimum lateral/transverse motion [21, 22, 11].

2-D ST can dramatically reduce registration error. It follows the same myocardium throughout motion, while TDI averages the deformation of different tissue segments passing through an image point to approximate the deformation of the original myocardial segment. This difference must be considered when the accumulated strain is used for clinical diagnosis since TDI may overestimate or underestimate contractility depending on the position of a pixel within the myocardial wall.

Another crucial advantage of 2-D ST is that tracking lateral displacement minimizes the dependency of lesion detection on beam angle. With 2-D displacement estimation, an in-plane strain tensor (strains based on principal stretches and corresponding principal axes, as detailed in [4]) can be derived to characterize regional myocardial contractility independent of beam direction. On the contrary, TDI can only provide (approximate) axial normal strains, the projection of the total deformation along the direction of the ultrasound beam. Directional changes in the principal axes before and after LAD ligation (see Fig. 2.13), available only with multi-dimensional ST, provide a strong indication of myocardial dysfunction. This is a robust method for determining the location of dysfunction [4].

TDI can provide higher temporal resolution for axial normal strain rate or axial normal strain by narrowing the field of view. At the same time, however, it suffers from low strain SNR due to the requirement of high PRF to avoid aliasing. 2-D ST using traditional 2-D image acquisition is applied to a larger field of view by sacrificing time resolution. Strain SNR can be increased by increasing the frame to frame interval [8] until speckle decorrelates due to large deformation. As demonstrated in this study, higher temporal sampling rates are possible for 2-D ST using an interleaved firing scheme (Fig. 2.2).

Clearly, TDI can be implemented in existing commercial ultrasound scanners more easily than full RF-based 2-D ST [1] and has a computational advantage since 2-D ST must compute the cross-correlation function and search for the peak of this function in 2-D. Nevertheless, with moderate hardware modifications,

2-D ST can also be realized in real time [23]. As these tools propagate into commercial scanners, we expect RF-based multi-dimensional speckle tracking will displace TDI as the preferred method for myocardial functional analysis.

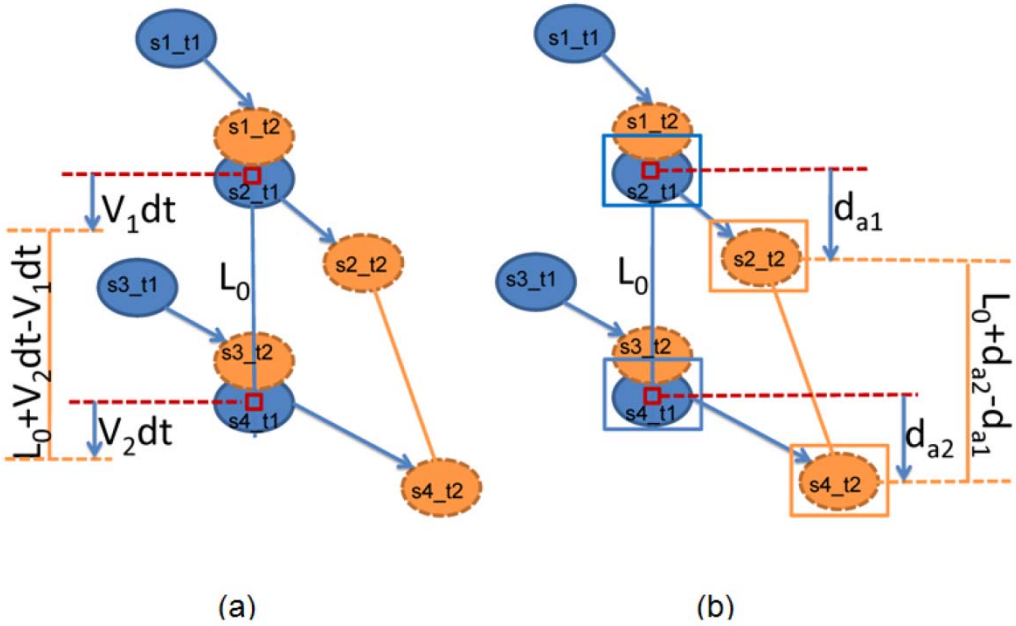

Figure 2.1 Axial normal strain estimation derived by TDI (a) and by 2-D ST (b). S1_t1 in blue means speckle 1 at time t1. S1_t2 in orange means speckle 1 at time t2. In TDI (a), V1 and V2 are TDI velocities of the interval dt = t2 − t1. The original axial distance between two points is L0. The axial distance changes to (L0+V2dt-V1dt). In 2-D ST (b), axial displacements (da1 and da2) of the same points labeled with red boxes are calculated by measuring the movement of speckles S2 and S4 shown in blue at time t1 and orange at time t2.

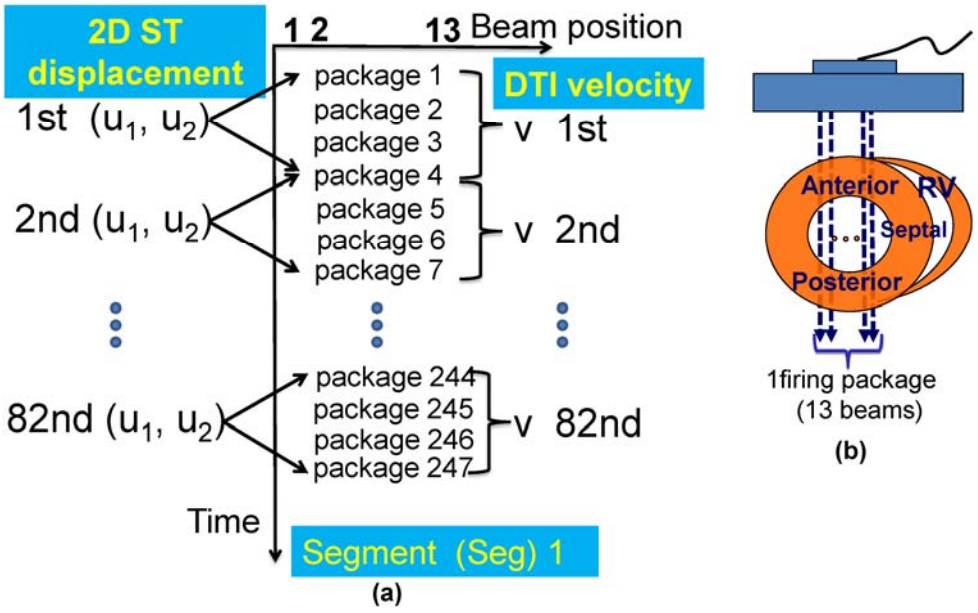

Figure 2.2 Experimental beam firing scheme. 2-D ST displacement and the corresponding TDI velocity were estimated with the scheme shown in (a) for segment 1.The beams are arranged in 17 segments (13 beams per segment as shown in (b)) which overlap each other to fully cover the whole heart.

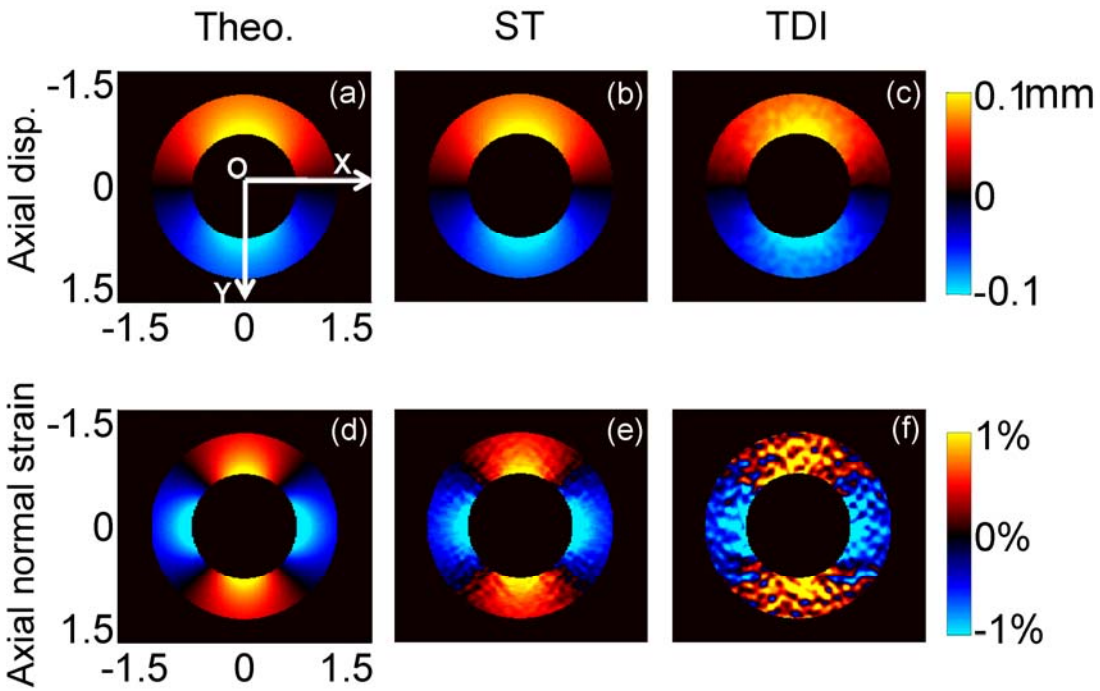

Figure 2.3 Axial displacements (the first row) and axial normal strain (the second row) for theory (the left column), 2-D ST (the middle column), and TDI (the right column). All spatial dimensions are in cm.

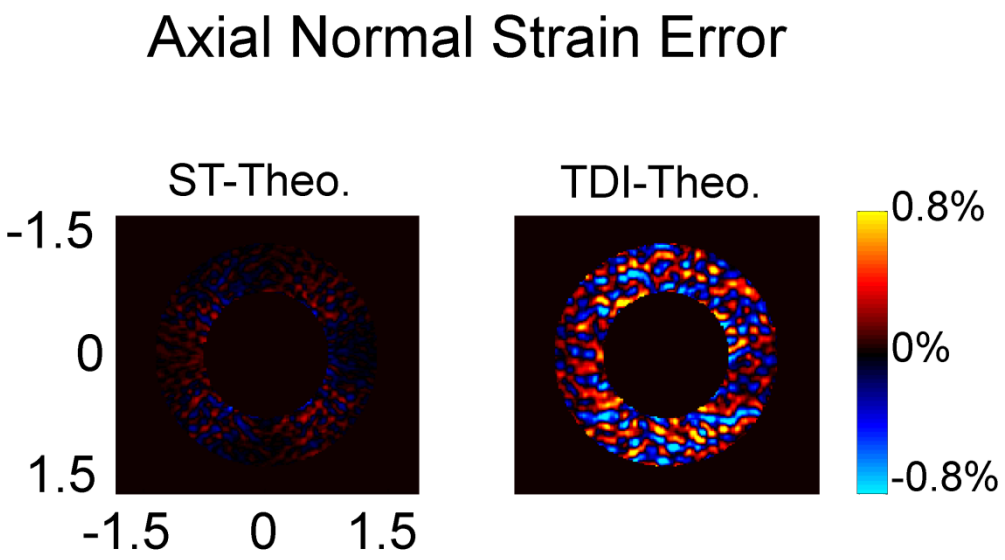

Figure 2.4 Axial normal strain error of 2-D ST (left) and TDI (right). All spatial dimensions are in cm.

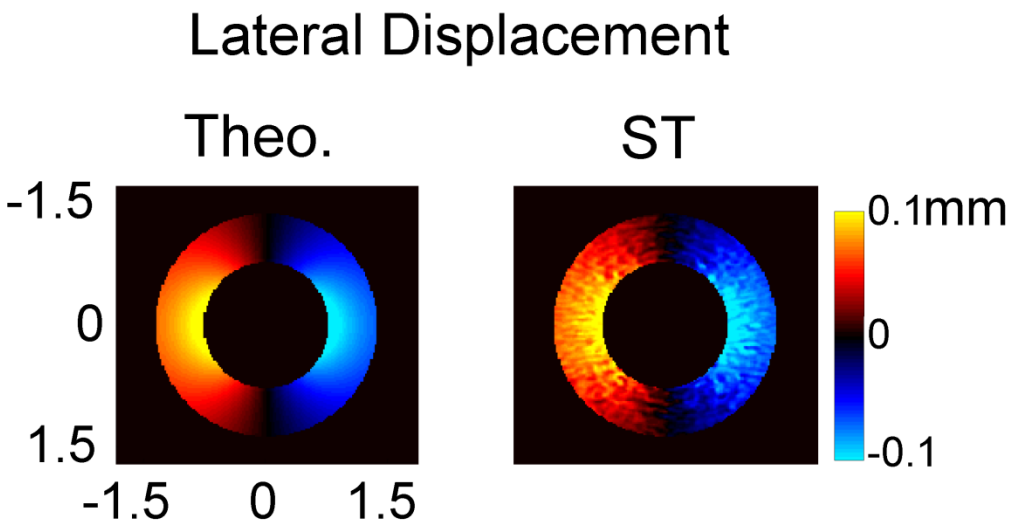

Figure 2.5 Theoretical lateral displacements (left) and corresponding 2-D ST results. All spatial dimensions are in cm.

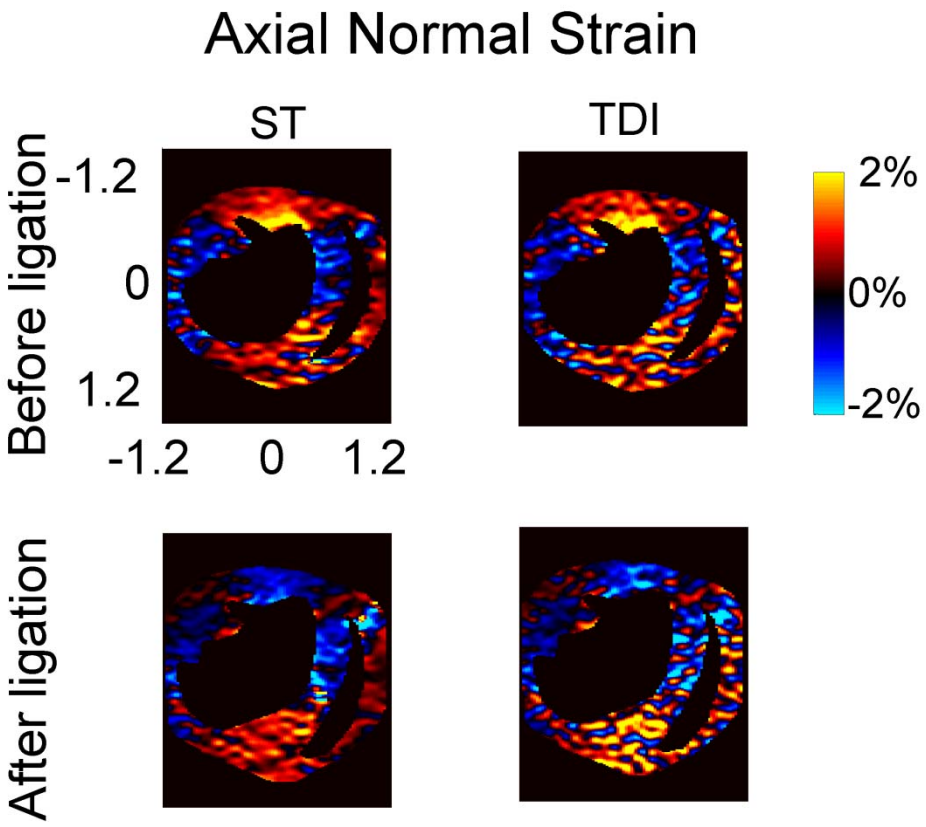

Figure 2.6 Axial normal strain before (first row) and after (second row) LAD ligation using 2-D ST (first column) and TDI (second column). The units of both axes are cm.

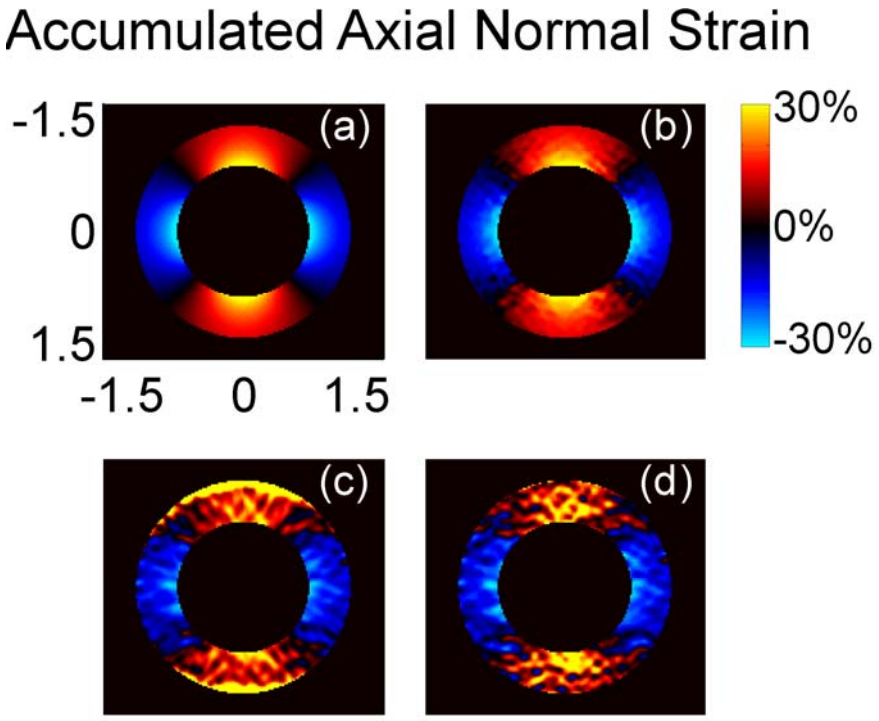

Figure 2.7 Theoretical accumulated axial normal strain (a) and corresponding axial normal strains derived from 2-D ST (b), TDI 0D (c), and TDI 1D (d).

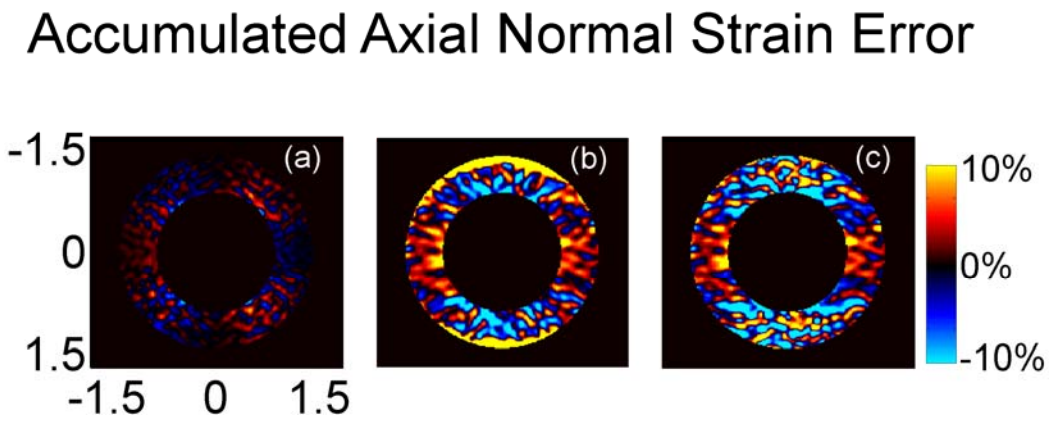

Figure 2.8 Comparison of the accumulated absolute axial normal strain error for 2-D ST (a), TDI 0D (b), and TDI 1D (c).

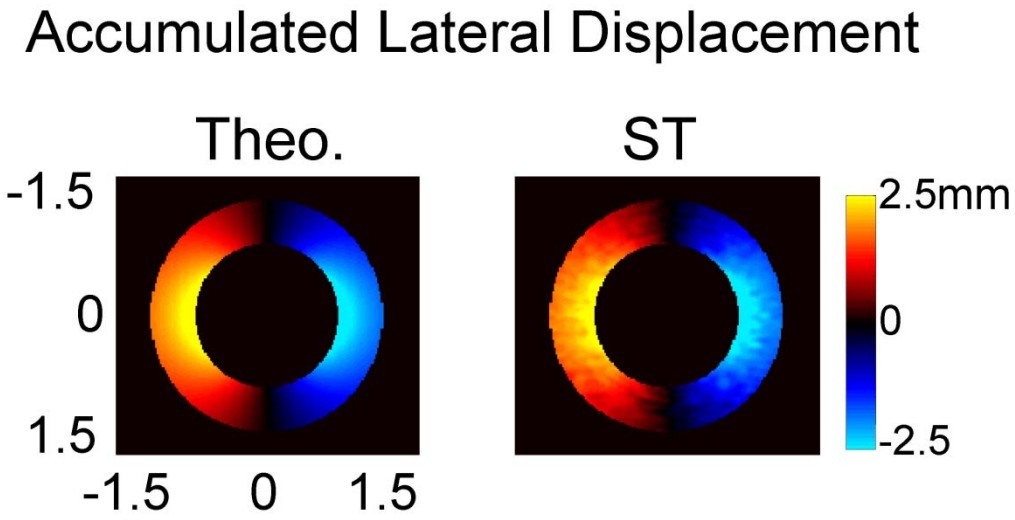

Figure 2.9 Theoretical accumulated lateral displacements (left) and the corresponding 2-D ST results (right).

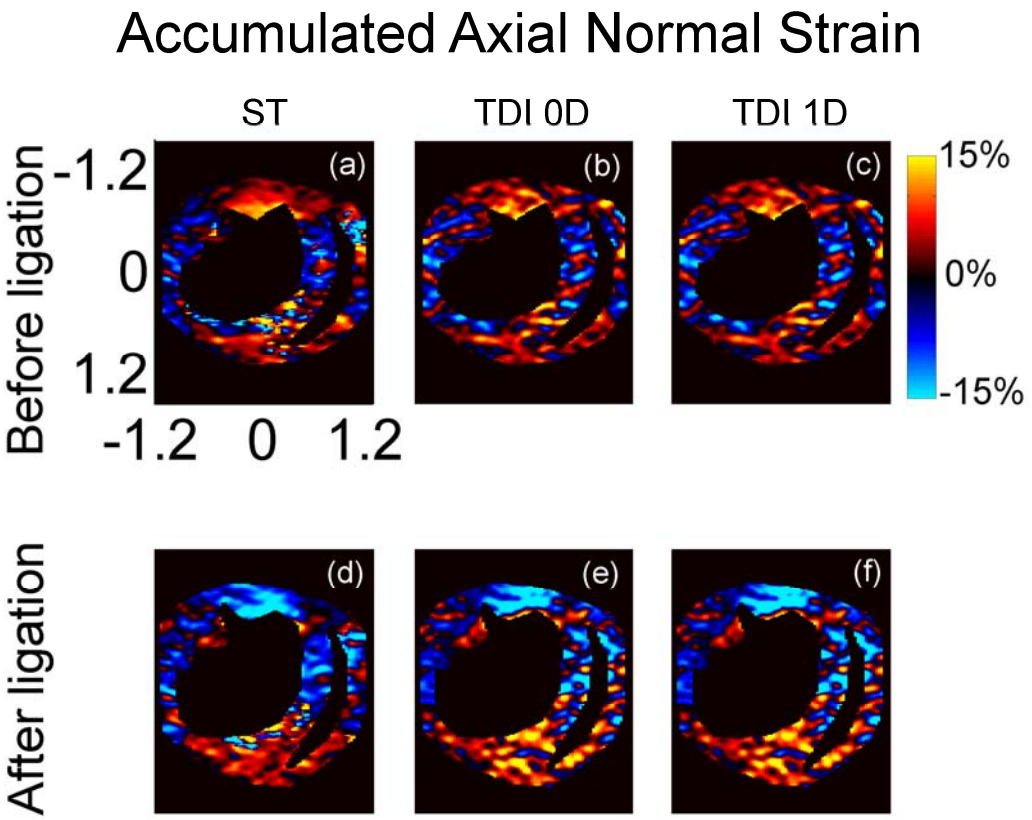

Figure 2.10 Accumulated axial normal strain before (first row) and after (second row) LAD ligation using 2-D ST (first column), TDI 0D (second column), and TDI 1D (the third column).

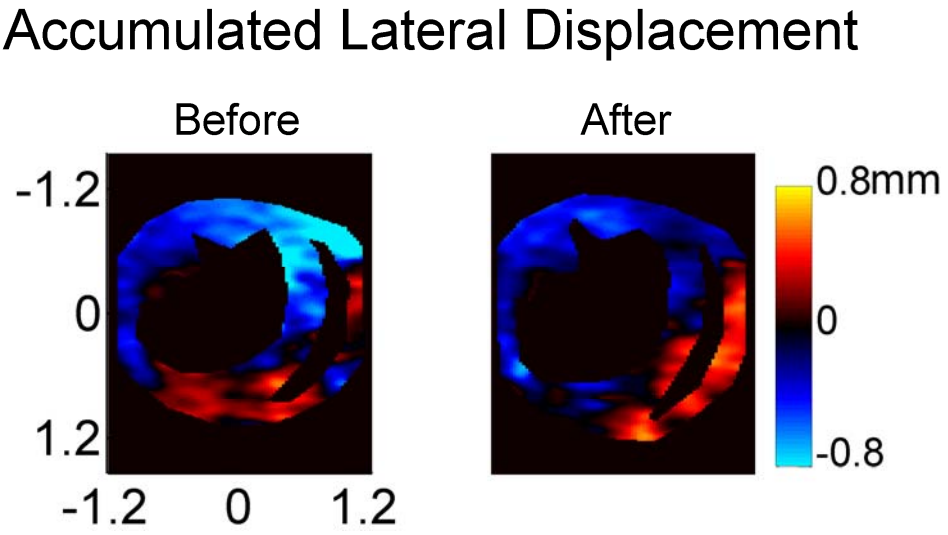

Figure 2.11 Accumulated lateral displacements before (left) and after (right) LAD ligation using 2-D ST.

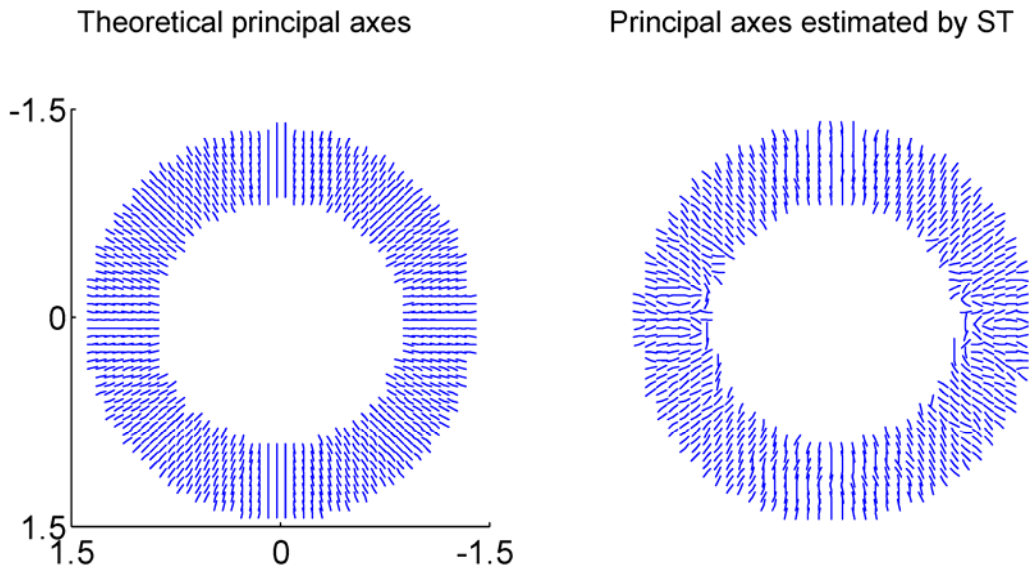

Figure 2.12 Comparison of principal axes of strain 1 (positive strain) based principal stretch (radial strain in this ideal case) between theory and 2-D ST for the simulated heart phantom.

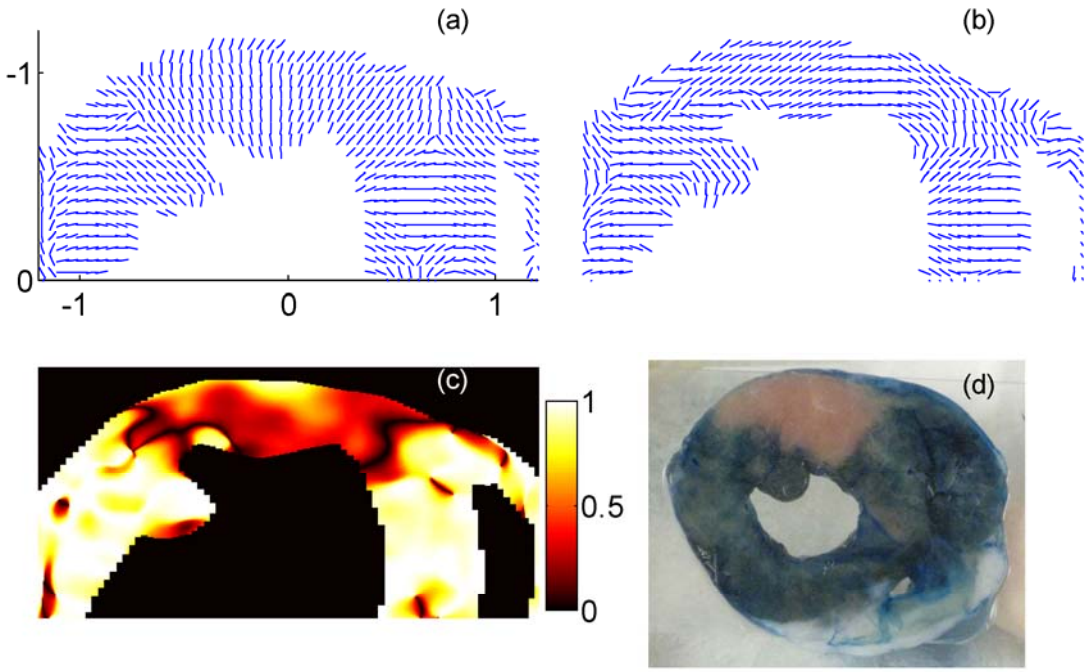

Figure 2.13 Principal axes of the primary deformation during systole before ligation (a), after ligation (b), and the dot product map (c) (of (a) and (b)) in the anterior wall, compared to Evan's blue staining slice (d).

2.5 References

[1] H. Torp, B. Olstad, A. Heimdal, and S. Bjaerum, “Method and apparatus for providing real-time calculation and display of tissue deformation in ultrasound imaging,” U.S. Patent 6 517 485 B2, Feb. 11, 2003.

[2] S. Bjaerum, H. Torp, and K. Kristoffersen**, “**High frame rate tissue Doppler imaging,” IEEE 2001 Ultrasonics Symposium Proceedings, pp. 1417-1421, Oct.07~Oct.10, 2001.

[3] X. Hua, T. Gauthier and A. T. Fernandez, “The role of local center frequency estimation in Doppler-based strain imaging”, IEEE 2007 Ultrasonics Symposium, pp.1965 – 1968, Oct.28-31 2007.

[4] C. Jia, R. Olafsson, K. Kim, T. J. Kolias, J. M. Rubin, H. Xie, and M. O'Donnell, “2D speckle tracking vs DTI-derived elasticity imaging on an isolated rabbit heart,” IEEE 2008 Ultrasonics Symposium Proceedings, vols.1-4 and Appendix, pp. 958-961, 2008.

[5] C. Kasai and K. Namekawa, “Real-time two-dimensional blood flow imaging using an autocorrelation technique,” IEEE 1985 Ultrasonics Symposium, pp.953-958, 1985.

[6] Bjorn A. J. Angelsen, “Ultrasound imaging. Waves, signals and signal processing.” Emantec AS, Trondheim, Norway. vol. II, ch 9 and 10, Dec. 2000.

[7] M. Uematsu, K. Miyatake, N. Tanaka, H. Matsuda, A. Sano, N. Yamazaki, M. Hirama, and M. Yamagishi, “Myocardial Velocity-Gradient as a New Indicator of Regional Left-Ventricular Contraction - Detection by a 2-Dimensional Tissue Doppler Imaging Technique, ” Journal of the American College of Cardiology, vol.26, no.1, pp.217-223, July 1995.

[8] K. Kaluzynski, X. C. Chen, S. Y. Emelianov, A. R. Skovoroda, and M. O'Donnell, “Strain rate imaging using two-dimensional speckle tracking,” IEEE Transactions on Ultrasonics Ferroelectrics and Frequency Control, vol.48, no.4, pp.1111-1123, July 2001.

[9] X. Chen, X. Li, D. Sahn, K. Kim, H. Xie and M. O’Donnell, “Evaluation of 2-D speckle tracking based strain rate imaging (SR) using a 3-D heart simulation model,” IEEE 2004 Ultrasonics Symposium Proceedings, vol. 3, pp. 2125-2128, Aug.23~27, 2004.

[10] I. Mirsky, D. N. Ghista, and H. Sandler, “Cardiac mechanics: physiological, clinical, and mathematical considerations,” John Wiley & Sons Inc., New York, 1974.

[11] G. R. Sutherland, L. Hatle, P. Claus, J. D’hooge and B. H. Bijnens, “Doppler myocardial imaging,” Belgium: BSWK, bvba, 2006, ch.3-4.

[12] S.-W. Huang, J. Rubin, H. Xie, R. Witte, C. Jia, R. Olafsson and M. O’Donnell, “Analysis of correlation coefficient filtering in elasticity imaging,” IEEE Trans. Ultrason., Ferroelect., Freq. Contr., vol. 55, no. 11, pp. 2426-2441, Nov. 2008.

[13] X. Zhong, M. A. Lubinski, N. Sanghvi, M. O'Donnell and C. A. Cain, "Speckle tracking and motion compensation for ultrasound-based lesion localization", IEEE 1997 Ultrasonics Symposium Proceedings, vol. 2, pp. 1381-1384, Oct.5~8, 1997.

[14] C. Jia, R. Olafsson, K. Kim, T. Kolias, J. Rubin, W. Weitzel, R. Witte, S.-W. Huang, M. Richards, C. Deng and M. O'Donnell, "Two-dimensional strain imaging of controlled rabbit hearts," Ultrasound in Medicine & Biology, vol.35, no.9, pp. 1488-1501, Sep. 2009.

[15] M. A. Lubinski, S. Y. Emelianov, and M. O'Donnell, "Speckle tracking methods for ultrasonic elasticity imaging using short time correlation," IEEE Trans. Ultrason., Ferroelect., Freq. Contr., vol. 46, pp. 82-96, Jan. 1999.

[16] M. A. Lubinski, S. Y. Emelianov, K. R. Raghavan, A. E. Yagle, A. R. Skovoroda, and M. O'Donnell, "Lateral displacement estimation using tissue incompressibility," IEEE Trans. Ultrason., Ferroelect., Freq. Contr., vol. 43, pp. 247-255, Mar. 1996.

[17] R. Richards, "Principles of solid mechanics," CRC press LLC, New York, 2001, pp.181-183.

[18] Y. Petrank, L. Huang, and M. O'Donnell, "Reduced peak hopping artifacts in ultrasonic strain estimation using Viterbi algorithm," IEEE Trans. Ultrason., Ferroelect., Freq. Contr., vol. 56, no. 7, pp. 1359-1367, Jul. 2009.

[19] N. A. Cohn, S. Y. Emelianov, and M. O'Donnell, "An elasticity microscope part II: experimental results," IEEE Trans. Ultrason., Ferroelect., Freq. Contr., vol.44, pp. 1320-1331, 1997.

[20] E. A. Booth, N. R. Obeid, and B. R. Lucchesi, "Activation of estrogen receptor-alpha protects the in vivo rabbit heart from ischemia-reperfusion injury," American Journal of Physiology-Heart and Circulatory Physiology, vol. 289, no. 5, pp. H2039-H2047, 2005.

[21] J. D'hooge, B. Bijnens, J. Thoen, F. Van de Werf, G. R. Sutherland, and P. Suetens, "Echocardiographic strain and strain-rate imaging: A new tool to study regional myocardial function," IEEE Transactions on Medical Imaging, vol.21, no.9, pp.1022-1030, Sep. 2002.

[22] J. D'hooge, A. Heimdal, F. Jamal, T. Kukulski, B. Bijnens, F. Rademakers, L. Hatle, P. Suetens, and G.R. Sutherland, "Regional strain and strain rate measurements by cardiac ultrasound: principles, implementation and limitations," European Journal of Echocardiography, vol.1, no.3, pp.154-170, 2000.

[23] J. Hamilton, M. O'Donnell and T. J. Kolias, "Real-time imaging of cardiac mechanical function using ultrasound," 2008 International Conference on the Ultrasonic Measurement and Imaging of Tissue Elasticity.

Chapter 3 Two-dimensional Strain Imaging of Controlled Rabbit Hearts

3.1 Introduction

Chapter 2 compared TDI-derived tracking to 2-D phase sensitive speckle tracking in terms of the accuracy of estimating both instantaneous axial normal strain and accumulated axial normal strain. Unlike TDI, which is limited by the beam propagation direction, 2-D ST's ability to provide 2-D displacement maps helps to characterize deformations at any point in the heart wall with low dependency on beam angle.

In this chapter[1], we describe a well controlled *in-vitro* experiment on an isolated rabbit heart paced from the apex. Two coplanar and orthogonal linear probes were used to acquire RF data. LV pressure and electrocardiogram (ECG) signals were recorded and synchronized with ultrasound RF data acquisition using a field programmable gate array (FPGA). Acute ischemia was generated by ligating the LAD coronary artery on an isolated Langendorff retroperfused rabbit heart. Results from a single probe show that systolic bulging of the heart wall due to LAD ligation can be detected by significant directional changes (about 90^{o}) in the principal axes. As indicated by the principal axes, muscle fibers during systole actively shorten primarily along the heart's circumferential direction producing heart wall thickening primarily along the heart's radial direction before LAD ligation. After ligation, fibers are passively stretched primarily along the

heart's circumferential direction by surrounding muscles, leading to heart wall thinning approximately along the heart's radial direction in the area perfused by the LAD. In addition, decreased myocardial contractility due to 2,3-butanedione monoxime (BDM) was detected by decreased strain magnitude. Results derived using asymmetric displacement accuracy from a single probe were also compared to those derived using symmetric displacement accuracy (i.e., dual probe measurements using only accurate axial tracking information from each). Identification of the ischemic region using directional changes of the principal axes was further validated by Evans Blue staining.

3.2 Materials and Methods

3.2.1 Langendorff Rabbit Heart Preparations

One adult New Zealand white rabbit was used. The experiment was performed according to a protocol approved by the University of Michigan Committee on the Use and Care of Animals. The rabbit received veterinary care provided by the University of Michigan Unit for Laboratory Animal Medicine. The University of Michigan is authorized by the American Association of Accreditation of Laboratory Animal Health Care and the animal care use program is in compliance with the standards in The Guide for the Care and Use of Laboratory Animals.

The rabbit was anesthetized by intramuscular injection of Ketamine (35mg/kg) and Xylazine (5mg/kg). As soon as the rabbit was euthanized by injecting sodium pentobarbital (100 mg/kg), heparin (500U/kg) was injected into

the left marginal ear vein to prevent clot formation. The heart was rapidly excised and mounted on a Langendorff setup. It was retroperfused with modified, oxygenated Krebs-Henseleit (K-H) buffer (pH 7.4; 37°C; 95% O_2/5% CO_2) through the aorta with perfusion pressure 35 – 40 mm/Hg. The modified K-H buffer [2] contained in mM: 117 NaCl, 4 KCl, 1.2 $MgCl_2$•$6H_2O$, 1.1 KH_2PO_4, 5.0 glucose, 25 $NaHCO_3$, and 2.6 $CaCl_2$•$2H_2O$.

3.2.2 Experimental Setup

To overcome the rabbit's natural heart beat and synchronize data acquisition, the heart was paced at 3Hz from its apex with two electrodes (Fig. 3.1). They were made of Teflon insulated tungsten wires (A-M System Inc., Carlsborg, WA, USA) and attached to a function generator (5V, 500μs square pulse, HP33120A, Agilent Technologies, Santa Clara, CA, USA). The ECG signal was recorded using three electrodes; two, made of Teflon insulated tungsten wires, were placed at the top and bottom of the bath; the third silver wire was submerged in the perfusion solution near the aorta. The ECG signal was filtered through a differential amplifier with gain of 1000 and bandwidth of 1-3000 Hz (AM502, Tektronix, Richardson, TX, USA).

The LV pressure was recorded with a pressure meter (Alicat Scientific Inc., Tucson, AZ) through a latex balloon. The balloon was inserted via the left atrium into the LV, secured with a silk string at the left atrial appendage, and then expanded with a small amount of water to achieve an LV end-diastolic pressure of 10 mmHg. Measured LV pressure was 10-60mmHg, well within the heart's

physiological working range. The balloon itself, however, was not fully inflated and with the water inside was still deformable. Therefore the balloon introduced minimal elasticity effects on myocardial deformation. The measured LV pressure was filtered through a second differential amplifier with gain of 50 and bandwidth of 0.1-3000 Hz (AM502, Tektronix). Both ECG and LV pressure signals were digitized simultaneously using an oscilloscope (TDS1002, Tektronix) and transferred to a computer using a general purpose interface bus (GPIB).

Two linear array probes connected to a commercial ultrasound (US) scanner (SonixRP, Ultrasonix, Richmond, BC, Canada) were coplanar and orthogonally positioned below the LAD ligation position to acquire RF data from a short-axis view (Fig. 3.2). An FPGA chip (ezFPGA-C6-6, Dallas Logic, Plano, TX, USA) was programmed to synchronize the pacing signal, LV pressure, ECG signal, and RF data capture. The frame rate of the US machine in this experiment was 123 Hz (41 frames per heart cycle). This was the highest frame rate available with this commercial scanner for the field of view used and the requirement of full synchrony with the pacing signal. This frame rate is not as high as cited in other studies [3] but it is sufficient here because out-of-plane motion was minimized by attaching the heart to the fixed pacing wire at the apex. The average correlation coefficient for frame to frame tracking was above 0.8 except for one interval of high strain rate during early systole in which the average coefficient fell to about 0.7.

To co-register the two fields of view, a wire perpendicular to the image plane was used to register the image planes from each probe after the probes were

clamped in a holder with two 90^o legs. The wire was first placed in the lateral center of each probe, then translated 3 steps in x and y directions independently with a step size of 5mm (i.e., nine total positions). Images were recorded at each position and used to construct a 3x3 composite point image for each probe. The center point was used to locate the image center. One 3 by 3 point image from one probe was also rotated 90^o to check if it would overlap the other 3 by 3 point image from the second probe. Alignment was maintained to 0.15 mm and orthogonality to 0.5^o.

Both linear probes used in this setup have a central frequency of 5 MHz, sampling frequency of 40MHz, and 128 elements with a pitch of 0.3 mm. Two coordinate systems (global coordinates and scanner coordinates) were used, as shown in Fig. 3.2 with the anterior wall on the upper left corner (Fig. 3.2 (a)). In global coordinates, the X_1-axis was defined as the horizontal direction and the X_2-axis is defined as the vertical direction. In scanner coordinates, the axial direction is defined along the beam propagation direction, and the lateral direction is perpendicular to the beam propagation direction for each probe. Since the probes were orthogonal to each other, the X_1-axis in global coordinates is the lateral direction of probe 1 and the axial direction of probe 2; the X_2-axis is the axial direction of probe 1 and the lateral direction of probe 2.

3.2.3 Experimental Procedure

The experimental procedure was divided into four stages. In the first three, LV pressure, ECG and RF data were monitored and recorded. In the final stage,

Evans Blue staining was used to find the nonperfused area (area at risk) due to LAD ligation.

Stage 1: The rabbit heart was retroperfused with modified K-H solution. The heart wall contracted synchronously with the pacing signal.

Stage 2: The rabbit heart was retroperfused with both K-H solution and 4mM BDM. Maximum contraction was decreased with increasing BDM concentration.

Stage 3: Acute ischemia was produced by ligating the LAD with a silk suture. The heart was retroperfused with only K-H solution or K-H solution including 4mM BDM, which will be discussed in the next section (BDM regulation). RF data were acquired from both probes several minutes after LAD ligation. RF data obtained in stages 1, 2 and 3 were processed offline. Strains and their corresponding principal axes were estimated from these RF data obtained before and after ligation.

Stage 4: Evans Blue staining was used to identify nonperfused areas: areas at risk.

The heart was detached from the Langendorff perfusion system. 2ml of 0.4% Evans Blue was retroperfused into the heart for about 10 seconds until the heart was stained uniformly [4]. The heart was then cut around the imaging plane corresponding to the short-axis view used for all experiments. Optical images of the stained cross section were used to validate the abnormal region determined

by principal axes analysis. The unstained area was the area at risk due to LAD ligation [4].

3.2.4 BDM Regulation

BDM is an excitation-contraction decoupler, 2,3-butanedione monoxime, which can reversibly reduce the maximum deformation [5]. In other words, BDM can reduce heart muscles' contractility. The higher the concentration of BDM, the more contractility will be reduced. In the experiment, 4mM BDM was retroperfused into the heart along with oxygenated modified K-H solution to partially reduce the heart muscles' contractility.

3.2.5 2-D Speckle Tracking

As mentioned above, each of two coplanar, orthogonal linear probes acquired forty one frames (one RF data set) in one heart cycle. Correlation-based phase-sensitive 2-D speckle tracking [6] was applied to estimate the cardiac contraction between every two consecutive frames in each data set. The tracking algorithm first calculated the complex cross-correlation coefficient between speckle-sized blocks from two consecutive frames. The correlation coefficient functions were then filtered using a 2-D Hanning window to reduce tracking error and peak hopping.

In this study, the correlation kernel, corresponding to one speckle spot, was 1.50 mm x 0.24 mm (lateral x axial) and the filter size was 2.10 mm x 1.22 mm (lateral x axial). Axial and lateral displacements were initially estimated by finding

the peak position of the magnitude of the filtered correlation coefficient function using a parabolic fit. The axial displacement was further refined by calculating the position of the phase zero-crossing around the peak correlation coefficient. Since there is no phase information in the lateral direction, lateral displacement estimates have much larger variance than axial ones [7].

Estimated displacements between two consecutive frames were then integrated frame by frame to obtain the accumulated displacements relative to a reference frame. In this study, the reference frame was chosen at the beginning of systole (downward arrow in Fig. 3.3 (c) and (d)) and displacements were accumulated until peak systole (upward arrow in Fig. 3.3 (c) and (d)). Ultimately, the axial displacement estimate had a higher spatial resolution of about 1.24 mm and the lateral displacement estimate had a resolution of about 2.58 mm, considering the combined effects of kernel and filter sizes. The thickness of heart wall was about 4-5mm. Finally, the deformation gradient tensor was computed using Eq. (A-1) by spatially differentiating accumulated displacements to derive principal axes and strains based on the principal stretches along these axes. Details are described in the next section.

3.2.6 Strains Based on the Principal Stretches and Corresponding Principal Axes

In continuum mechanics, deformation at one point in a solid body can be fully characterized by strains based on the principal stretches along the principal axes, where a proper coordinate rotation eliminates all shear components. The principal axes and corresponding strains fully describe the deformation at that

point independent of coordinate system. In this study, we use strains based on the principal stretches to characterize contractility and directional changes of their principal axes to detect abnormal motion due to LAD ligation.

As shown in appendix A, the deformation gradient tensor using Eq. (A-1) is calculated by first spatially differentiating accumulated displacements estimated using phase-sensitive speckle tracking. Then, the right Cauchy deformation tensor $\mathbf{C}$ was calculated using Eq. (A-2). As shown in Eqs. (A-3) and (A-4), by calculating the eigenvalues and eigenvectors of this tensor, the square of two in-plane principal stretches (λ_1 and λ_2) and their principal axes ($\mathbf{v}_1$ and $\mathbf{v}_2$) in the orthogonal matrix $\mathbf{\Omega}$ are obtained. Note that principal axes defined here are bidirectional. That is, $\mathbf{v}_1$ and $-\mathbf{v}_1$ represent the same axis.

The strains based on the principal stretches at a point within the solid body are defined as ($\lambda_1 - 1$) and ($\lambda_2 - 1$) at that point along the principal axes $\mathbf{v}_1$ and $\mathbf{v}_2$, respectively. If one strain is larger than zero, then the solid body at this point lengthens along the corresponding principal axis. If negative, the solid body at this point shortens along the principal axis. Note that the strains ($\lambda_1 - 1$) and ($\lambda_2 - 1$) based on the principal stretches have the same corresponding principal axes as the principal strains (ε_1 and ε_2) calculated using Eqs. (A-5) and (A-6). However, they have different values as shown in Eqs. (A-7) and (A-8) and different physical meanings.

As illustrated in Fig. A-1 and Eq. (A-9), (λ_1 -1) and (λ_2 -1) quantify the shortening (-) or lengthening (+) of the original element along the principal axes as a fraction of the original length. Principal strains ε_1 and ε_2 as shown in Eq. (A-8) will overestimate or underestimate this fractional change. When the deformation is small, the principal strains approximately equal the strains based on the principal stretches along the principal axes.

$$\begin{aligned} \varepsilon_1 &\approx \lambda_1 - 1 \\ \varepsilon_2 &\approx \lambda_2 - 1. \end{aligned} \tag{3.1}$$

However, the accumulated strain at the end of systole is not small. Strains based on the principal stretches ($\lambda_1 - 1$) and ($\lambda_2 - 1$) along the principal axes are more accurate parameters for characterizing cardiac deformation. So we propose to use the strains (λ_1 -1) and (λ_2 -1) along the principal axes $\mathbf{v}_1$ and $\mathbf{v}_2$ to characterize heart muscle contractility in this study. For convenience, we define $\lambda_1 > \lambda_2$ for the rest of the paper.

The accuracy and resolution of axial and lateral displacements estimated by speckle tracking will affect the accuracy of principal axes estimates and corresponding strains, because displacements are used directly to calculate deformation gradient tensor components, as shown in Eq. (A-1). As mentioned above, the lateral component has lower spatial resolution and less estimation precision than the axial component. To further investigate the effects of asymmetric displacement estimation and explore optimal methods using multi-dimensional speckle tracking, we also compare single probe results with those

derived using both axial displacements from two orthogonal and coplanar linear probes.

In summary, three methods were used:

Method 1: lateral and axial displacements derived exclusively from probe 1 data. u_1 and u_2 in Eq. (A-1) are the lateral and axial displacement components of probe 1, respectively, as shown in Fig. 3.2.

Method 2: lateral and axial displacements derived exclusively from probe 2 data. u_1 and u_2 in Eq. (A-1) are the axial and lateral displacement components of probe 2, respectively, as shown in Fig. 3.2.

Method 3: axial displacements from probe 1 and probe 2 are used. u_1 is the axial displacement of probe 2 and u_2 is the axial displacement of probe 1, as shown in Fig. 3.2.

3.3 Results

3.3.1 ECG Signal and LV Pressure

ECG and LV pressure before and after LAD ligation are shown in Fig. 3.3 for two perfusion conditions: only modified K-H solution (blue) and modified K-H solution with 4 mM BDM (red). Note that the peak at time zero in the ECG figures is a pacing artifact. When the heart was correctly paced, each cycle was 1/3 second. The time lag between excitation, indicated by the ECG signal, and contraction, indicated by LV pressure, remained the same for all conditions (as shown in Fig. 3.3 (a) and (c), Fig. 3.3 (b) and (d)). The morphology of ECG

signals in Fig. 3.3 (a) was similar for different BDM concentrations before LAD ligation. The same phenomena can also be observed in Fig. 3.3 (b) after LAD ligation. However, the morphology of the ECG signals before and after ligation was slightly different. The reason is probably that muscle fibers perfused by the LAD no longer actively contracted and conduction was altered after ligation.

As discussed in the previous section (BDM Regulation), BDM was used to reduce heart muscles' contractility. This effect of BDM was clearly demonstrated by the LV pressure. As shown in Fig. 3.3 (c), LV pressure was reduced by about 25% in the heart retroperfused with K-H solution including 4 mM BDM (red) compared to that measured when the heart was retroperfused with only K-H solution (blue). After ligation, LV pressure was reduced by about 50% by BDM as shown in Fig. 3.3 (d). The duration between the two arrows in Fig. 3.3 (c) and (d) was defined as systole in this study.

3.3.2 2-D Displacement Estimates using 2-D Speckle Tracking

Results from a single probe presented in this section were further validated using the results from two probes. To closely compare single probe to dual probe performance, we present results from both systems together.

B-mode images acquired using the two linear arrays before and after ligation when the heart was perfused in modified K-H solution are registered in the global coordinates shown in Fig. 3.4 with the anterior wall on the upper left corner as shown in Fig. 3.4 (d). The first column presents B-mode images before ligation, while the second column contains B-mode images after ligation. The first row

was acquired with probe 1 at the top and the second row was acquired with probe 2 on the left. After LAD ligation, abnormal motion in the anterior wall highlighted in Fig. 3.4 (b) was observed in the B-mode movie (movie 3.1). Compared to the synchronous global contraction of the heart before ligation, the anterior wall in the highlighted area after LAD ligation lost its local active contraction and bulged out during systole instead of thickening in the radial direction. This abnormal area matched the perfusion area of the LAD.

Results at the end of systole referenced to the first frame at the beginning of systole are presented and analyzed in the following section. To avoid being distracted by surrounding artifacts, masks are manually generated according to the contour of the corresponding first B-mode image during systole and applied to subsequent results.

Lagrangian displacement estimates using 2-D speckle tracking at the end of systole before ligation when the heart was retroperfused using only modified K-H solution are shown in Fig. 3.5. The first column is the displacement u_1 along the X_1-axis. The second column is the displacement u_2 along the X_2-axis. The first row presents results calculated using data from probe 1 at top and the second row is calculated using data from probe 2 on the left. Since the two probes were rotated 90^o with respect to each other, the same u_1 along X_1-axis was estimated by probe 1 as the lateral displacement (Fig. 3.5 (a)) and by probe 2 as the axial displacement (Fig. 3.5 (c)). The same u_2 along X_2-axis was estimated by probe 1 as the axial displacement (Fig. 3.5 (b)) and by probe 2 as the lateral displacement (Fig. 3.5 (d)).

As expected, displacement estimates u_1 in Fig. 3.5 (a) and (c) (u_2 in Fig. 3.5 (b) and (d)) from the two probes have similar patterns, demonstrating the probe setup is aligned properly. However, axial displacement estimates are smoother than lateral ones, as displacement components estimated along a probe's lateral direction (Fig. 3.5 (a) and Fig. 3.5 (d)) show larger local variations. These variations are most evident when spatial derivatives of the lateral displacement are computed to produce components of the local strain tensor. The same phenomena can also be observed in tracking results after ligation for modified K-H, and for modified K-H plus 4 mM BDM. Consequently, the corresponding images for these cases are not included.

3.3.3 Strains Based on the Principal Stretches and Corresponding Principal Axes

As discussed in the corresponding section under Materials and Methods, the deformation at any position within the heart wall can be characterized by principal axes ($\mathbf{v}_1$ and $\mathbf{v}_2$) with corresponding strains based on the principal stretches along them (($\lambda_1 - 1$) and ($\lambda_2 - 1$) with $\lambda_1 > \lambda_2$). The strain ($\lambda_1 - 1$) before and after ligation at the end of the systole is presented in Fig. 3.6 for different probe combinations when the heart was perfused with only modified K-H perfusion solution. The first column shows results before ligation, and the second column after ligation. The first row presents results from probe 1, the second row from probe 2, and the third row from combined axial displacement estimates from both probes. The highlighted area denotes the region of abnormal motion observed in the B-mode movie.

As is evident from these figures and movies, ($\lambda_1 - 1$) is positive over most of the heart wall, especially when axial displacement estimates from both probes are combined. Positive values mean the myocardium lengthens along the principal axis $\mathbf{v}_1$. Images of this principal axis's direction are color coded from -90^o to 90^o as shown in the colormap in Fig. 3.7 (g). The brightness of each color was modulated by the magnitude of the strain using the shifted sigmoid function shown in Fig. 3.7 (h). The principal axis directions calculated using different probe combinations are similar at all positions either before (Fig. 3.7 (a), (c) and (e)) or after ligation (Fig. 3.7 (b), (d) and (f)).

Results from the single probes after and before ligation (Fig. 3.7 (b) and (d) versus Fig. 3.7 (a) and (c)) clearly demonstrate about a 90^o rotation of the principal axes of ($\lambda_1 - 1$) in the center of the highlighted region. These results match those obtained from two probes (Fig. 3.7 (f) versus Fig. 3.7 (e)). However, the shapes of the area with this direction change in single probe images are slightly different from that in the two probe image. The principal axes from single probes also have more direction variation in the septum region compared to those from two probes. This is mainly due to the large variation in lateral displacement estimation from single probe data, and also the relatively complex contraction of the septum sitting between left and right ventricles.

This directional change is better observed in a zoom of the highlighted area in Fig. 3.8. Here, a vector presenting the direction of the principal axis is superimposed on the color-coded image. The principal axis $\mathbf{v}_1$ is primarily in a

direction perpendicular to the heart wall before ligation and changes to be primarily in a direction parallel to the heart wall after ligation. In other words, the heart wall thickens primarily in a direction perpendicular to the heart wall before ligation due to active shortening of muscle fibers, and changes to be passively stretched by surrounding muscles primarily in a direction parallel to the heart wall after ligation in this highlighted area. This is consistent with findings by Villarreal [8] that myocardium in ischemic regions will change from radial directional thickening to circumferential directional stretching during systole. Note that estimation of strains based on principal stretches and principal axes does not require a centroid; it is only related to the deformation condition at that point.

The second strain ($\lambda_2 - 1$) before and after ligation at the end of systole for only the modified K-H solution is shown in Fig. 3.9 for all probe combinations. The figure layout is identical to that of Fig. 3.6. The strain ($\lambda_2 - 1$) is negative over most of the heart wall, which means that the myocardium shortens along principal axis $\mathbf{v}_2$. Since $\mathbf{v}_2$ is perpendicular to $\mathbf{v}_1$, as demonstrated in appendix A, we only provide the principal axes $\mathbf{v}_2$ in the highlighted area in Fig. 3.10.

Similar to $\mathbf{v}_1$, principal axis $\mathbf{v}_2$ indicated that myocardium in the highlighted area actively shortens approximately parallel to the heart wall before ligation but changes to thinning approximately perpendicular to the heart wall after ligation due to stretching by surrounding muscles. This can also be interpreted as myocardium in the ischemic region changing from active circumferential

directional shortening before ligation to passive radial directional thinning during systole after ligation, similar to Villarreal et al.'s findings [8].

Similar trends are observed when the heart was retroperfused with K-H perfusion solution including 4 mM BDM, but with expected reduced overall deformation magnitude. Under both perfusion conditions, muscle fibers in the highlighted region during systole actively shorten primarily along the heart's circumferential direction and thicken primarily along the heart's radial direction before LAD ligation. After ligation, fibers are passively stretched primarily along the heart's circumferential direction by surrounding muscles, leading to the heart wall's thinning approximately along the heart's radial direction.

The decrease of the overall myocardium's contractility due to BDM is observed by the decrease of strains along their principal directions. This decrease can also be found quantitatively in the averaged strains ($\lambda_1 - 1$), ($\lambda_2 - 1$) and strain magnitude $\sqrt{(\lambda_1 - 1)^2 + (\lambda_2 - 1)^2}$ in the highlighted region (shown in Fig. 3.6) at the end of systole before ligation for both types of solution shown in Table 1. The averaged strains for K-H solution including 4 mM BDM decrease to 40%-60% of that for only K-H solution. The variance of the calculation is relatively large partly because the segment covers the entire heart wall from endocardium to epicardium.

Directional changes of the principal axes also can be presented as the dot product of principal axes $\mathbf{v}_1$ before and $\mathbf{v}_1$ after LAD ligation in the highlighted region, as shown in Fig. 3.11 (a)-(c) for only K-H solution. A value of one in these

images means that the principal axes before ligation and after ligation are the same/parallel while zero means they are perpendicular to each other. The region with the directional changes of principal axes can be observed in the upper left corner for different probe combinations. Compared to Fig. 3.11 (c) using two probes, the single probe results (Fig. 3.11 (a) and (b)) have more shape variation because of the large variance in the lateral displacement estimates for single probe data. In other words, the accuracy and precision of single probe results tends to be sensitive to probe orientation.

3.3.4 Evans Blue Staining

Fig. 3.11 (d) presents an optical photograph of the heart stained with Evans Blue at the cross section corresponding to the ultrasound results presented above. The upper left area has substantially less staining due to LAD ligation. This area at risk identified by Evans Blue staining matches well to the abnormal area (Fig. 3.11 (a)-(c)) estimated by measurements of the directional change in the principal axis.

3.4 Discussion

In this chapter, a well-controlled 2-D cardiac elasticity imaging technique was developed to test the capability of multi-dimensional speckle tracking for detection of deformation abnormalities due to myocardial ischemia. Two coplanar and orthogonal linear probes were used to simultaneously image an isolated retroperfused rabbit heart. A segmental dyskinesis (i.e., systolic bulging) due to acute ischemia was produced by LAD ligation and a reversible decrease in the

myocardium's contractility was also achieved by adding 4 mM BDM into modified K-H perfusion solution. Initial results in this study have demonstrated two possibilities for potential clinical application of this 2-D cardiac elasticity imaging technique.

First, the results from a single probe demonstrate the feasibility of sensitively detecting abnormal wall deformation using directional changes of the principal axes - the results from two probes further validate this feasibility. Under two perfusion conditions (only modified K-H solution and K-H solution including 4 mM BDM) as shown in Figs. 3.7, 3.8 and 3.10, muscle fibers during systole actively shorten primarily along the heart's circumferential direction producing heart wall thickening primarily along the heart's radial direction before LAD ligation. After ligation, fibers are passively stretched primarily along the heart's circumferential direction by surrounding muscles, leading to the heart wall's thinning approximately along the heart's radial direction in the area perfused by the LAD. The region detected by this directional change matches well with the area at risk identified by Evans Blue staining. The continuous transition of principal axes at the boundary of the region is also found in Figs. 3.7, 3.8 and 3.10. This is consistent with previously reported findings describing the tethering effects of surrounding normal myocardium on segments which have lost active contraction [9].

We also repeated the experiment in a second rabbit heart perfused with K-H solution to demonstrate the coordinate-independence of strains based on principal stretches and corresponding principal axes. Compared to the first heart

(Fig. 3.11), the region with abnormal contractility was rotated about 45^{o} clockwise as shown in the dot product images of principal axes before and after LAD ligation for different probe combinations (Fig.3.12 (a), (b) and (c)). As expected, the results from single probes (Fig. 3.12 (a) and (b)) show more variation than those using two probes (Fig. 3.12 (c)). The detected abnormal region also matched well with the corresponding Evans Blue staining shown in Fig. 3.12 (d). Similar coordinate-independence was also proposed using principal strains by Zervantonakis [10]. However, principal strains will overestimate or underestimate the deformation as shown in appendix A.

Second, the results from a single probe also demonstrated the feasibility of quantifying myocardial contractility using strains, or strain magnitude, based on the principal stretches along principal axes. In this experiment, 4 mM BDM was used to reversibly reduce overall myocardial contractility, which decreases the heart's global function as measured by LV pressure. As expected for the 4 mM BDM case, strains based on the principal stretches along the principal axes decrease along with the decrease of the myocardium's contractility, as shown in table 1. Therefore, the strains, or strain magnitude, along the principal axes can be used as an indicator of myocardial contractility. It may be possible to sensitively detect segmental changes in contractility (such as segmental akinesis) from the locally decreased magnitude of strains along the principal axes.

The above two conclusions derived using asymmetric displacement accuracy (i.e., normal single probe measurements with good axial and poor lateral estimates) were further validated using symmetric displacement accuracy

(i.e., dual probe measurements using only accurate axial tracking estimates from each). The location of the abnormality and general trends in contractility detected with a single probe are similar to those obtained with two probes. However, the size and shape of the abnormal region are different for the different probe combinations. This difference is due primarily to the large variance in lateral displacement estimates and their position in the deformation tensor $\mathbf{F}$ as shown in Eq. (A-1). This leads to dependency of the accuracy of 2-D cardiac strain imaging using a single probe on the probe's orientation, even though the principal axes and their corresponding strains are theoretically only related to the deformation status at that point and independent of coordinates.

Initial results using a single probe in this study suggest that this method may be clinically useful for diagnosing cardiac diseases related to abnormal wall deformation by finding the abnormal principal axis directions of myocardium during systole. That is, a possible regional dyskinesis can be found by a single probe when the principal axis of positive strain in this area during systole is not primarily along the radial direction of the heart wall. This method reduces the angle limitation of Doppler based strain imaging and has potential for detecting the transmurality of myocardial ischemia or infarction with higher accuracy and spatial resolution than B-mode image based tracking.

The results obtained with this method using a single probe must be used with special care for clinical interpretation since the accuracy of the region at risk depends on the probe's orientation relative to the heart wall. Analysis of single probe data acquired from multiple views on the suspected region during

examination is also recommended if possible. If the location of the detected suspect region is independent of probe rotation, the confidence in myocardial abnormality will increase. Nonetheless, imaging the same suspect region from different views is subject to limited probe windows among the ribs and requires more operator expertise.

Finally, this technique may also be applicable to stress echocardiography in the future. During stress echocardiography, images obtained at rest and during peak exercise or pharmacologic stress are compared to identify areas at risk for ischemia. The same conclusions made between K-H solution and K-H solution including 4 mM BDM in this study can be applied to strain images acquired during a stress test compared to those acquired at rest. The dot product map of principal axes can be used as another visual presentation to detect the area at risk. However, correct registration of the heart wall between rest and stress images is required to use the dot product image as a potential clinical tool. In addition, a stress test will increase heart rate, producing fewer frames per cardiac cycle at a given frame rate. High frame rate [3, 11] is usually preferred to reduce decorrelation due to out-of-plane motion when correlation-based 2-D tracking is applied. Therefore, interframe interpolation with proper weighting must be developed to properly compare images acquired at different effective frame rates (i.e. frames per cardiac cycle). Moreover, the SNR of clinical data is usually lower than that of controlled animal experiments, which will affect the accuracy of this method when applied clinically.

Table 3.1 Strains based on the principal stretches along principal axes in the highlighted area before ligation.

	Probe1		Probe 2		Probes 1 and 2	
	KH	KH+BDM	KH	KH+BDM	KH	KH+BDM
strain 1 based on the principal stretches (%)	7.7±3.5	4.4±2.0	8.4±4.4	4.9±2.4	6.4±2.6	4.0±1.5
strain 2 based on the principal stretches (%)	10.1±8.6	5.3±4.8	8.6±4.8	4.0±2.2	5.1±2.3	3.6±1.5
strain magnitude based on the principal stretches (%)	13.7±7.6	7.5±4.3	12.7±5.0	6.8±2.3	8.5±2.7	5.5±1.8

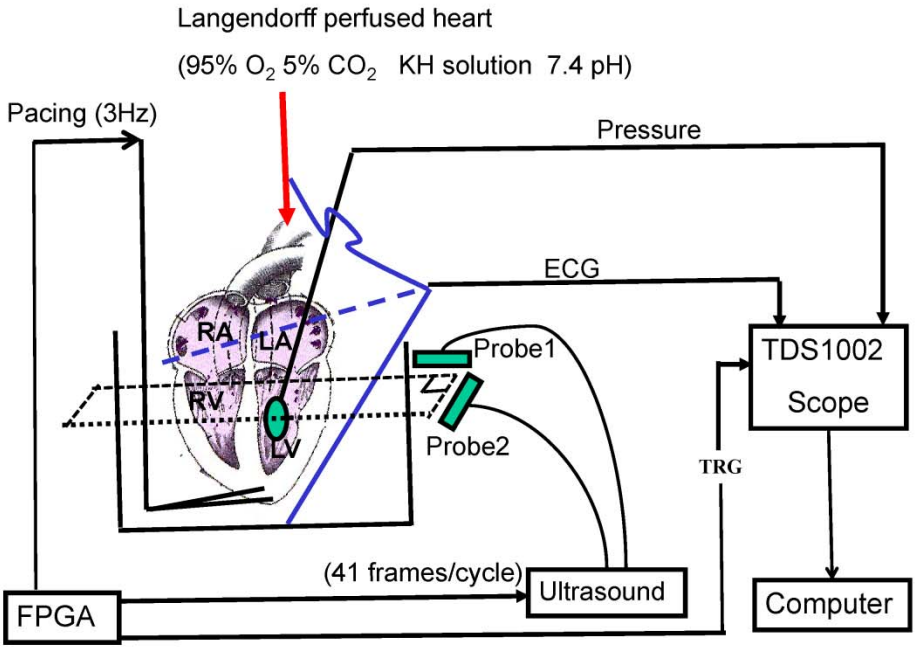

Figure 3.1 Schematic of the experimental setup: The rabbit heart was retroperfused with modified K-H buffer (pH 7.4; 37°C; 95% O2/5% CO2) through the aorta. Two electrodes paced the heart from its apex at 3Hz. The ECG signal was recorded using three electrodes. Two wires were placed at the top and bottom of the bath. The third silver wire was submerged in the perfusion solution right before the aorta. LV pressure was measured through a latex balloon filled with water. Two linear arrays were coplanar and orthogonally positioned outside the tank to acquire RF data. An FPGA chip helped synchronize the pacing signal, LV pressure, ECG signal, and RF data capturing.

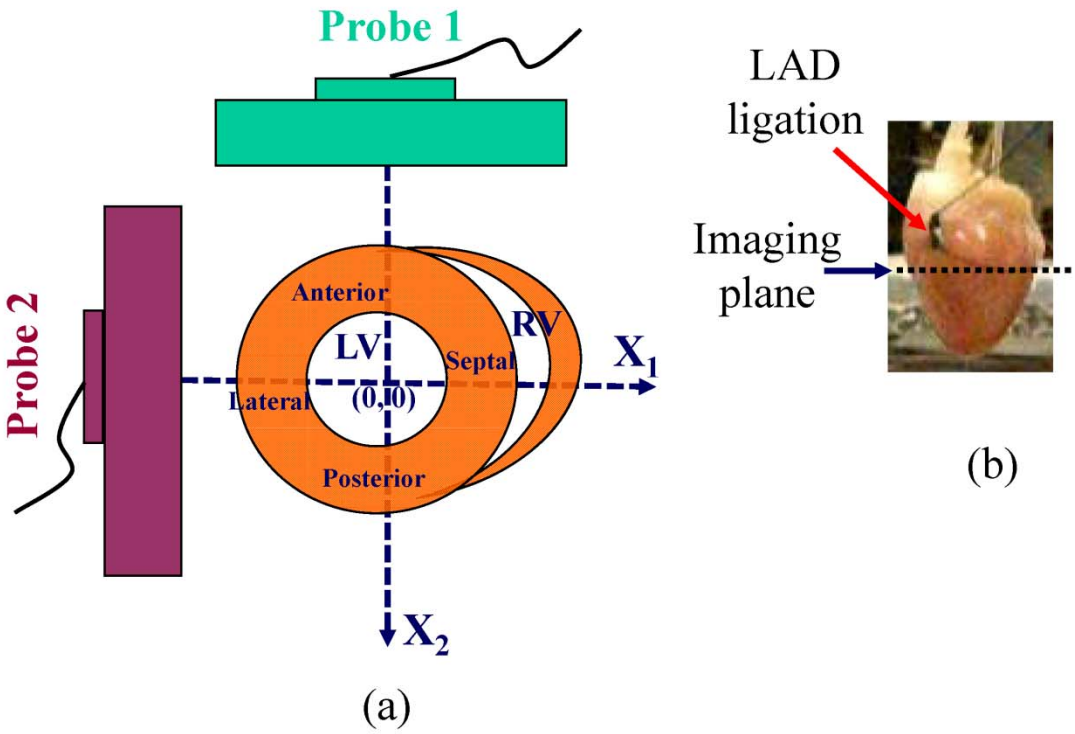

Figure 3.2 Probe orientation in global coordinates for short-axis view of the heart. Two linear probes were coplanar and oriented 90o apart within a plane just below the site of LAD ligation (as shown in (b)). RF data in the short-axis view were acquired from two probes, with higher resolution along the axial direction and lower resolution along the lateral direction for each probe. As shown in (a), the X1-axis is the lateral direction of probe 1 and axial direction of probe 2. The X2-axis is the axial direction of probe 1 and lateral direction of probe 2.

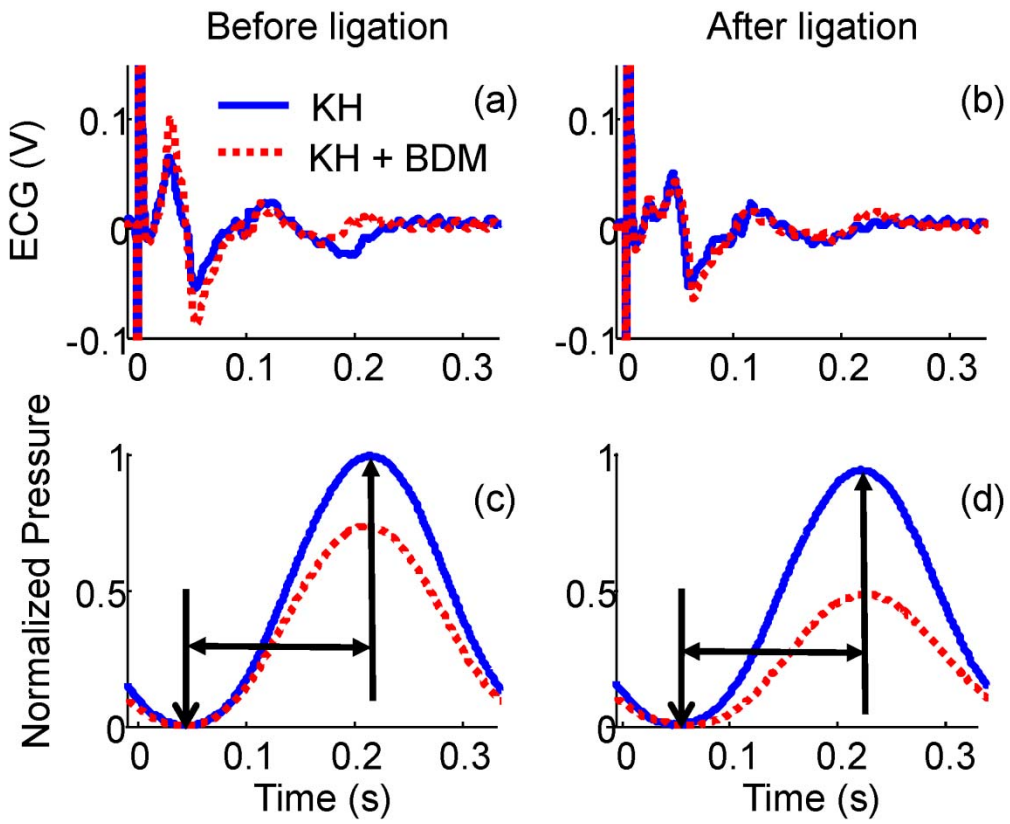

Figure 3.3 (a) ECG measured before LAD ligation; (b) ECG measured after LAD ligation; (c) Normalized LV pressure before LAD ligation; (d) Normalized LV pressure after LAD ligation. The heart was perfused with two different solutions: only modified K-H solution (blue solid line), and modified K-H solution with 4 mM BDM (red dotted line). The big signal at t=0 in (a) and (b) is a triggering artifact. The duration between the two arrows in (c) and (d) is defined as systole in this experiment. The first frame over this period was used as the reference frame for displacement accumulation.

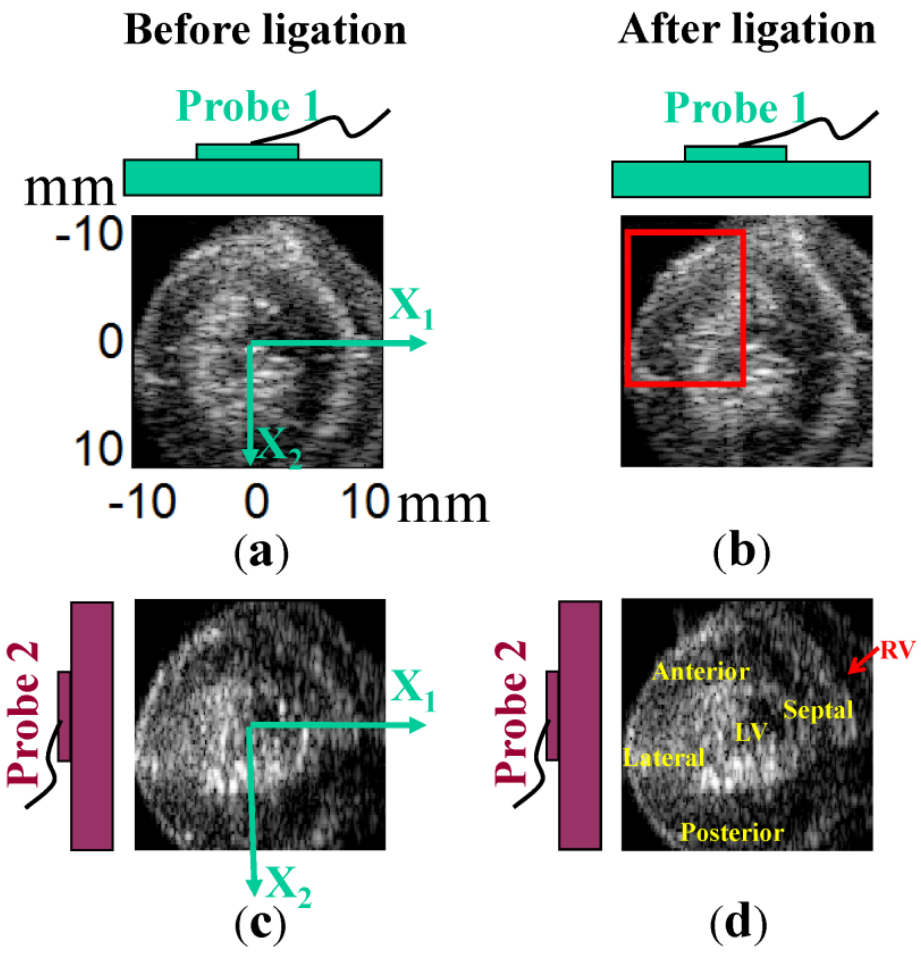

Figure 3.4 B-mode images acquired using the two linear arrays before and after ligation in global coordinates displayed with respect to probe orientation: The first column shows B-mode images before ligation, while the second shows images after ligation. The first and second rows were acquired using probes 1 and 2, respectively. Bulging can be observed from the B-mode movie in the area highlighted by the box in (b).

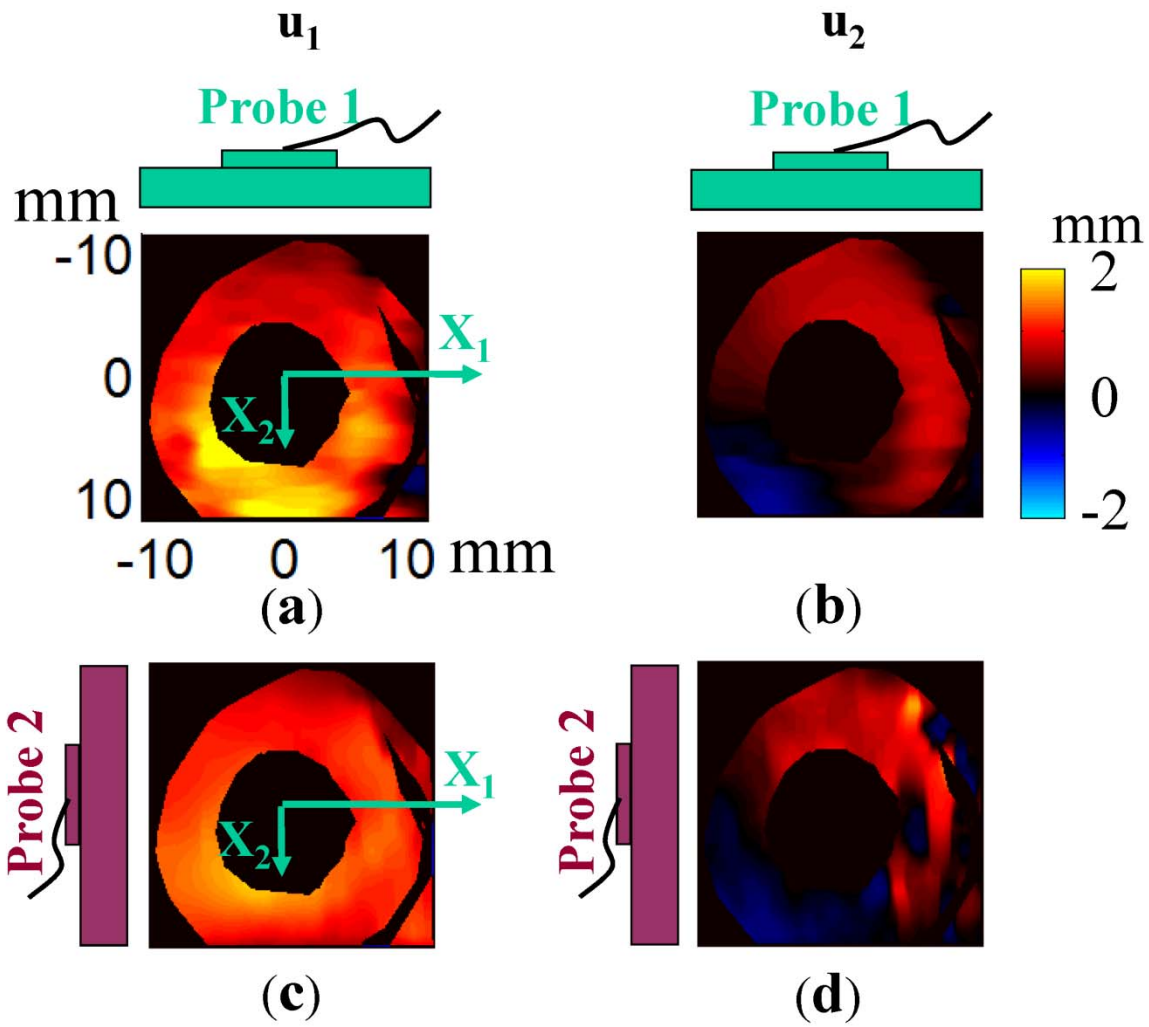

Figure 3.5 2-D displacement (u1, u2) estimated using 2-D speckle tracking and accumulation over systole when the heart was perfused with KH solution before LAD ligation. The first column is displacement u1 estimated from each probe, and the second is displacement u2. The first row presents displacement estimates using RF data acquired using probe 1. The second row presents displacement estimates using RF data acquired using probe 2. As indicated by the probe position and global coordinates, u1 in (a) is the lateral displacement for probe 1; u1 in (c) is the axial displacement for probe 2; u2 in (b) is the axial displacement for probe 1; and u2 in (d) is the lateral displacement for probe 2.

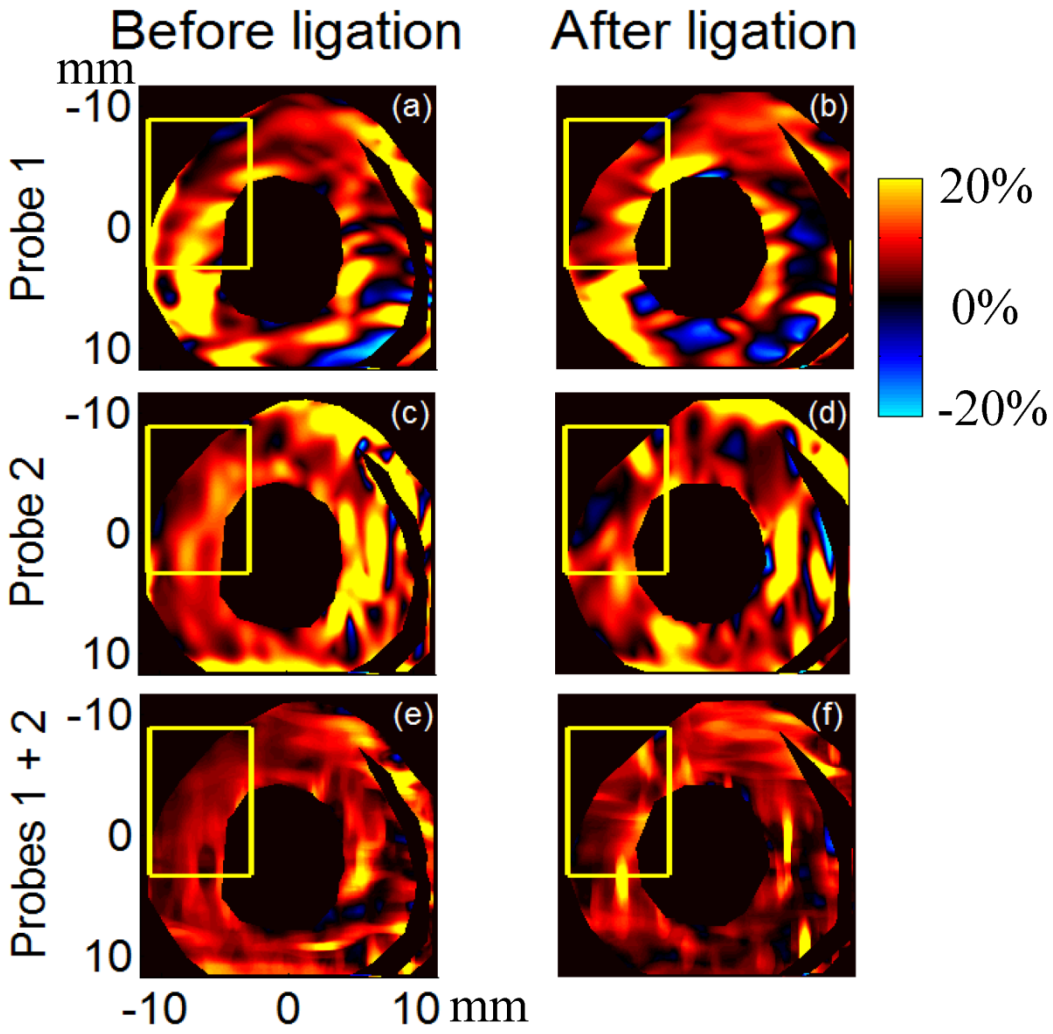

Figure 3.6 Strain based on the principal stretch ($\lambda_1 - 1$) at the end of systole before (left column) and after (right column) ligation for different probe combinations when the heart was perfused with only modified K-H perfusion solution. The first row presents results using only probe 1 data, the second row presents results using only probe 2 data, and the third row presents results combining axial displacement estimates from both probes.

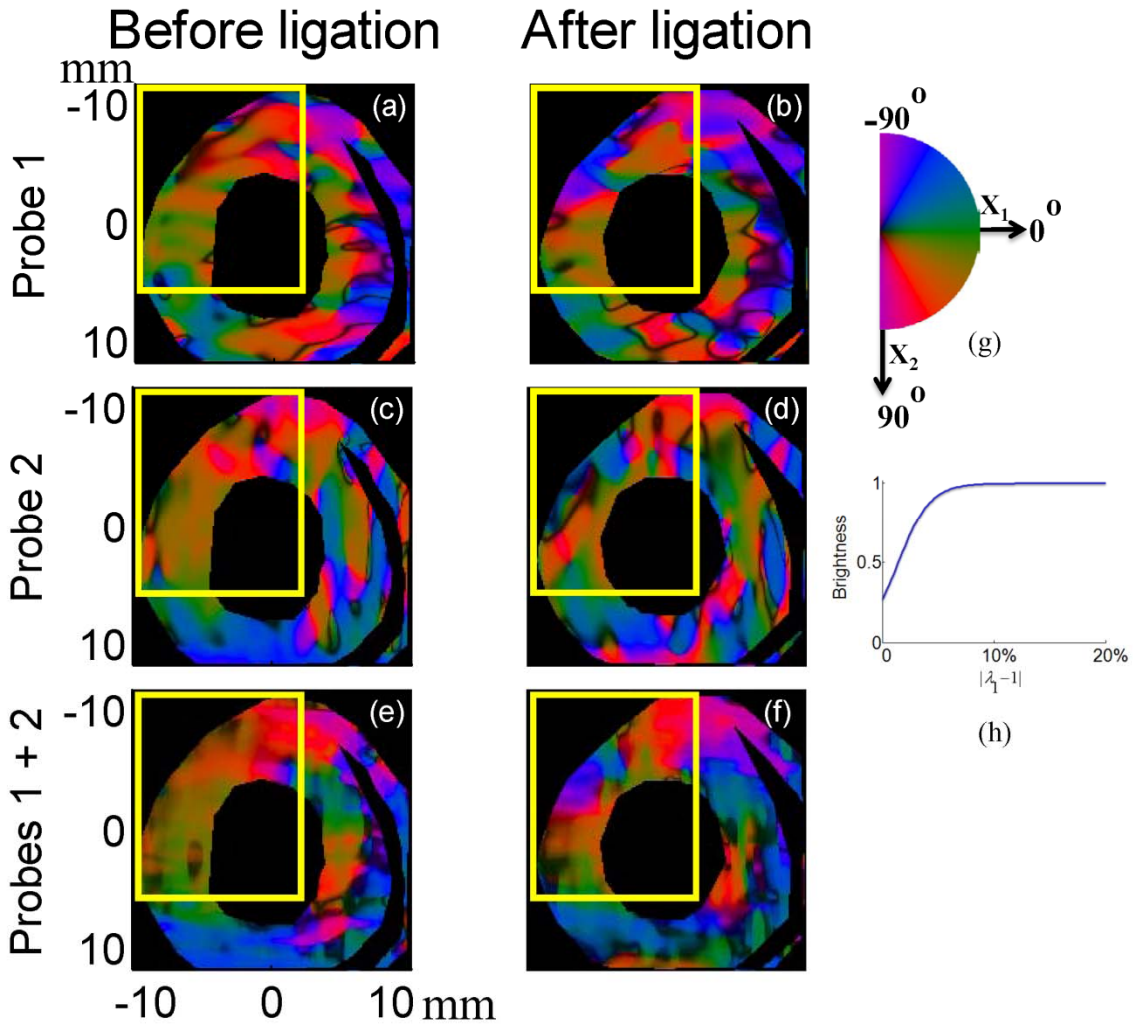

Figure 3.7 The angle of principal axis for strain based on the principal stretch (V_1) at the end of systole before (left column) and after (right column) ligation for different probe combinations when the heart was perfused with K-H perfusion solution. On the left side, the first row presents results using only probe 1 data, the second row presents results using only probe 2 data and the third row presents results combining axial displacement estimates from both probes. The direction of the principal axis changes after ligation, as apparent in the highlighted bulging area. On the right side, (g) presents the cyclic colormap for the angle of principal axis ranging from -90o to 90o; (h) presents the shifted sigmoid function describing the relationship between each color's brightness and the magnitude of the strain.

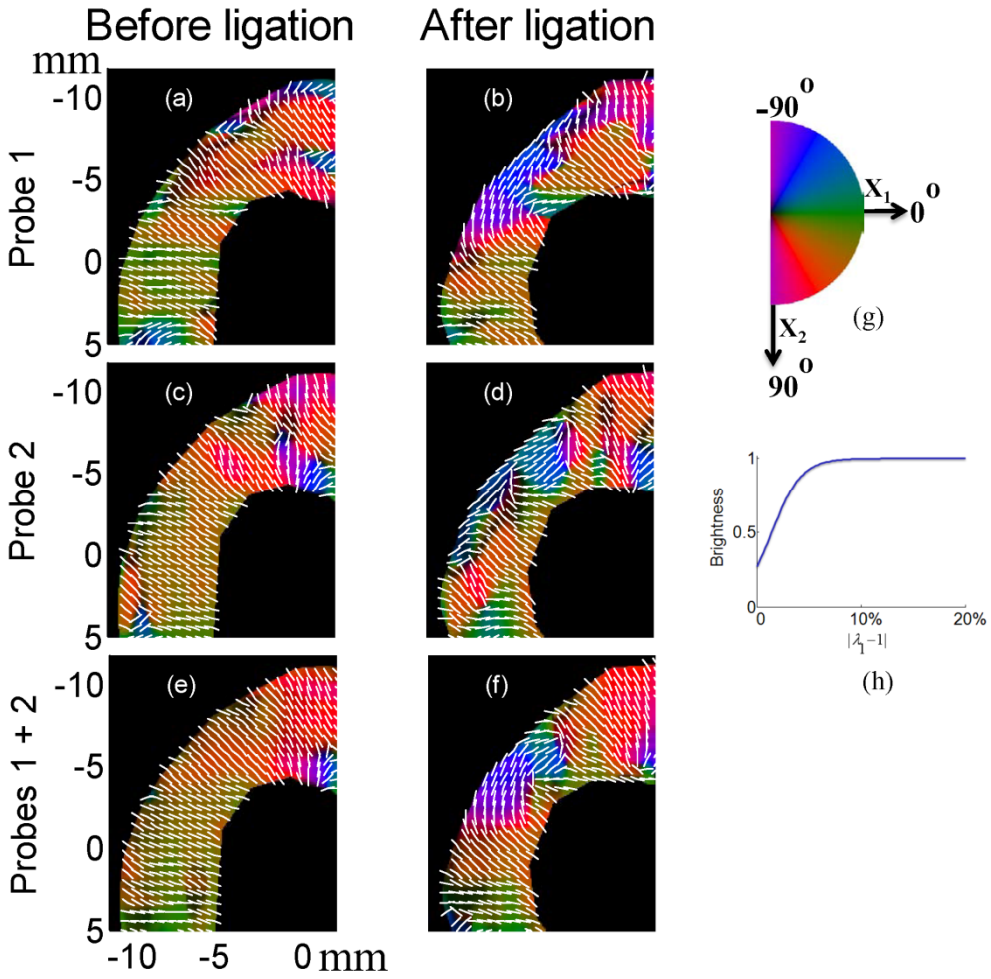

Figure 3.8 Zoom of results in highlighted area using the same layout as Fig. 7 with superimposed vector showing the direction of the principal axis.

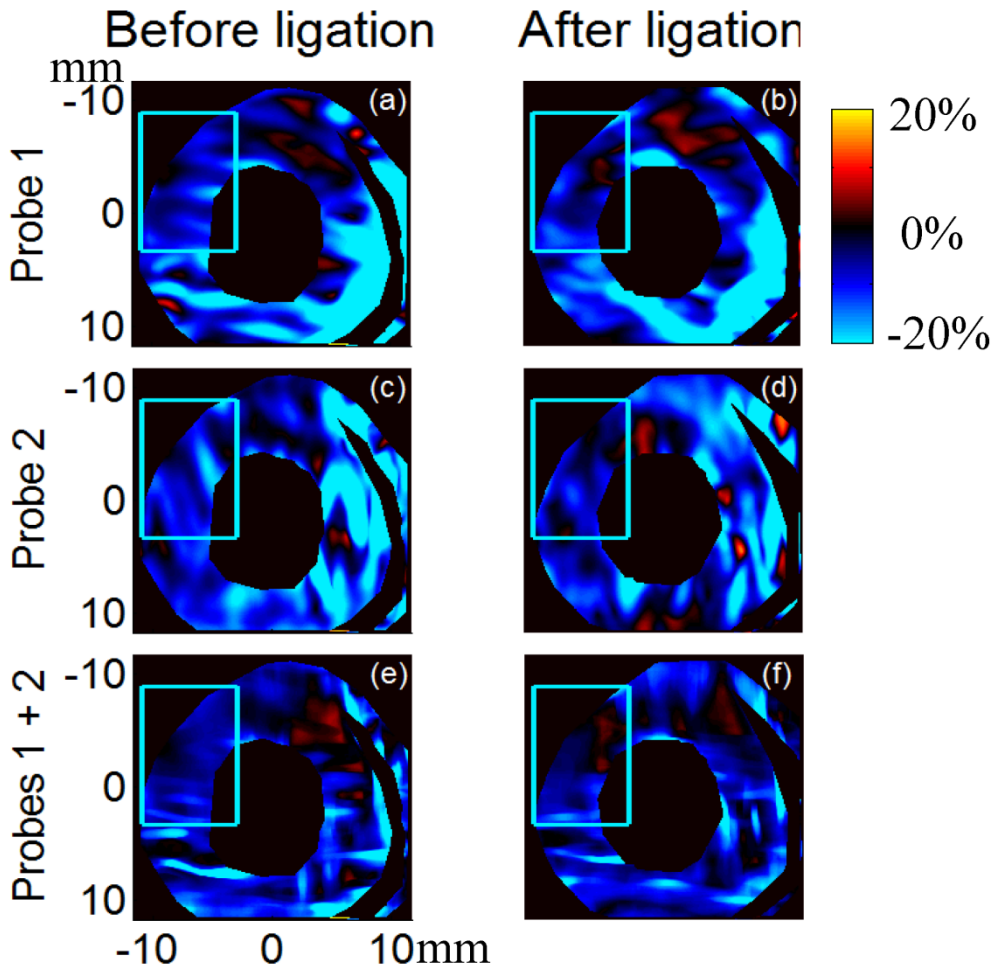

Figure 3.9 Strain based on the principal stretch ($\lambda_2 - 1$) at the end of systole before (left column) and after (right column) ligation for different probe combinations when the heart was perfused with K-H perfusion solution. On the left side, the first row presents results using only probe 1 data, the second row presents results using only probe 2 data, and the third row presents results combining axial displacement estimates from both probes.

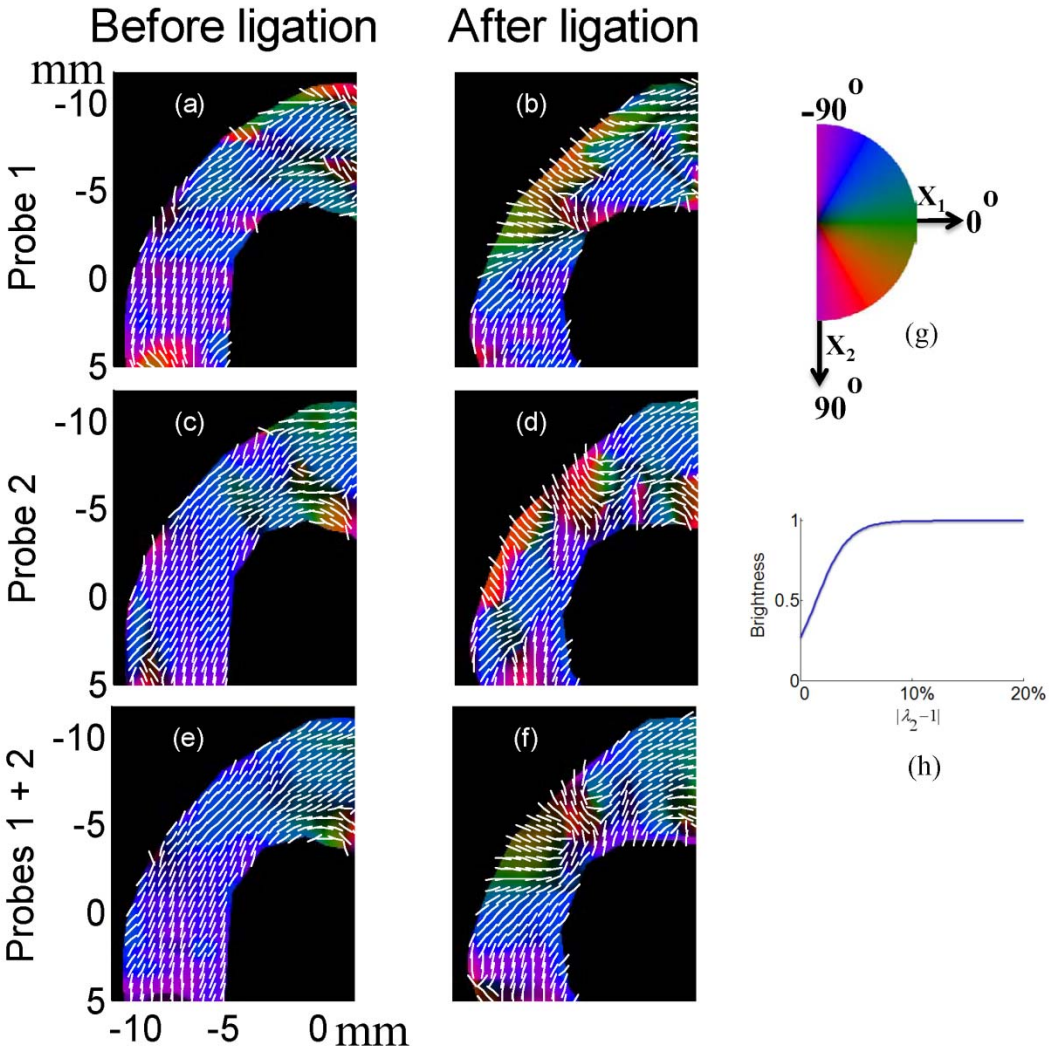

Figure 3.10 Zoom of results in highlighted area for principal axis using the same layout as Fig. 8.

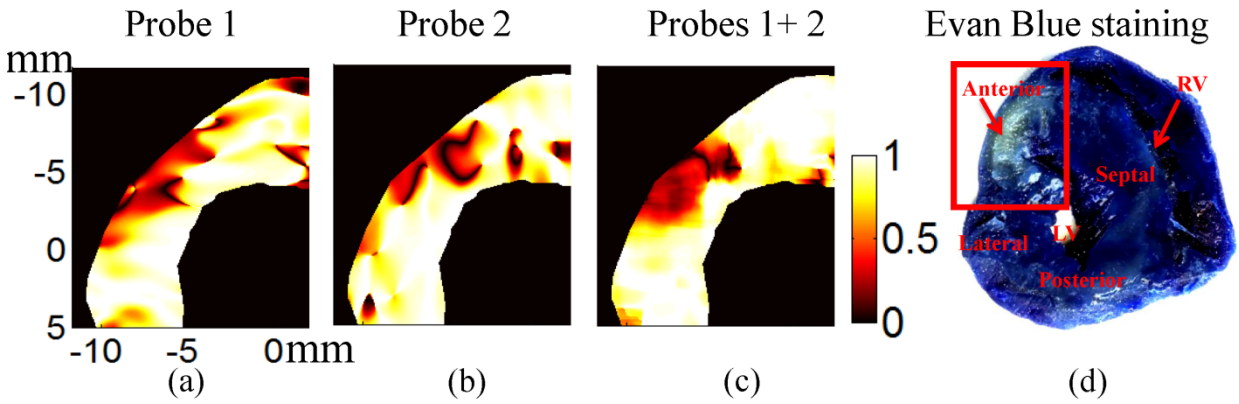

Figure 3.11 The dot product of the first principal axes before and after ligation for heart perfused using only K-H solution: (a) Probe 1; (b) Probe 2; (c) Probes 1+2 (d) Evans Blue staining result after the ultrasound experiment. The highlighted region is the area at risk due to LAD ligation.

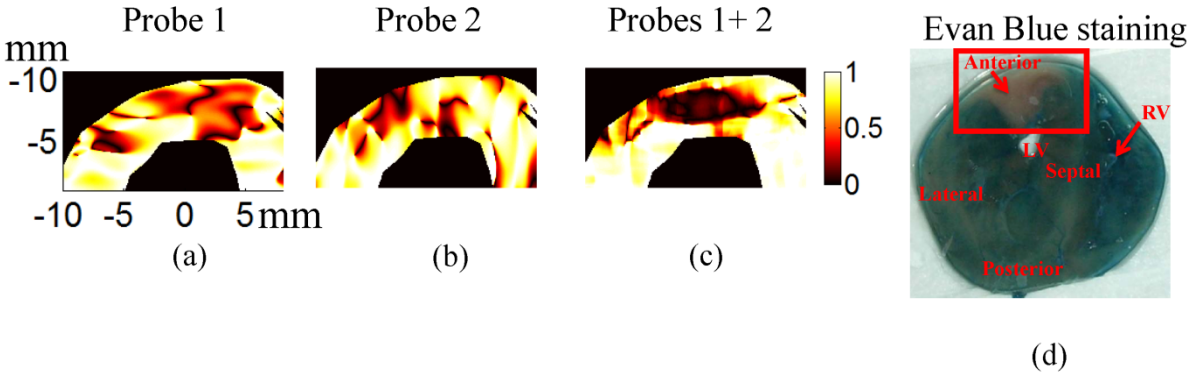

Figure 3.12 The dot product of the first principal axes before and after ligation for the second heart: (a) Probe 1; (b) Probe 2; (c) Probes 1+2 (d) Evans Blue staining result after the ultrasound experiment. The highlighted region is the area at risk due to LAD ligation.

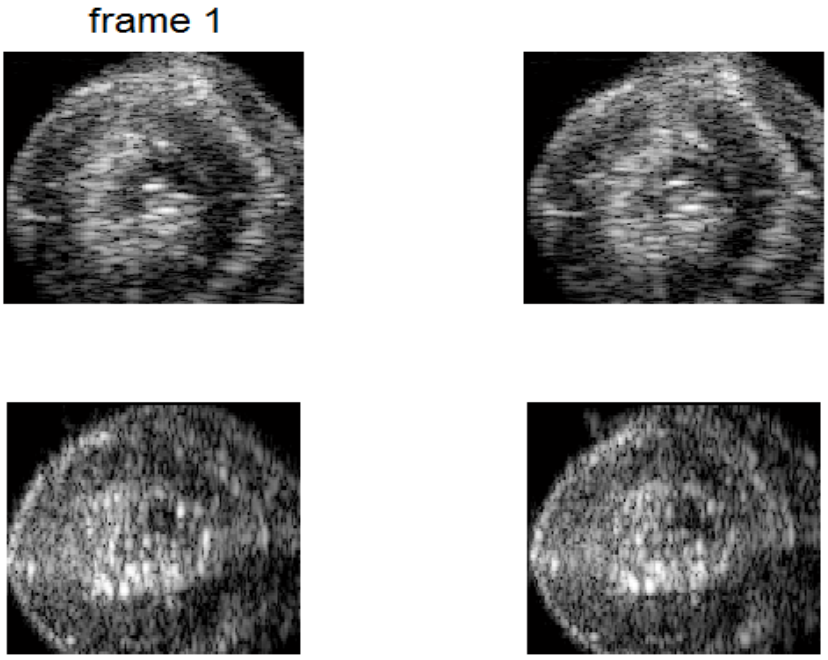

Movie 3.1 B-mode movies acquired using the two linear arrays before and after ligation in global coordinates displayed with respect to probe orientation: The first column shows B-mode movies before ligation, while the second shows movies after ligation. The first and second rows were acquired using probes 1 and 2, respectively. Bulging can be observed from the B-mode movie in the area highlighted by the box in Fig. 3.4(b).

3.5 References

[1] C. Jia, R. Olafsson, K. Kim, T. J. Kolias, J. M. Rubin, W. F. Weitzel, R. S. Witte, S.-W. Huang, M. S. Richards, C. X. Deng, and M. O'Donnell, "Two-dimensional Strain Imaging of Controlled Rabbit Hearts," *Ultrasound in Medicine and Biology*, vol. 35, no. 9, pp. 1488-1501, 2009.

[2] E. J. Tanhehco, K. Yasojima, P. L. Mcgeer, R. A. Washington, and B. R. Luccesi, "Free radicals upregulate complement expression in rabbit isolated heart," *American Journal of Physiology-heart and Circulatory Physiology*, vol. 279, pp. h195-h201, 2000.

[3] J. Luo and E. E. Kobifagou, "High-frame rate, full-view myocardial elastography with automated contour tracking in murine left ventricles in vivo ," *IEEE Trans. Ultrason., Ferroelect., Freq. Contr.,* vol. 55, no. 1, pp. 240-248, 2008.

[4] E. A. Booth, N. R. Obeid, B. R. Lucchesi, "Activation of estrogen receptor-alpha protects, the in vivo rabbit heart from ischemia-reperfusion injury," *American Journal of Physiology-heart and Circulatory Physiology*, vol. 289, no. 5, pp. H2039-H2047, 2005.

[5] S. Kettlewell, ETTLEWELL, ET AL., " The electrophysiological and mechanical effects of 2,3-butane-dione monoxime and cytochalasin-D in the Langendorff perfused rabbit heart," *Experimential Physiology*, vol. 89, pp. 163-172, 2004.

[6] M. A. Lubinski, S. Y. Emelianov, and M. O'Donnell, "Speckle tracking methods for ultrasonic elasticity imaging using short time correlation," *IEEE Trans. Ultrason., Ferroelect., Freq. Contr.,* vol. 46, pp. 82-96, Jan. 1999.

[7] M. A. Lubinski, S. Y. Emelianov, K. R. Raghavan, A. E. Yagle, A. R. Skovoroda, and M. O'Donnell, "Lateral displacement estimation using tissue incompressibility," IEEE Transactions on Ultrasonics, Ferroelectrics, and Frequency Control, vol. 43, pp. 234-46, 1996.

[8] F. J. Villarreal, W. Y. W. Lew, L. K. Waldman, and J. W. Covell, "Transmural myocardial deformation in the ischemic canine left ventricle," *Circ. Res*. vol. 68, pp. 368-81, 1991.

[9] B. Bijnens, P. Claus, F. Weidemann, J. Strotmann, and G. R. Sutherland, "Investigating cardiac function using motion and deformation analysis in the setting of coronary artery disease," *Circulation*, vol. 116, pp. 2453-2464, 2007.

[10] I. K. Zervantonakis, S. D. Fung-Kee-Fung, W. –N. Lee, and E. E. Konofagou, "A novel, view-independent method for strain mapping in myocardial elastography: eliminating angle and centroid dependence," *Physics in Medicine and Biology,* vol. 52, pp. 4063-4080, 2007.

[11] J. D'hooge, A. Heimdal, F. Jamal, T. Kukulski, B. Bijnens, F. Rademakers, L. Hatle, P. Suetens, and G.R. Sutherland, "Regional strain and strain rate measurements by cardiac ultrasound: principles, implementation and

limitations," *European Journal of Echocardiography,* vol. 1,pp. 154-170, 2000.

Chapter 4 4-D Elasticity Imaging of PVA LV Phantom Integrated with Pulsatile Circulation System Using 2-D Phased Array

4.1 Introduction

As described in chapter 1, a challenging issue with cardiac elasticity imaging is that heart motion is 3-D and complex. Currently available 1-D or 2-D elasticity imaging techniques are limited by significant out-of-imaging plane motion. However, the frame rate of cardiac data acquisition using current 2-D probes is not high enough for evaluating 3-D tracking algorithms. A well-controlled experimental setup is needed to validate speckle tracking algorithms for displacement and strain estimation.

A LV phantom [1, 2 and 3] was constructed using Polyvinyl alcohol (PVA) cryogel and integrated with a pulsatile pump in combination with a pressure meter. A commercial 2-D phased array (Sonos 7500, Philips) was used to acquire 3-D RF data on the phantom with an increased effective frame rate by reducing the stroke volume and the beats per minute of the pulsatile circulation system. 2-D and 3-D speckle tracking were tested on this 3-D data set. LV contraction and out-of-plane motion were also simulated and tracked using a computer model of cardiac imaging. These tests represent a first step for cross-validation of multi-dimensional speckle tracking techniques.

4.2 Materials and Methods

4.2.1 PVA Phantom

The PVA phantom has similar acoustic and mechanical properties as tissue. Its elastic modulus can also be controlled by changing either the freeze-thaw cycle number or PVA solution concentration. Both US and PA imagings can use PVA as a tissue-mimicking material.

4.2.1.1 Phantom Design

A LV with uniform thickness about 15mm is designed as shown in Fig. 4.1. The inner surface and outer surface are denoted by two ellipsoid Eqs. (4.1) and (4.2), respectively. The length of the long axes and short axes, and the thickness of this phantom are chosen according to the averaged values of human heart LV geometry at the end of systole [4 and 5], because a LV phantom is passively deformed while live heart actively contracts.

$$\frac{x^2}{18.5^2}+\frac{y^2}{18.5^2}+\frac{z^2}{50^2}=1, \tag{4.1}$$

$$\frac{x^2}{33.5^2}+\frac{y^2}{33.5^2}+\frac{z^2}{65^2}=1, \tag{4.2}$$

Two negative molds were built using three steps to construct the inner and outer surfaces of the LV phantom. The first step was to design two positive molds complementary to the needed negative molds using 3-D CAD software Solidworks as shown in Fig. 4.2. The second step was to print positive molds

from plaster powder using a 3-D printing system (ZPrinter 310, Z Corporation, Burlington, MA) in UM3-D Lab. The third step was to cast negative molds using a liquid molding technique by pouring Hypflex (Hapco inc., Hanover, MA) into a cylinder container holding the positive mold at the container's center and then cutting the dried Hypflex mold into two pieces as shown in Fig. 4.3.

4.2.1.2 Phantom making procedure:

A homogeneous LV phantom was constructed using 8% PVA with two freeze-thaw cycles and two negative Hyperflex molds. First, a PVA solution was heated in an oven at 120^{o}C until fully dissolved and then was cooled down to room temperature. 1% enamel paint (The Testor Corporation, Rockford, IL) was stirred into the solution as acoustic scatterers. Second, 2% agarose (GPG/LE, American Bioanalytical, Natick, MA) was poured into a negative mold to construct an inner positive mold. Third, the agarose inner mold was taken out after the solution solidified and was hanged in the center of the outer negative mold. PVA solution was then poured between the two negative molds. Fourth, the mold with solution was placed in a refrigerator at -20^{o} C for 24 hours and then thawed for 12 hours, completing one freeze-thaw cycle. Two complete cycles were used for the LV PVA phantom. The inner gel inside the PVA phantom was peeled off after the two cycles. A photograph of a finished PVA LV phantom (a), and its B-mode images in short axis view (b) and long axis view (c) are shown in Fig. 4.4.

4.2.2 Pulsatile Circulation System

The pulsatile circulation system includes the PVA LV phantom connected to a pulsatile pump and a pressure meter (Fig. 4.5). The effective frame rate in one heart cycle can be increased by reducing stroke volume (15-100ml), rate per minute (RPM 10-100 beats per minute), and/or adjusting the systole/diastole ratio (35%-50%). LV pressure was recorded by the pressure meter in the upper stream of the phantom. A commercial Ultrasound scanner with 2-D phased array (Sonos 7500, Philips, Andover, MA) was used to acquire a 3-D RF volume sequence on the passively deformed LV phantom in real time. Each data volume covered 46 degrees in azimuth, 22.5 degrees in zenith, and 13cm in depth.

In this experiment, the pulsatile pump was set for a stroke volume of 15ml and a systole/diastole ratio around 50:50. Ninety-two volumes were acquired in one cycle over 4.5 seconds.

4.2.3 3-D LV Simulation

The LV [6 and 7] is simply modeled as a thick-wall ellipsoid built on a prolate spheroid coordinate system with a series of incompressible confocal ellipsoid wall layers (Fig. 4.6). By manipulating semi-major axis *b* and semi-minor axis *a* through a heart cycle, this LV modal is simulated to mimic the heart contraction with out-plane translation along the z-axis (Appendix B). The probe position and directions are shown in Fig. 4.7.

A phased-array imaging system with a 3 MHz operating frequency was used in this simulation. To closely match commercially available cardiac imaging

systems, a 3-D point spread function (PSF) was simulated. The axial PSF is determined assuming a 50% fractional bandwidth and a Gaussian pulse envelope. The azimuthal and zenithal components are created such that the minimum in-plane f/number is 2. The span of both azimuthal and zenithal PSF is depth-dependent once the aperture is fully open.

4.2.4 2-D and 3-D Speckle Tracking

Correlation-based phase-sensitive 2-D [8] and 3-D speckle tracking (ST) algorithms [9] developed in our lab were applied to estimate the cardiac motion between every two consecutive RF frames or volumes in radial, azimuthal, and zenithal domain on PVA LV phantom or simulated LV. 3-D ST is simply extended version of the 2-D algorithm into 3-D case. Both tracking algorithms first calculated the complex cross-correlation coefficient between speckle-sized squared blocks in 2-D ST from the two frames and cubic domains in 3-D ST from the two volumes. The Hanning window with corresponding dimensions filtered the correlation coefficient to reduce tracking error and peak hopping. Displacements in 2-D or 3-D were initially estimated by finding the peak position of the magnitude of the filtered correlation coefficient function using a parabolic fit. The axial displacement was further refined by calculating the position of the phase zero-crossing around the peak correlation coefficient. The displacement estimates in the other directions (azimuthal direction in 2-D; azimuthal and zenithal direction in 3-D) have larger variance than axial ones due to lacking phase information in those directions.

Estimated displacements between two consecutive frames or volumes were then integrated sequentially in frame or volume number to obtain the accumulated displacements relative to a preselected reference frame or volume. In this study, the reference frame or volume was chosen at the beginning of systole (downward arrow in Fig. 4.8) and displacements were accumulated until peak systole (upward arrow in Fig. 4.8).

4.3 Results and Discussion

4.3.1 Pressure Measurements

The differential pressure in the upper stream of the phantom inlet was measured using the pressure meter (Fig. 4.8). Systole and diastole periods are relatively similar since 50:50 systole to diastole ratio was selected for the pulsatile pump. One heart cycle is adjusted to be about 4.5 seconds. By optimizing the period and stroke volume, we were able to increase the effective volume rate and lower the peak deformation between the consecutive volumes. In this way, we can minimize the decorrelation due to the large deformation rate during the systole resulting from low volume rate of commercial ultrasound machine in 3-D data acquisition. In this study, ninety-two volumes were acquired in one heart cycle.

4.3.2 2-D and 3-D Speckle Tracking Results on LV Phantom

Fig.4.9 shows 2-D and 3-D tracking results on the LV phantom at the end of the systole for slice 12. The first column shows 3-D tracking results. The second column shows 2-D tracking results. The third column shows the difference

between 2-D and 3-D tracking results. The first row shows axial displacement. The second row shows azimuthal displacements and the third row shows zenithal displacements. The third row clearly shows that the 3-D speckle tracking algorithm estimates out-of-imaging plane motion. Because the 3-D tracking accounts for out-of-imaging plane motion, azimuthal displacement estimated by 3-D tracking is smoother than that estimated by 2-D tracking. Assuming that 3-D tracking results more accurately represent true displacement, the difference in axial displacement between 2-D and 3-D means that 2-D overestimates or underestimates the displacement when it omits out-of-imaging plane motion. Tracking results on simulated LV in the next section further support this conclusion.

4.3.3 2-D and 3-D Speckle Tracking Results on Simulated Data

Fig. 4.10 shows the theoretical displacement, and 2-D and 3-D speckle tracking results, on the simulated LV displaced with a combination of contraction and out-of-imaging plane motion at the end of systole. The first column shows theoretical displacements at z=0 plane. The second column shows 3-D speckle tracking results and the third column shows 2-D tracking results. The first, second and third rows in Fig. 4.10 show axial, azimuthal and zenithal displacements, respectively. 3-D speckle tracking correctly estimates zenithal displacements compared to theory. Displacement estimations in the other two directions also follow theoretical displacement images.

2-D and 3-D speckle tracking errors were calculated and are presented in Fig. 4.11. For axial displacement estimates, both 3-D and 2-D tracking have some error. 2-D tracking has larger errors than 3-D tracking. This demonstrates that the 3-D reduces 2-D tracking error by estimating out-of-plane motion, which supports the conclusion of the LV phantom experiment.

4.4 Discussion

A PVA phantom connected to a pulsatile pump successfully mimics simple 3-D heart motion. A commercial 2-D phased array was used to acquire a 3-D RF data sequence on the phantom with increased effective frame rate by reducing stroke volume and RPM. 2-D and 3-D speckle tracking algorithms were tested on this data set. 3-D speckle tracking successfully estimated out-of-imaging plane motion and reduced 2-D tracking error on 3-D complex cardiac motion. This conclusion was further supported by LV simulations.

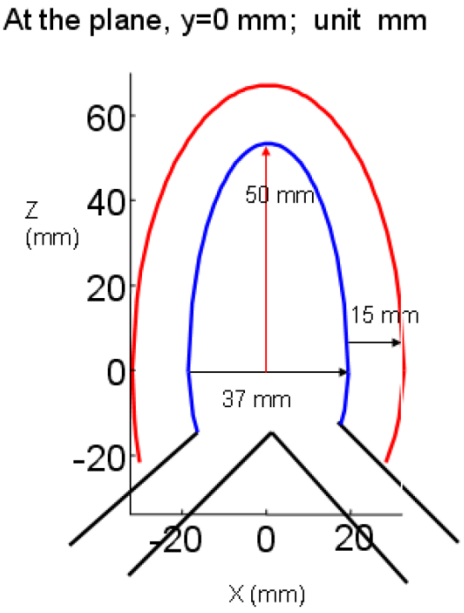

Figure 4.1 The geometry of designed LV phantom.

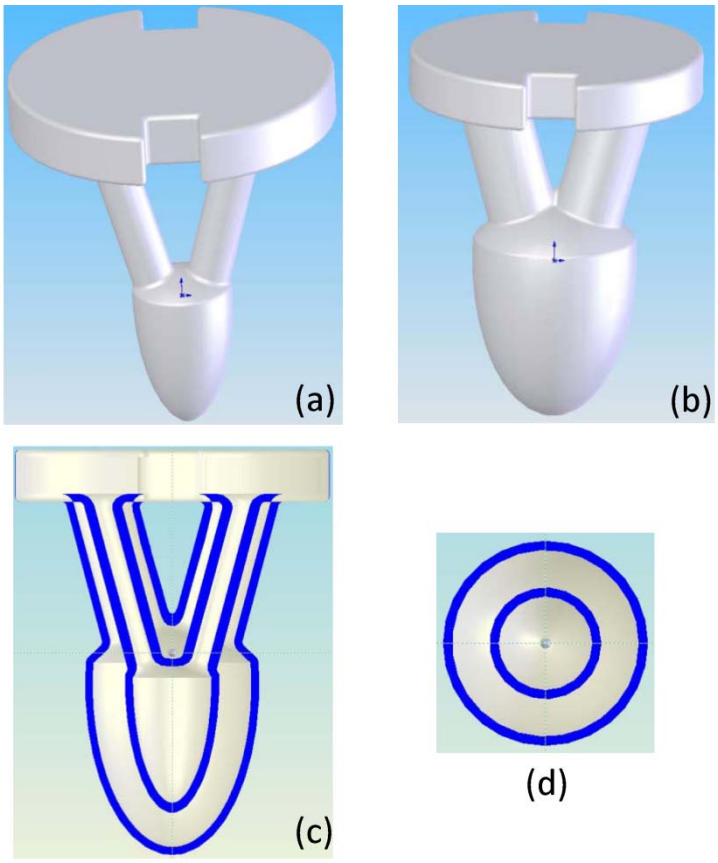

Figure 4.2 Sketches of the two positive molds drawn using Solidworks. (a) a solid positive mold for the inner surface; (b) a solid positive mold for the outer surface; (c) and (d) are cross sections of the assembled two positive molds in long axis view and short axis view, respectively.

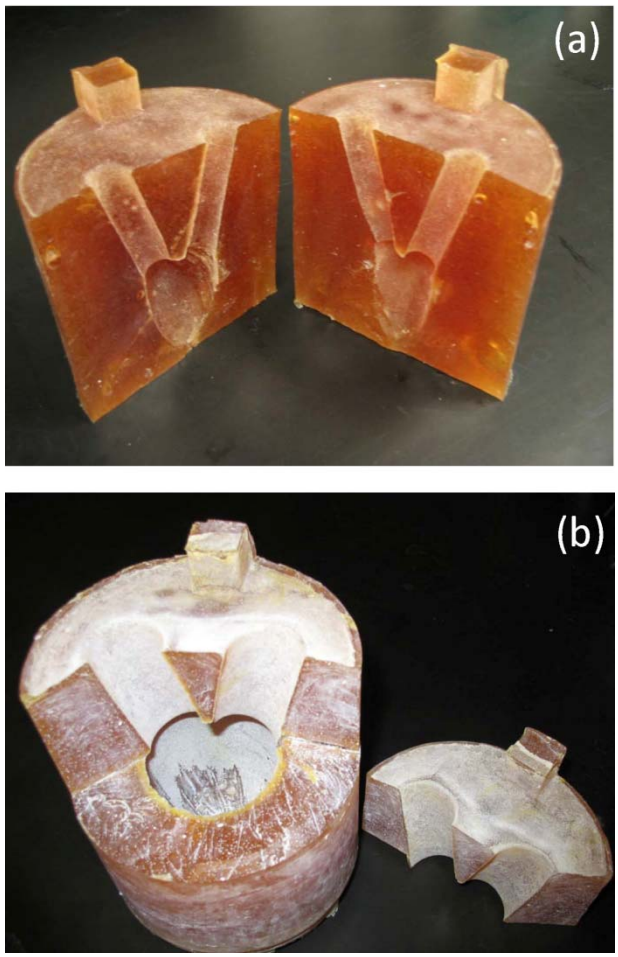

Figure 4.3 Negative molds for the inner (a) and outer (b) surfaces made of Hyperflex.

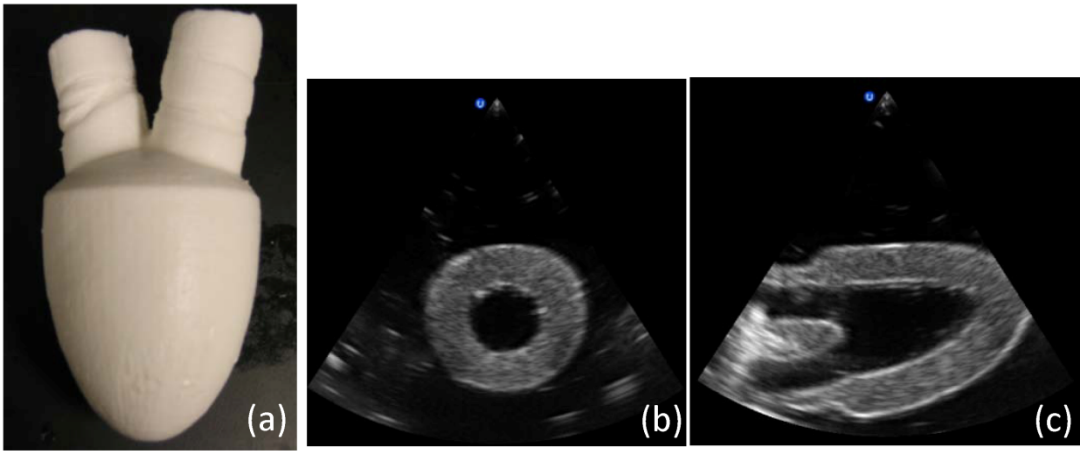

Figure 4.4 PVA LV phantom (a) and it's cross section in short axis view (b) and long axis view (c).

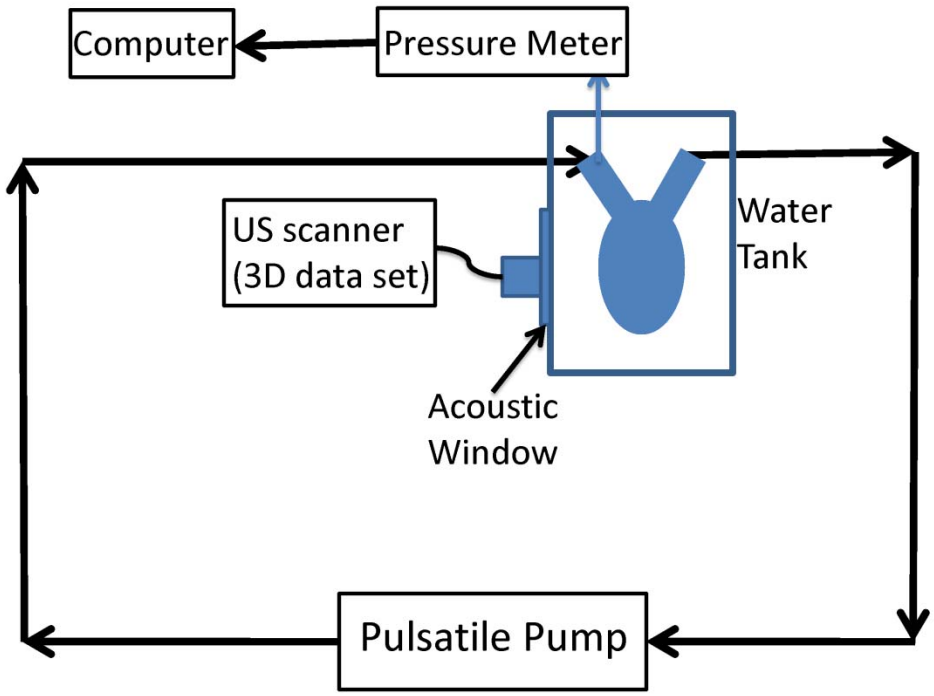

Figure 4.5 Pulsatile circulation system diagram.

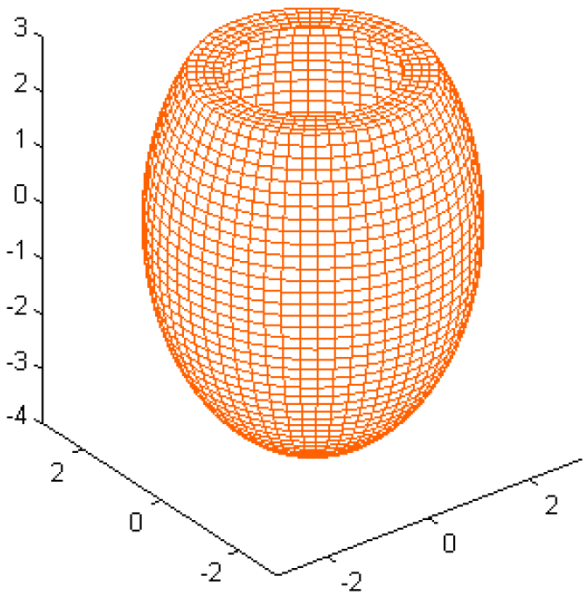

Figure 4.6 A simulated 3-D LV. All spatial dimensions are in cm.

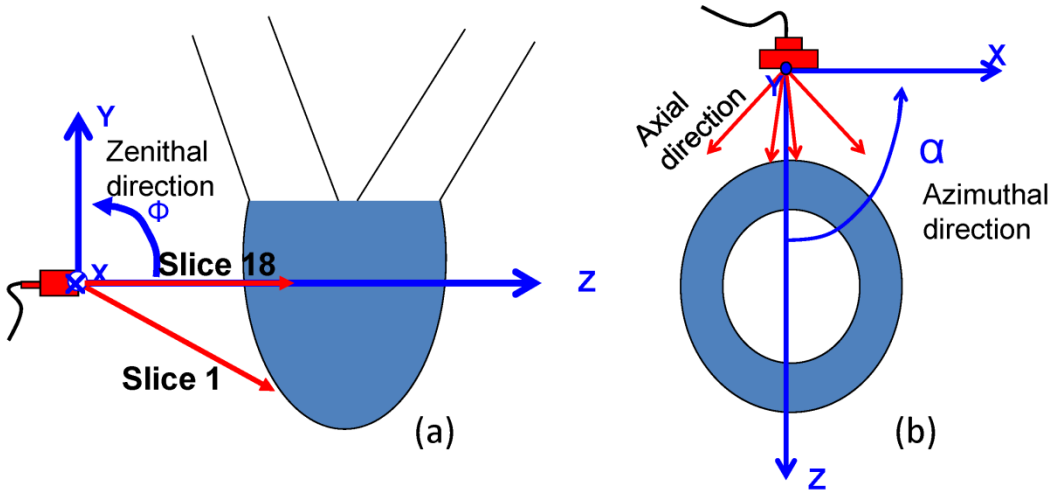

Figure 4.7 The probe position and directions relative to LV in long-axis view (a) and short-axis view (b).

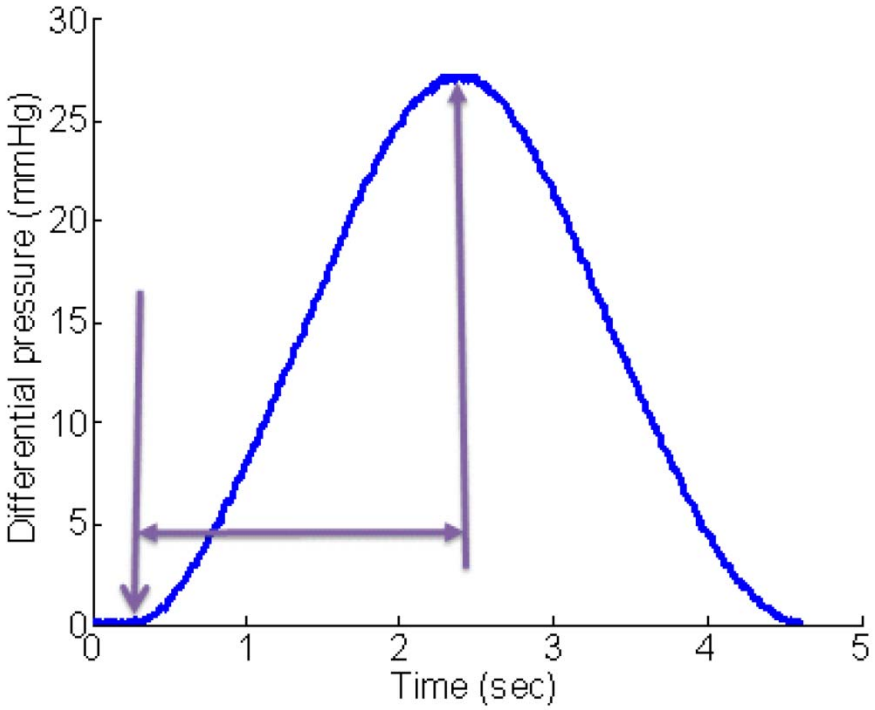

Figure 4.8 Pressure.

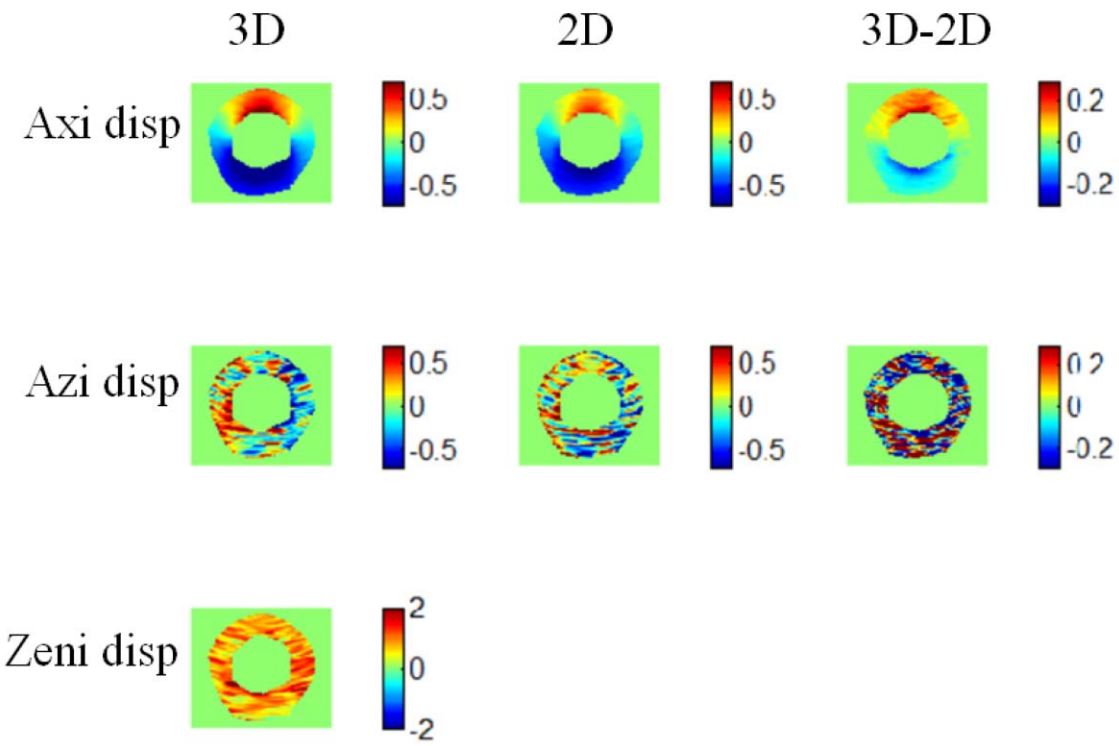

Figure 4.9 3-D (the left column), 2-D (the middle column) displacement estimates and the difference (the right column) between them in mm for the LV phantom.

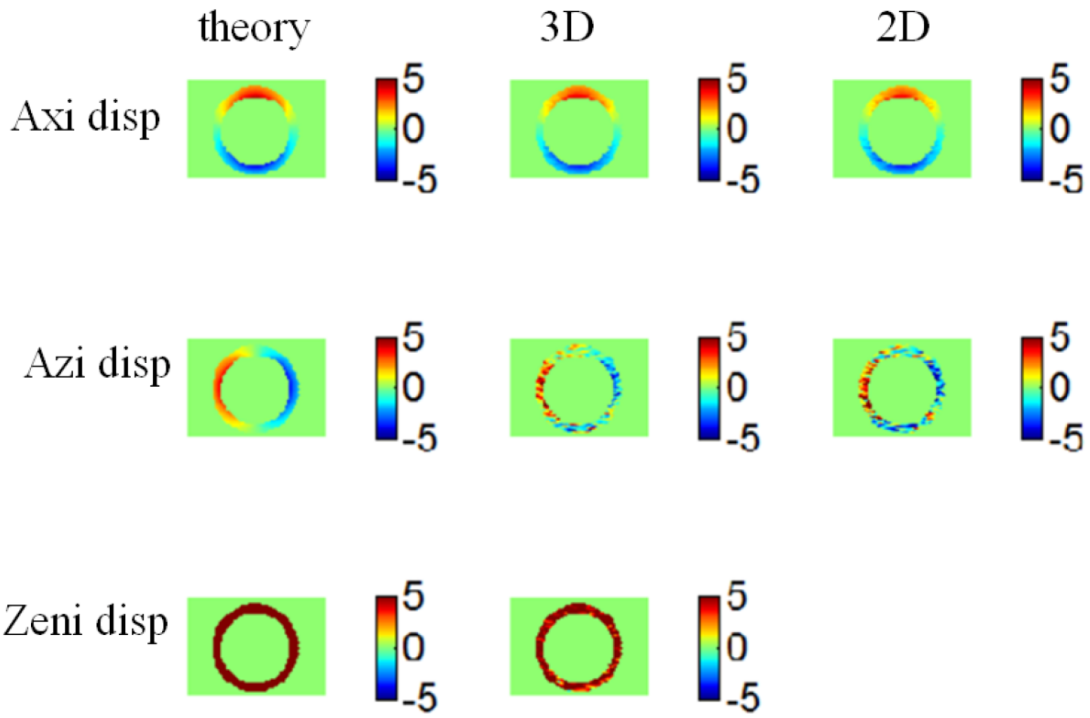

Figure 4.10 Theoretical displacement (the left column), 3-D (the middle column) and 2-D (the right column) displacement estimates in mm on simulated LV.

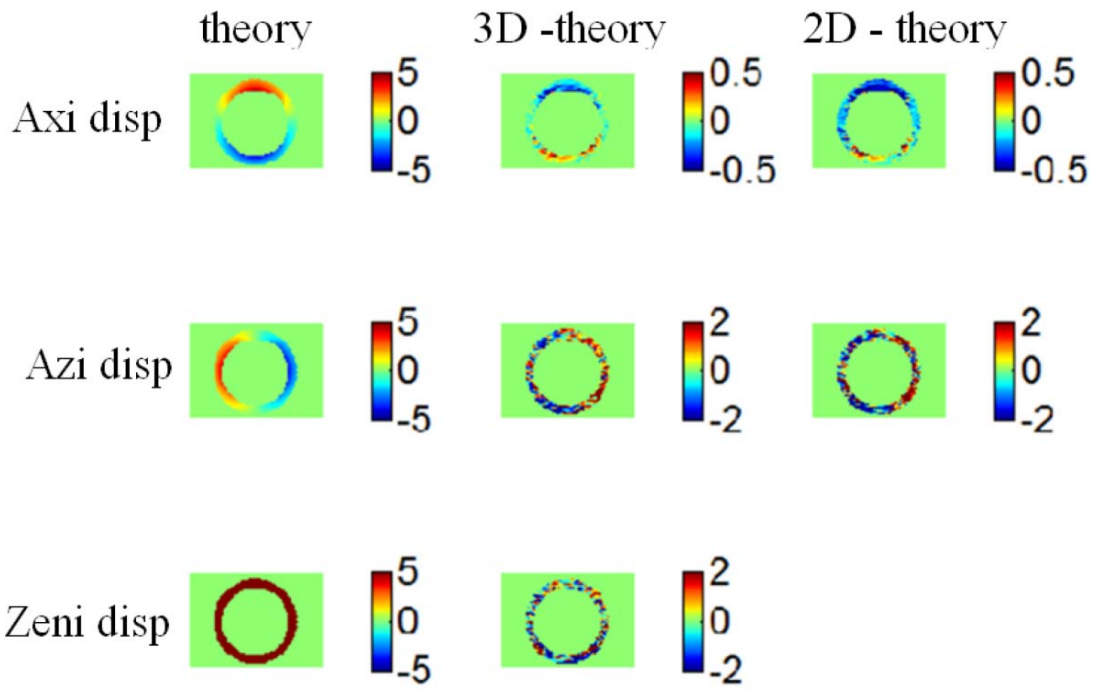

Figure 4.11 The theoretical displacement (the left column), 3-D (the middle column) and 2-D (the right column) displacement estimation error in mm on simulated LV.

4.5 References

[1] C. Jia, K. Kim, T. J. Kolias, W. F. Weitzel, J. M. Rubin, and M. O'Donnell, "Left ventricular phantom with pulsatile circulation for ultrasound strain rate imaging," *Proceedings of the 2006 IEEE Ultrasonics Symposium*, 2006.

[2] S. K.Nadkarni, H. Austin, G. Mills,D. Boughner and A. Fenster, "A pulsating coronary vessel phantom for two- and three-dimensional intravascular ultrasound studies," *Ultrasound in Med & Bio.,*vol.29, no.4, pp 621-628, 2003.

[3] K. J. M. Surry, H.J.B. Austin, A. Fenster and T.M. Peter, "Poly(vinyl alcohol) cryogel phantoms for use in ultrasound and MR Imaging, " *Phys. Med. Biol.* Vol. 49, pp. 5529-5546, 2004.

[4] S.I. Rabben, A. H. Torp, A. Stoylen, S. Slorahl, K. Bjornstad, B. O. Haugen and B. Angelsen, "Semiautomatic contour detection in Ultrasound M-mode Images," *Ultrasound in Med. & Biol*, vol. 26, no.2, pp 287-296, 2000.

[5] A. E. Weyman, "Principles and practice of echocardiography," *Lippincott Williams & Wilkins*; *Second Edition edition*, Jan. 1994.

[6] S.I. Rabben, A. L. Haukanes, F. Irgens. "A kinematic model for simulat ing physiological left ventricular deformation patterns – a tool for evalu ation of myocardial strain imaging," *in Proc IEEE Ultrason Symp,* pp. 134-137 2003.

[7] X. Chen, X. Li, D. Sahn, K. Kim, H. Xie, and M. O'Donnell, "Evalution of 2-D speckle tracking based on strain rate imaging (SRI) using a 3-D heart simulation model," *Proceedings of the 2004 IEEE Ultrasonics Symposium,* pp. 2125-2128, 2004.

[8] M. A. Lubinski, S. Y. Emelianov and M. O'Donnell, "Speckle tracking methods for ultrasonic elasticity imaging using short-time correlation," *IEEE Transactions on Ultrasonics, Ferroelectrics, and Frequency Control,* vol. 46, pp. 82-96, 1999.

[9] X. Chen, H. Xie, R. Erkamp, K. Kim, C. Jia, J.M. Rubin, and M. O'Donnell, "3-D correlation-based speckle tracking," *Ultrasonic Imaging,* vol. 27, pp. 21-36, 2005.

Chapter 5 2-D Speckle Tracking for Contrast Enhancement in Photoacoustic Imaging

5.1 Introduction

As described in chapter 1, PA imaging has demonstrated great promise as a functional and molecular imaging tool [1-3]. However, background PA signals limit the specific contrast of molecular contrast agents. To increase the linear range of molecular contrast agents, the background must be suppressed [4].

In chapter 5, we demonstrate that contrast can be increased by magnetomotive manipulation of magnetic nanoparticles (MNPs). These particles are subjected to a time-varying magnetic field. Researchers have shown that by detecting tissue motion induced by magnetomotive force using ultrasonic or optical imaging, regions with magnetic nanoparticles can be identified [5-6]. Pure optical approaches suffer shallow penetration. Pure ultrasound approaches are also limited because nanoparticles cannot produce a measurable ultrasound signal and therefore motion detection relies on scattered signals from the tissues containing nanoparticles rather than from the nanoparticles themselves. In contrast, combining magnetomotive manipulation with PA imaging of MNPs allows direct manipulation of the PA signal generating object. Like US imaging, PA image, as a coherent imaging modality, is also characterized by the presence of speckle. Speckle tracking can be used to estimate motion due to magnetomotive manipulation of magnetic MNPs in a PA image sequence. PA

contrast can be greatly enhanced by identifying the region due to this motion and suppressing the unwanted, stationary PA signal.

5.2 Methods

5.2.1 MNP-AU Core-Shell Agents and their optical, magnetic properties

MNP-gold coupled NPs, schematically illustrated in Fig. 5.1(a), use monodisperse MNPs with hydrophobic surface ligands (oleic acid) as core. Then the core structure is sequentially deposited by phospholipid-polyethylene glycol terminated with carboxylic acid (PL-PEG-COOH), a layer of positively charged peptide, poly-L-histidine (PLH) to create anchor points for gold shell growth. Finally, a layer of Au3+ ions is immobilized on those anchor points. The multilayer organic molecules coated on the MNP surface (oleic acid, PL-PEG, and PLH) effectively separate the gold ions from the iron oxide core, forming an MNP core and gold shell structure [7]. Transmission electron microscopy (TEM) images of the PL-PEG-COOH / PLH coated MNPs (Fig. 5.1 (b)) and MNP-gold coupled agents (Fig. 5.1 (b)) further confirm the core-shell structure due to the low electron density of the embedded organic molecules.

PLH templated gold deposition can control the gold layer thickness with nanometer precision; enable fine adjustment of the optical properties of the MNP-AU Core-Shell Agents. The extinction spectra of MNP-gold core-shell hybrid particles with different gold shell thickness (Fig. 5.1 (d)) shows high NIR absorption compared to MNPs coated with PL-PEG-COOH and PLH polymer layers, which is desirable for photoacoustic imaging. The susceptibility of the

hybrid NPs (2-3 nm gold shell), measured using a superconducting quantum interference device (SQUID) magnetometry, shows that the hybrid NP responds nearly as well as the bare MNP core itself.

5.2.2 Phantom and Integrated Multimodality Imaging System

A 3-mm thick, 10% PVA disk (Fig. 5.2) was constructed as an imaging phantom. It contained three 2-mm diameter cylindrical inclusions made of 10% PVA mixed with 8% 15-um polymer beads. The first, containing gold nanorods with comparable absorption coefficient as 3 nM MNP-gold hybrid NPs, serves as a magnetic reference, i.e., a localized “background” region to be suppressed in mmPA imaging. The second, containing 3 nM MNP-gold hybrid NPs, serves as an object of interest. And the third, containing 3 nM MNPs, serves as an optical reference. The PVA phantom was positioned in a water tank held by a 2-D mechanical stage, as illustrated in Fig. 5.2.

The integrated multimodality imaging system consists of three parts: laser illumination system, electromagnet system, and US system. An optical parametric oscillator (Surelite OPO Plus, Continuum, Santa Clara, CA) pumped by a frequency-doubled pulsed YAG laser (Surelite I-20, Continuum) with 5-ns pulse width is used as a light source. The laser beam is constrained by an iris and guided to illuminate the imaged object from the top using optical components in free space as shown in Fig. 5.2. The electromagnet system integrates a DC power supply, a waveform generator, a high-power current amplifier, a solenoid, and a core. The waveform generator programs the high-power current amplifier

to drive the solenoid to generate about 0.7-Tesla pulses with a programmable time interval. Either a DC or AC field, or the combination of the two, can be produced with a programmable time course. This extends the range of possible magnetic manipulation of MNPs. A 15-MHz single element transducer (Olympus, Waltham, MA) is used as the US detector to acquire RF signals through an amplifier (AM-1300, Miteq, Hauppauge, NY) and an oscilloscope (LeCroy Corp., Chestnut Ridge, NY). The US transducer is positioned on the top of the imaged object aligned directly opposite to the electromagnet tip, as shown in Fig. 5.3. It is used as only a receiver for PA imaging, and a pulser-receiver for US imaging. The imaged object (such as a polyvinyl alcohol (PVA) phantom here) is positioned in a water tank placed between the US transducer and the electromagnet tip. The water tank is held by a 2-D mechanical stage. By translating the stage, RF data during magnetic field variation can be acquired at different positions and reconstructed into a sequence of 2-D images.

A field programmable gate array (FPGA) is used to synchronize laser illumination, magnetic field generation, and US detection. Multiple recordings are made at each position, interleaving US and PA measurements. The trigger out signal from the pulse laser with 20-Hz repetition rate is set as the main clock of the FPGA. Every 30 seconds, the water tank is moved to a new position with a step size of 0.1 mm. Then the magnetic field is programmed to be on for 5 seconds. The computer acquires either the US signal or PA signal during this 5 second interval and the following 5 second interval through the oscilloscope and amplifier using the single element transducer.

5.2.3 Magnetic-force-induced MNP-gold hybrid NPs' motion

A 2-D image was obtained by translating the water tank using the mechanical stage. At each image position, the magnetic field was turned on for 5 seconds and then off for 5 seconds, as illustrated in Fig. 5.4. The disk containing MNPs and MNP-gold hybrid NPs moved down when the magnetic field was on and up when the magnetic field was off. PA signals during this ten second interval were recorded by the single element transducer. All signals acquired at each position in slow time were used to reconstruct a 2-D PA image sequence as a function of slow time.

5.2.4 Signal Processing Scheme using 2D speckle tracking

An mmPA image can be derived from a series of PA images in a variety of ways. Fig. 5.5 illustrates the current signal processing scheme using 2D speckle tracking. A conventional PA image sequence was acquired in synchrony with a magnetic pulse. The displacement of each pixel in a PA image from its initial position was tracked using a 2D speckle tracking algorithm [8] over the entire 10 second interval, with the magnetic pulse spanning the first 5 seconds. Since the displacement is small, the tracking was performed from the reference frame to the rest frames in the image sequence. The 2D speckle tracking scheme is detailed described in chapter 3 section 3.3.2. For each pixel, we fitted the displacement as linear functions of time over the two 5-second intervals when the field was on/off. A pixel with positive slope in the first half and negative slope in the second half was subsequently fitted to two cascaded exponential functions using nonlinear least squares curve fitting. Using these curves at every pixel, the

maximum positive and negative velocities were used to create a weighting image based on the magnitude of the difference between the peak positive velocity in the first half and the peak negative velocity in the second half. The mmPA image was produced from the product of the original PA image and the weighting image as shown in Fig. 5.5, where the gold nanorod inclusion is almost completely suppressed.

5.3 Results

A cross-sectional PA image on a dB scale of the PVA phantom at 720 nm optical wavelength was shown in the lower panel in Fig. 5.6. with 0 dB corresponding to the maximum signal level across all images. The inclusion with MNP-gold hybrid NPs (middle) is one order of magnitude (i.e., 20 dB) brighter than the one with MNPs (right), while the inclusion with gold nanorods (left) has comparable PA strength to that with MNP-gold hybrid NPs. One typical displacement trace from each inclusion estimated using 2D speckle tracking and its fitted curve were shown in the upper panel. Unlike the MNP-Au core shell particle inclusion (middle) and pure MNP inclusion (right), almost no motion is found in the inclusion (left) containing the gold rod.

The maximum positive (upper panel) while the magnetic field was on and negative velocities (middle panel) while the field is off were shown in Fig. 5.8. The magnitude of the difference between the peak positive velocity and the peak negative velocity was used to create a weighting image (lower panel Fig. 5.8). The mmPA image (lower panel in Fig. 5.9) was produced from the product of the

weighting image (lower panel Fig. 5.8) and original PA image (upper panel in Fig. 5.9), where the gold nanorod inclusion is suppressed by more than 40dB.

5.4 Discussion

Although the principle of suppressing strong PA sources not susceptible to an applied magnetic field (e.g., the gold nanorod inclusion above) in mmPA imaging has been demonstrated, finite background motion in real clinical imaging from physiological sources such as cardiac motion and respiration can interfere with induced motion. Other imaging modalities, such as acoustic radiation force impulse (ARFI) imaging [9] and thermal strain imaging (TSI) [10], have a similar problem of tracking small induced displacements during physiologic motion. Robust signal processing methods have been developed to track induced motion by synchronizing the data acquisition sequence with physiologic motion. Similar methods can be developed for clinical applications of mmPA imaging.

In mmPA imaging, the induced motion depends not only on the magnetic field but also on tissue elastic properties. Therefore, in biomedical applications, it is hard to quantitate the contrast agent concentration based on motion alone. For example, displacements and velocities in the MNP inclusion were slightly greater than those in the MNP-gold hybrid NP inclusion primarily because of differences in the elasticity of the inclusions. However, the induced motion, regardless of scale, is coherent with the applied magnetic field. By detecting motion in response to a time-varying magnetic field, contrast can be greatly improved. The ability to enhance regions with targeted contrast agents makes mmPA imaging

an attractive modality for molecular diagnostics. In addition, because the displacement time course depends on tissue elastic properties (e.g., after the magnetic field is turned off, displaced tissue moves back to its original position subject only to intrinsic elastic properties such as relaxation), mmPA imaging can potentially also be used for elasticity imaging. Fig. 5.9 shows the elastic relaxation time estimated from the displacement curve after the magnetic field was turned off. The higher relaxation time in the pure MNP inclusion (right) indicates that this inclusion is slightly softer than the MNP-Au inclusion (middle). This explained the relative larger maximum displacement found in the pure MNP inclusion than in the MNP-Au inclusion (Fig. 5.6).

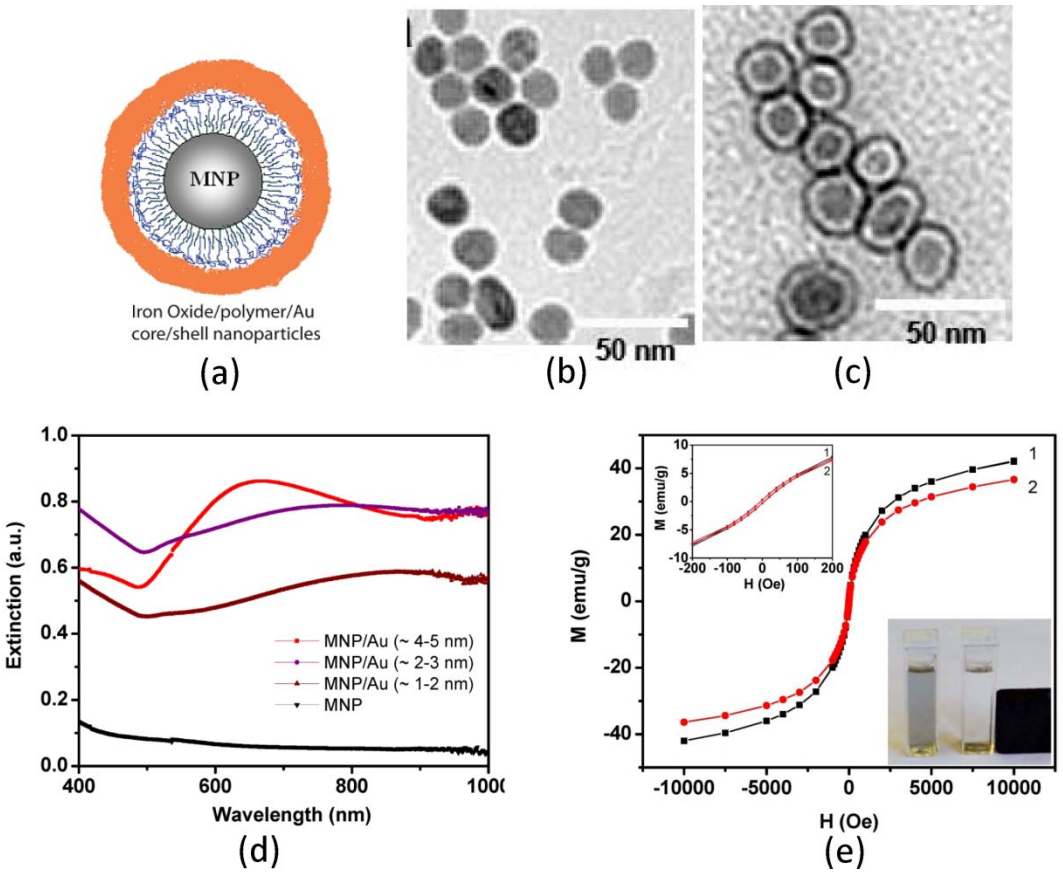

Figure 5.1 Schematic of nanoparticles, and their optical, magnetic properties. (a) Schematic of MNP-gold core-shell NPs; (b) TEM image of the PL-PEG-COOH / PLH coated MNPs and (c) MNP-gold coupled agents, (d) Extinction spectra of MNPs coated with PL-PEG-COOH and PLH (black), and with gold nanoshells of various thickness, 1-2 nm (brown), 2-3 nm (purple), and 4-5 nm (red). (e) Magnetization as a function of magnetic field at room temperature (300 K) for MNP (black) and MNP-gold (2-3 nm shell thickness) (red).

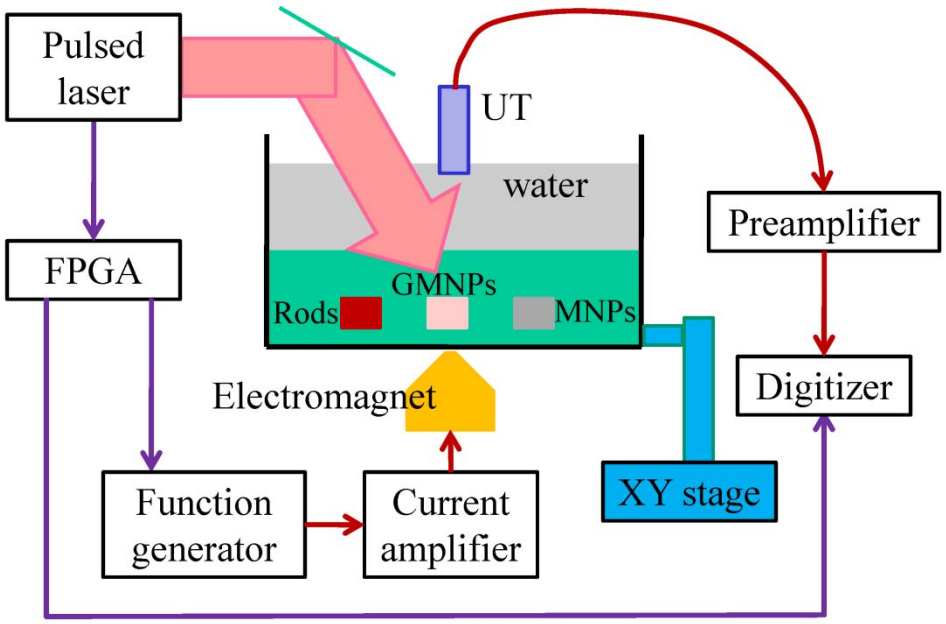

Figure 5.2 Schematic of the system for mmPA imaging.

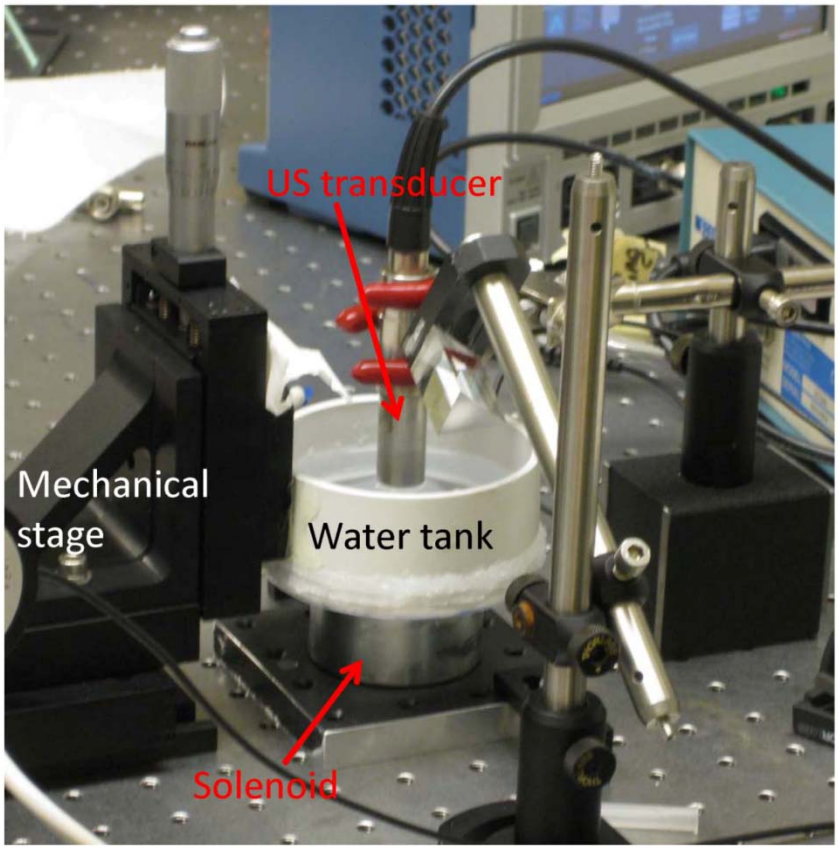

Figure 5.3 Layout of solenoid, US transducer, and water tank.

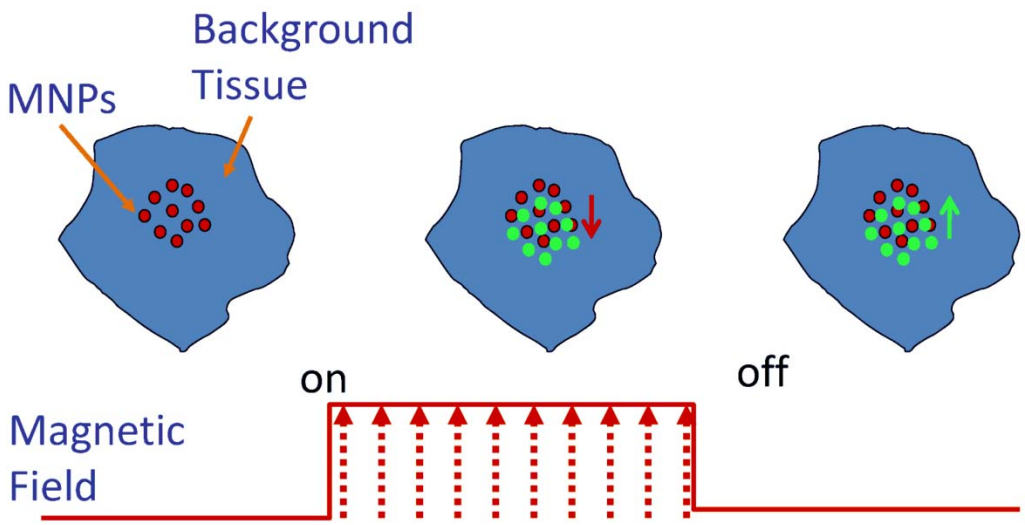

Figure 5.4 Illustration of MNPs' response to magnetic field.

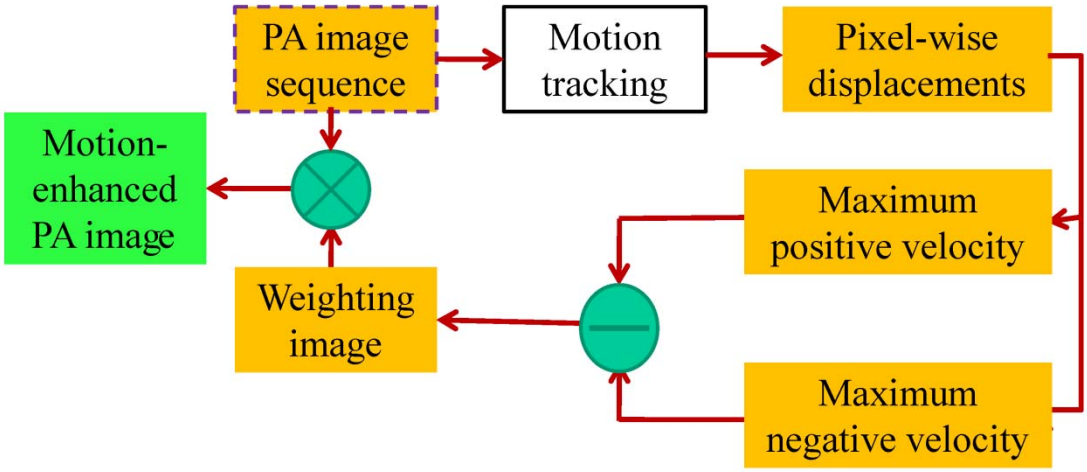

Figure 5.5 Signal processing scheme for motion-enhanced PA image.

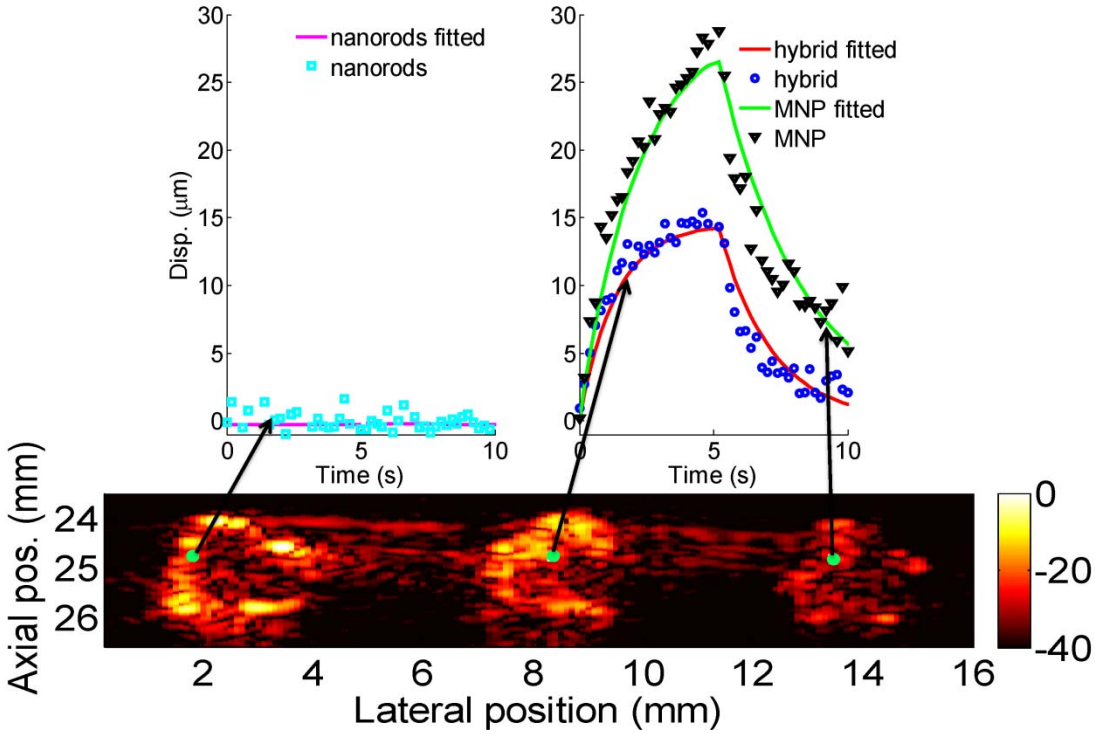

Figure 5.6 Original PA image and typical displacement curves from each inclusion estimated using 2D speckle tracking.

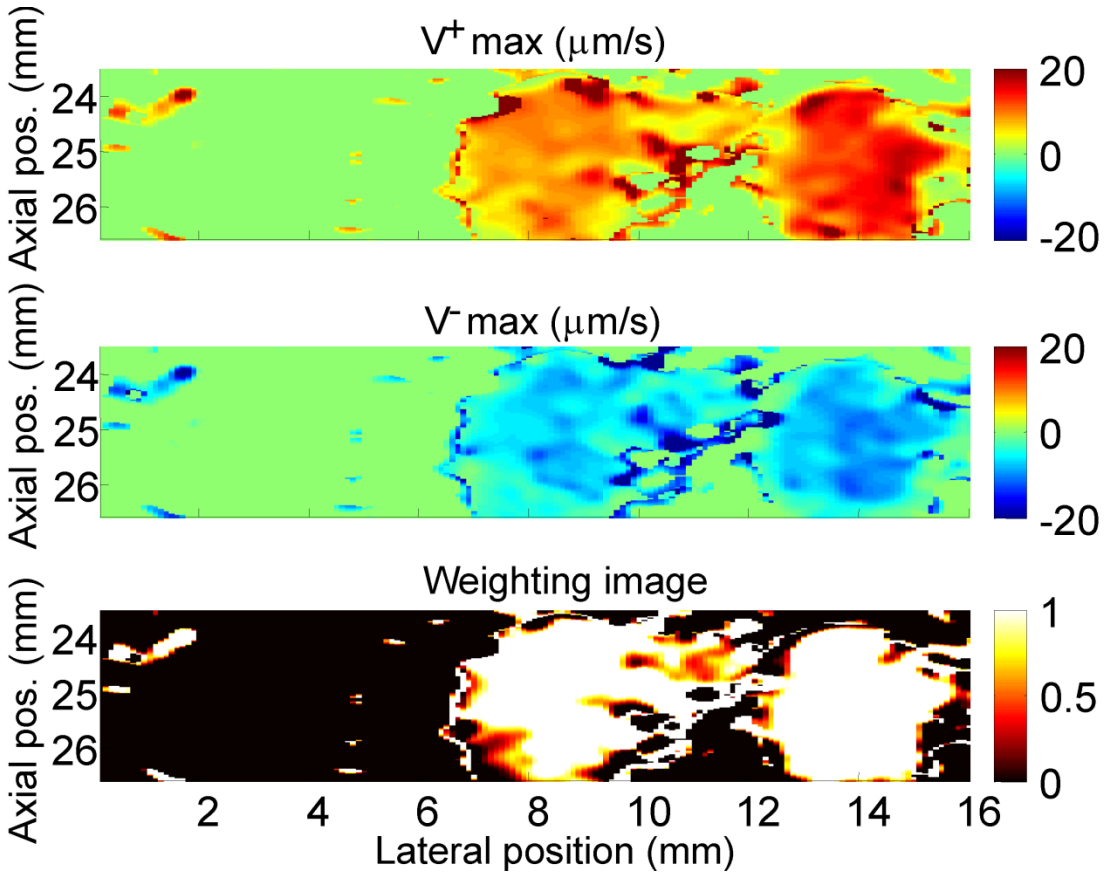

Figure 5.7 Maximum velocity map (upper panel) while magnetic field was turned on, maximum negative map (middle panel) while magnetic field was turned off and the weighting image (lower panel) using the difference of the two velocity maps.

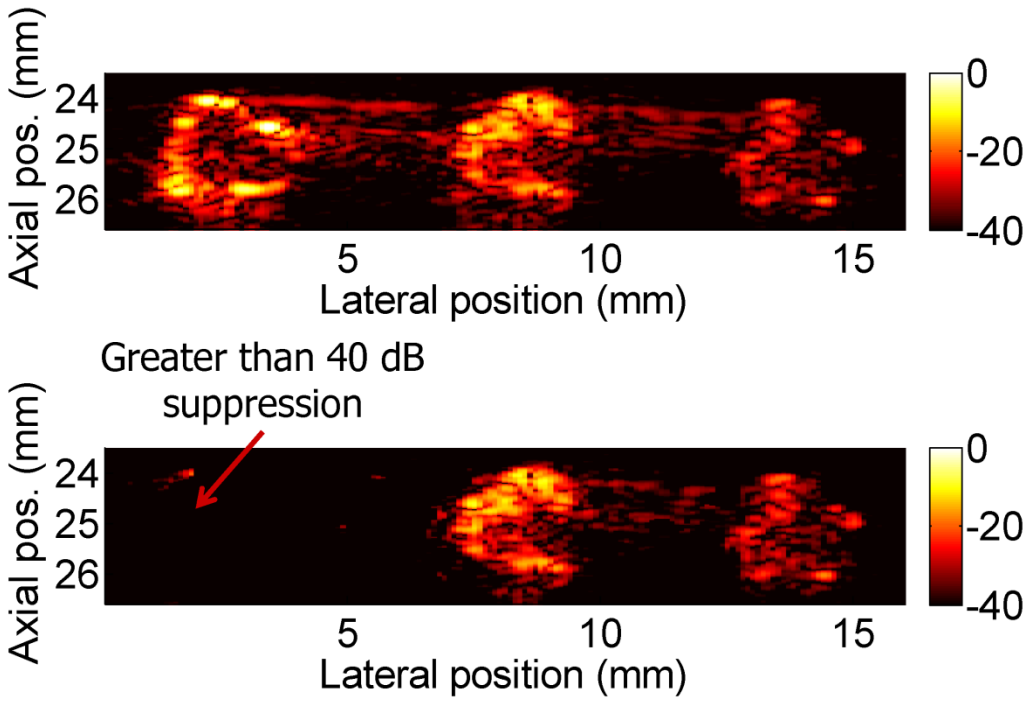

Figure 5.8 Original PA image (upper panel) and motion-enhanced PA image (bottom panel) displayed on a logarithmic scale, where 0 dB represents the brightest signal in the top panel.

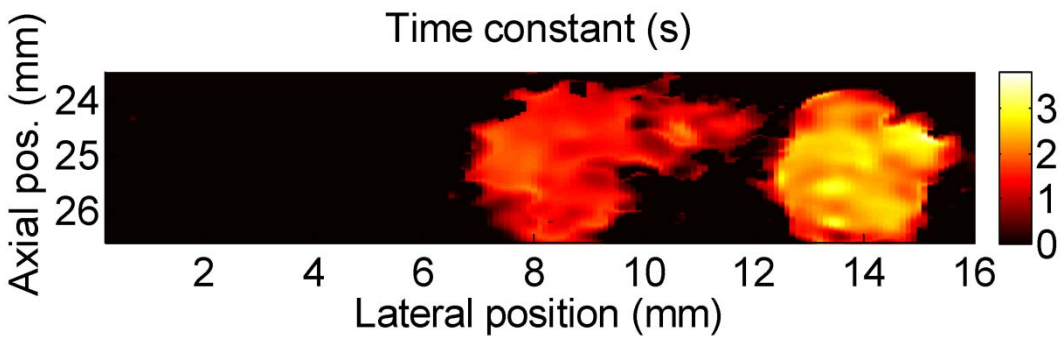

Figure 5.9 Elastic relaxation constants (sec) within the PVA phantom.

5.5 References

[1] A. A. Oraevsky, S. L. Jacques, R. O. Esenaliev, and F. K. Tittel, "Determination of tissue optical-properties by piezoelectric detection of laser-induced stress waves," *Proc. SPIE,* vol. 1882, pp. 86-101, 1993.

[2] L. W. Wang and M. Xu, "Photoacoustic imaging in biomedicine", *Rev. Sci. Instrum.* vol. 77, 041101, 2006.

[3] S. Sethuraman, S. R. Aglyamov, J. H. Amirian, R. W. Smalling, and S. Y. Emelianov, "Intravascular photoacoustic imaging using an IVUS imaging catheter*," IEEE Trans. Ultrason. Ferroelectr. Freq. Control,* vol. 54, no. 5, pp. 978-986, 2007.

[4] S. -W. Huang, J. F. Eary, C. Jia, L. Huang, S. Ashkenazi and M. O'Donnell, "Differential-absorption photoacoustic imaging," *Optics Letters*, vol. 34, no. 16, pp. 2393-2395, 2009.

[5] J. Oh, M. D. Feldman, J. Kim, C. S. Condit, S. Emelianov, and T. E. Milner, "Detection of magnetic nanoparticles in tissue using magneto-motive ultrasound," *Nanotechnology*, vol. 17, no. 16, pp. 4183-4190, 2006.

[6] J. Kim, J. Oh, T. E. Milner, and J. S. Nelson, "Imaging nanoparticle flow using magneto-motive optical Doppler tomography," *Nanotechnology*, vol 18, no. 3, 035504, 2007.

[7]. Y. Jin, C. Jia, S.-W. Huang, M. O'Donnell, and X. Gao, "Multifunctional Nanoparticles as Coupled Contrast Agents," *Nature Materials*, under revision, 2009.

[8] M. A. Lubinski, S. Y. Emelianov and M. O'Donnell, "Speckle tracking methods for ultrasonic elasticity imaging using short-time correlation," *IEEE Transactions on Ultrasonics, Ferroelectrics, and Frequency Control,* vol. 46, pp. 82-96, 1999.

[9] B. J. Fahey, S. J. Hsu, and G. E. Trahey, "A novel motion compensation algorithm for acoustic radiation force elastography," *IEEE Trans. Ultrason. Ferroelectr. Freq. Control,* vol. 55*,* pp. 1095-1111, 2008.

[10] Y. Shi, F. J. de Ana, S. J. Chetcuti and M. O'Donnell, "Motion artifact reduction for IVUS-based thermal strain imaging," *IEEE Trans. Ultrason. Ferroelectr. Freq. Control,* vol. 52, pp. 1312-1319, 2005.

Chapter 6 Conclusions and Future work

6.1 Conclusions and Contribution of This work

The presence of speckle in coherent imaging modalities provides the foundation for US and PA imaging to be applied for non-invasive and quantitative image-based disease diagnosis and therapy. This can be accomplished using a motion tracking algorithm or more specifically a speckle tracking algorithm. The goal of this dissertation is to demonstrate speckle tracking's application to cardiac strain imaging in US imaging and contrast enhancement in PA imaging.

In chapters 2 through 4, we discussed and demonstrated the ability of speckle tracking's application to multi-dimensional cardiac strain imaging. Chapter 2 first showed that with 2-D ST, we can achieve better accuracy than the 1-D TDI method in estimating instantaneous axial normal strain and accumulated axial normal strain. The improvement was demonstrated in simulation using a simulated heart, and experimentally, using an isolated rabbit heart model of acute ischemia produced by LAD artery ligation. Chapter 3 further demonstrated that directional changes in the in-plane principal deformation axes derived from 2-D speckle tracking can locate the region with abnormal motion due to LAD ligation. Furthermore, strains based on principal stretches can characterize heart muscle contractility independent of probe orientation. These two findings were evaluated in a well-controlled 2-D cardiac elasticity imaging technique using two

coplanar and orthogonal linear probes simultaneously imaging an isolated retroperfused rabbit heart. When 2-D speckle tracking is used clinically, it has to be recognized that this method ignores out-of-plane motion in 3-D heart motion. Introduction of commercial 2-D ultrasound probe makes ultrasound 3-D RF data acquisition possible. However, the volume rate of current commercial scanners is not high enough for 3-D speckle tracking. Chapter 4 introduced a LV phantom constructed using PVA cryogel and integrated with a pulsatile pump and a pressure meter. This new system can increase the effective volume rate and overcome the current commercial system's limitation. The performance of 2-D and 3-D speckle tracking was tested on this LV phantom and a simulated 3-D LV.

Chapter 5 illustrated speckle tracking's ability to enhance contrast in PA imaging. As demonstrated in this chapter, motion synchronized with magnetomotive manipulation of Au-shell-encapsulated magnetic nanoparticles can be estimated using 2-D speckle tracking and then used to distinguish the targeted region from the unwanted background region. In addition, the study also showed that mmPA imaging can potentially characterize tissue's elastic properties.

The main contributions of the work presented in this dissertation are summarized below

- The accuracy of TDI and 2-D ST estimates of instantaneous axial normal strain and accumulated axial normal strain using a simulated heart were compared and evaluated.

- Directional changes in the in-plane principal deformation axes and strains based on principal stretches derived for cardiac strain were introduced and evaluated in a well controlled isolated retroperfused rabbit heart.
- A 3-D LV phantom was first constructed using PVA cryogel and integrated with a pulsatile pump and a pressure meter with increased effective volume rate for evaluating 3-D speckle tracking.
- The feasibility of contrast enhancement in a new imaging modality, mmPA imaging, was first demonstrated experimentally.

The work of Chapter 2 was presented at the 2008 IEEE International Ultrasonics Symposium, 7th International Conference on the Ultrasonic Measurement and Imaging of Tissue Elasticity, and has been submitted to the IEEE Transactions on Ultrasonics, Ferroelectrics and Frequency Control.

- C. Jia, R. Olafsson, S.-W. Huang, T. J. Kolias, K. Kim, J. M. Rubin, H. Xie, and M. O'Donnell, "Comparison of 2-D Speckle Tracking and Tissue Doppler Imaging," submitted to IEEE Transactions on Ultrasonics, Ferroelectrics and Frequency Control.
- C. Jia, R. Olafsson, K. Kim, T. J. Kolias, J. M. Rubin, H. Xie, and M.O'Donnell, "2D Speckle Tracking vs DTI-derived Elasticity Imaging on an Isolated Rabbit Heart", 2008 IEEE Ultrasonics Symposium, vol. 1-4 and Appendix, pp. 958-961, 2008.

- C. Jia, R. Olafsson, T. J. Kolias, S.-W. Huang, K. Kim, J. M. Rubin, H. Xie, and M. O'Donnell, “Comparison of 2D Speckle Tracking and DTI on an Isolated Rabbit Heart,” 7th International Conference on the Ultrasonic Measurement and Imaging of Tissue Elasticity, Austin, USA, Oct. 2008.

The work of Chapter 3 was presented at the 2007 IEEE International Ultrasonics Symposium, and has been published in Ultrasound in Medicine and Biology.

- C. Jia, R. Olafsson, K. Kim, T. J. Kolias, J. M. Rubin, W. F. Weitzel, R. S. Witte, S.-W. Huang, M. S. Richards, C. X. Deng, and M. O’Donnell, “Two-dimensional Strain Imaging of Controlled Rabbit Hearts,” Ultrasound in Medicine and Biology, vol. 35, no. 9, pp. 1488-1501, 2009.
- C.Jia, R. Olafsson, K. Kim, R. S. Witte, S.-W. Huang, T. J. Kolias, J. M. Rubin, W. F. Weitzel, C. Deng, and M.O'Donnell, “Controlled 2D Cardiac Elasticity Imaging on an Isolated Perfused Rabbit Heart,” 2007 IEEE Ultrasounics Symposium proceedings, vol. 1-6, pp. 581-584, 2007.

The work of Chapter 4 and related results were presented at the 2006, 2007, and 2009 IEEE International Ultrasonics Symposia, and the 6th International Conference on the Ultrasonic Measurement and Imaging of Tissue Elasticity.

- C. Jia, P. Yan, A. Sinusas, D. P. Dione, Q. Wei, K. Thiele, T. K. Kolias, J. M. Rubin, L. Huang, S.-W. Huang, J. S. Duncan, and M. O'Donnell, “3D Elasticity Imaging on an Open-chest Dog Heart,” 2009 IEEE International Ultrasonics Symposium, Rome, Italy, Oct. 2009.
- C. Jia, P. Yan, K. Kim, T. J. Kolias, J. M. Rubin, W. F. Weitzel, D. Dione, A. J. Sinusas, J. Duncan, and M. O'Donnell, “3D Elasticity Imaging of LV Through Simulations and Phantom Experiments,” 6th International Conference on the Ultrasonic Measurement and Imaging of Tissue Elasticity, Santa Fe, USA, Nov. 2007.
- C. Jia, K. Kim, T. J. Kolias, J. M. Rubin, W. F. Weitzel, P. Yan, D. Dione, A. J. Sinusas, J. Duncan, and M. O'Donnell, “4D Elasticity Imaging of PVA LV Phantom Integrated with Pulsatile Circulation System Using 2D Phased Array,” 2007 IEEE Ultrasonics Symposium Proceedings, vol. 1-6, pp. 876-879, 2007.
- C. Jia, K. Kim, T. J. Kolias, W. F. Weitzel, J. M. Rubin, and M. O’Donnell, “Left Ventricular Phantom with Pulsatile Circulation for Ultrasound Strain Rate Imaging,” 2006 IEEE Ultrasonics symposium, vol.1-5, Proceedings, pp. 1317-1320, 2006.

The work of Chapter 5 was presented at the 2010 SPIE Photonics West, and has been submitted to Nature Materials.

- C. Jia, S.-W. Huang, Y. Jin, C. Seo, L. Huang, J. F. Eary, X. Gao, and M. O'Donnell, "Integration of Photoacoustic, Ultrasound and Magnetomotive System," Proc. SPIE, vol. 7564, 756416, 2010.
- Y. Jin, C. Jia, S.-W. Huang, M. O'Donnell, and X. Gao, "Multifunctional Nanoparticles as Coupled Contrast Agents," Nature Materials, under 2nd review, 2010.

6.2 Future Experiments for Cardiac Strain Imaging

6.2.1 Error Characterization for 3-D Speckle Tracking

One challenging issue with cardiac elasticity imaging is that heart motion is 3-D and complex. Real heart motion is a combination of 3-D translation, deformation and torsion. For example, strain and torsion at the end of systole can be more than 30% [1] and about 13° in humans, respectively [2]. A rotation larger than 4 degrees for a high resolution imaging system will significantly change the speckle pattern. Frame to frame strain larger than 2% causes speckle decorrelation and peak hopping artifacts especially in the areas with large local shear strain. 2-D speckle tracking also suffers from decorrelation since it cannot follow out-of-plane motion. Ideally 3-D speckle tracking can eliminate out-of-plane motion by estimating 3-D motion [3]. However, the displacement estimate accuracy in azimuthal and zenithal directions is worse than that along the beam propagation direction as discussed in Chapter 4. This will eventually affect the accumulated results in three directions at the end of systole. Therefore, it is

necessary to characterize error due to either one of these motions for 3-D speckle tracking.

The simulated 3-D left ventricle [4] discussed in Chapter 4 can decouple complex heart motion to isolate only out-of-plane translation, only physiological 3-D deformation, only torsion, combined motions using two cases (out-of-plane translation and 3-D deformation), and combined motion using three cases. A phased-array imaging system closely matching commercially available cardiac imaging systems will be used to generate 3-D RF data. The performance of 3-D speckle tracking for either simulated case will be analyzed. An optimum tracking and accumulation scheme needs to be established for truly deformation-limited, decorrelation-optimized 3-D speckle tracking.

Validation will be performed in both phantom and animal experiments. 3-D LV phantom integrated with a pulsatile pump described in Chapter 4 provides a well controlled 3-D environment for evaluating 3-D speckle tracking algorithm for pure 3-D translation and combined motion using two simple motions (out-of-plane translation and 3-D deformation). An open-chest dog experiment performed by our collaborators at Yale University will evaluate the tracking algorithm on the combination of three motions. Preliminary studies showed that the positive radial strain (Fig. 6.1 (a)) before occlusion and negative radial strain (Fig. 6.1 (b)) after occlusion were successfully detected three-dimensionally at the anterior wall using 3-D speckle tracking.

6.2.2 Angle Independent Deformation Estimation for 3-D Speckle Tracking

Chapter 3 demonstrated and evaluated the feasibility of angle independent deformation estimation using in-plane principal deformation axes and its corresponding strains based on principal stretches derived from 2-D speckle tracking. This angle independent analysis can also be extended to 3-D case for detecting the contractility of myofibers.

Myocardial tissue has inherent anisotropic mechanical properties because of its myocardial fiber structure as shown in Fig. 6.1. Cardiac fibers are modeled as transverse isotropic in terms of mechanical properties. Some groups have modeled the myocardial fiber as orthotropic considering the sheet structure of the myocardial fiber [5, 6]. In both mechanical models, one of the strains based on the principal stretches is along the fiber direction while the others are in the cross section perpendicular to the fiber direction. During systole, myocardial fibers contract mainly along the fiber direction and LV volume decreases to eject blood. So, the strains based on the principal stretch along the myocardial fiber direction can be used to characterize the contractility of myocardial fibers.

In 2-D speckle tracking, only 3 components of the symmetric strain tensor can be estimated in plane. However, with 3-D tracking, all 6 components of the symmetric strain tensor can be derived since complete spatial displacements can be estimated. Therefore, deformation at one point in the heart wall can be fully characterized by three strains based on the principal stretches along the principal axes independent of coordinate system by calculating the eigenvalues and eigenvectors of the Lagrange strain tensor E as below

$E = \frac{1}{2}(\Omega \begin{bmatrix} \lambda_1^2 & & \\ & \lambda_2^2 & \\ & & \lambda_3^2 \end{bmatrix} \Omega^T - I)$, where Ω is an orthogonal matrix. The column vectors in Ω are eigenvectors representing the principal axes of stretch λ_i (i = 1, 2 and 3).

This hypothesis will be evaluated on an open-chest dog experiment performed at Yale University.

6.3 Future Experiments for Contrast Enhancement in Photoacoustic Imaging

6.3.1 Elasticity Property Characterization and Validation based on Relaxation

As discussed in Chapter 5, mmPA imaging can potentially be used for elasticity imaging since the displaced tissue moves back to its original position subject only to the intrinsic elastic properties after the magnetic field is turned off. Fig. 6.3 shows the relaxation time constant measured from the displacement trace after the magnetic field is turned off in this phantom experiment. The difference in the relaxation time constant between the two inclusions well explained why displacements in the MNP inclusion were slightly greater than those in the MNP-gold hybrid NP inclusion.

To fully explore the capability of mmPA imaging in characterizing tissue elastic properties, a series of PVA phantoms, mixed with a certain MNP-gold hybrid NP, with different elasticity and viscosity needs to be built. Young's moduli and viscosity of these phantoms will be measured in advance using force-

deformation methods. These values will be used to validate the corresponding measurements using mmPA imaging.

6.3.2 Characterization of Motion Response in Complex Motion Environment

Chapter 5 demonstrated that we are able to distinguish PA sources susceptible to an applied magnetic field (e.g., the gold nanorod inclusion) from the unwanted background signal in mmPA imaging in a phantom experiment. The local perturbation due to the interaction between the NPs and the magnetic field is finite in real clinical imaging compared to physiological motion such as cardiac motion and respiration. A challenging issue is how to reduce the interference from these relatively large physiological motions when mmPA imaging is applied clinically.

Robust signal processing methods have been developed to track small induced displacements during physiologic motion in acoustic radiation force impulse (ARFI) imaging [7] and thermal strain imaging (TSI) [8]. Similar to these methods, the PA image acquisition sequence relative to the magnetic field will be synchronized with local main physiologic motion as shown in Fig. 6.4. Theoretically, local motion is proportional to local magnetic field changes and thereby has a linear relationship with cardiac cycles when a corresponding periodic magnetic field is applied. Therefore, the weighted linear least squares fitting scheme can be used to extract the induced motion synchronized with the magnetic field from background physiological motion. This data acquisition

scheme will be evaluated in a PVA phantom periodically compressed by an external force similar to cardiac motion.

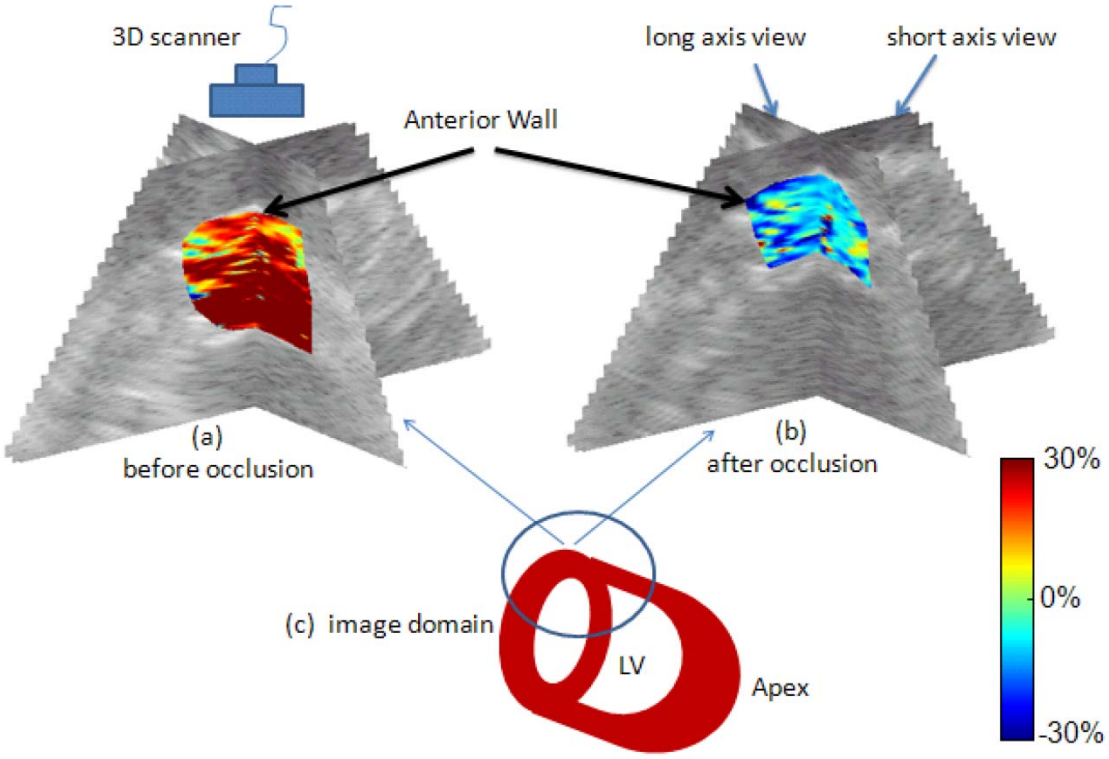

Figure 6.1Radial strain using 3-D speckle tracking before and after occlusion at the end of systole.

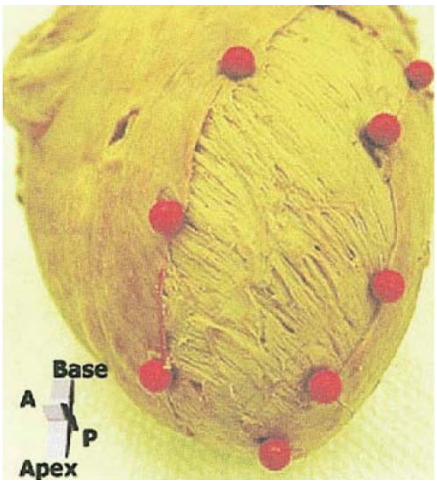

Figure 6.2 Muscle fibers in the left ventricle of an explanted adult porcine heart (adapted from ref. [1]).

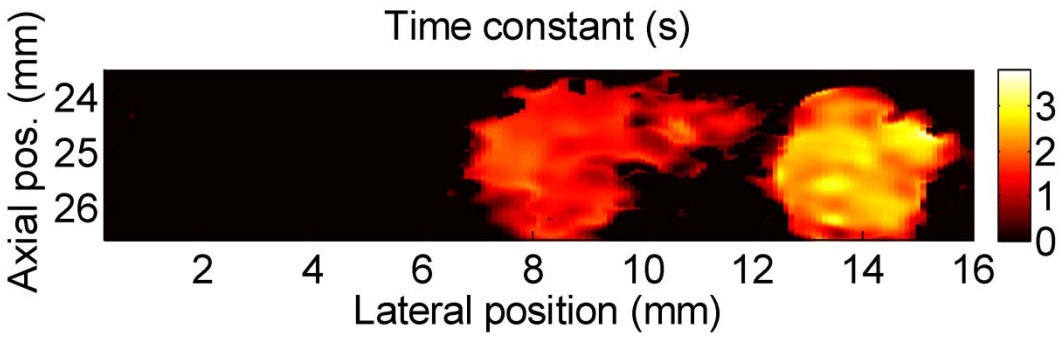

Figure 6.3 Elastic relaxation constants (sec) within the PVA phantom.

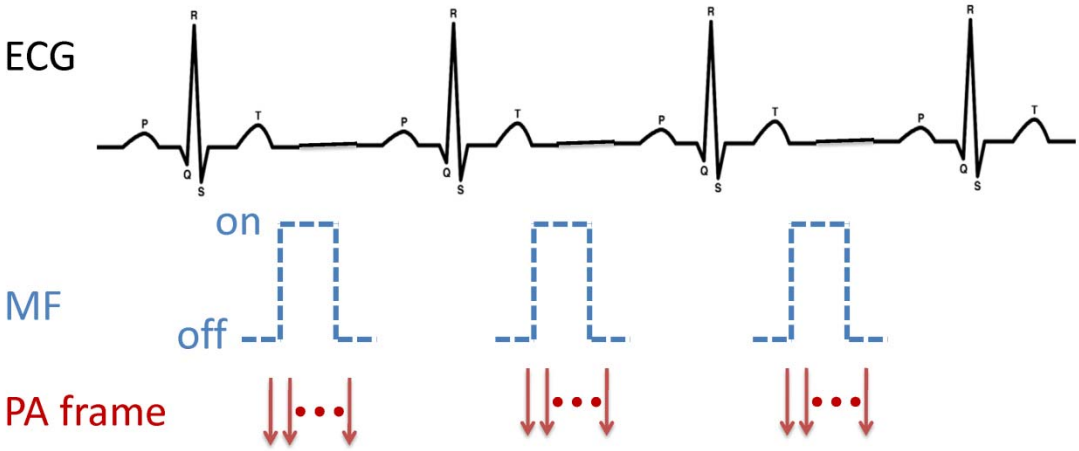

Figure 6.4 PA imaging scheme relative to ECG and magnetic field (MF) to minimize the effects of cardiac motion.

6.3.3 References

[1] P.P. Sengupta, J. Korinek, M. Belohlavek, J. Narula, M. A. Vannan, A. Jahangir, and B. K. Khandheria, “Left ventricular structure and function basic science for cardiac imaging,” J Am Coll Cardiol, vol. 48, pp. 1988-2001, 2006.

[2] R. E. Henson, S. K. Song, J. S. Pastorek, J. J. H. Ackerman, and C. H. Lorenz, " Left ventricular torsion is equal in mice and humans,“ *Am J Physiol Heart Circ Physiol,* vol. 278, pp. H1117-H1123, 2000.

[3] X. Chen, H. Xie, R. Erkamp, K. Kim, C. Jia, J. M. Rubin, and M. O'Donnell, “3-D correlation-based speckle tracking,” *Ultrasonic Imaging*, vol. 27, pp. 21-36, 2005.

[4] X. Chen, X. Li, D. Sahn, K. Kim, H. Xie, and M. O’Donnell, "Evalution of 2-D Speckle Tracking Based on Strain Rate Imaging (SRI) Using a 3-D Heart Simulation Model,“ Proceedings of the 2004 IEEE Ultrasonics Symposium, pp. 2125-2128, 2004.

[5] M. P. Nash and P. J. Hunter, “Computational mechanics of the heart”, *Journal of Elasticity,* vol. 6, pp. 113-141, 2000.

[6] T. P. Usyk, R. Mazhari and A. D. Mcculloch, “Effect of laminar orthotropic myofiber architecture on regional stress and strain in the canine left ventricle”, *Journal of Elasticity*, vol. 61, pp. 143-164, 2000.

[7] B.J. Fahey, S.J. Hsu, and G. E.Trahey, “A novel motion compensation algorithm for acoustic radiation force elastography,” *IEEE Trans. Ultrason. Ferroelectr. Freq. Control,* vol. 55, pp. 1095-1111, 2008.

[8] Y. Shi, F. J. de Ana, S. J. Chetcuti, and M. O'Donnell, “Motion artifact reduction for IVUS-based thermal strain imaging,” *IEEE Trans. Ultrason. Ferroelectr. Freq. Control,* vol. 52, pp.1312-1319, 2005.

Appendix A Principal Stretch and Principal Strain

In continuum mechanics, deformation is often quantified by the deformation gradient tensor $\mathbf{F}$ [1]. It compares the size and shape of material elements in the deformed configuration. Let $\mathbf{x}$ and $\mathbf{X}$ be the coordinates in the reference and deformed configuration, respectively. $\mathbf{F}$ in 2-D is defined as:

$$\mathbf{F} \equiv \begin{pmatrix} \frac{\partial x_1}{\partial X_1} & \frac{\partial x_1}{\partial X_2} \\ \frac{\partial x_2}{\partial X_1} & \frac{\partial x_2}{\partial X_2} \end{pmatrix} = \begin{pmatrix} \frac{\partial u_1}{\partial X_1} + 1 & \frac{\partial u_1}{\partial X_2} \\ \frac{\partial u_2}{\partial X_1} & \frac{\partial u_2}{\partial X_2} + 1 \end{pmatrix}, \tag{A-1}$$

where u_1 and u_2 are the displacement components due to deformation. **F** can be expressed as $\mathbf{F} = \mathbf{RU}$, where **R** is a rotation matrix and **U** is a symmetric deformation matrix. The right Cauchy deformation tensor

$$\mathbf{C} \equiv \mathbf{F}^{\mathbf{T}}\mathbf{F} = \mathbf{U}^T\mathbf{U} \tag{A-2}$$

is independent of rotation and fully characterizes the deformation. $\mathbf{C}$ is a symmetric tensor and can be decomposed as:

$$\mathbf{C} = \mathbf{\Omega}\begin{pmatrix} (\lambda_1)^2 & 0 \\ 0 & (\lambda_2)^2 \end{pmatrix}\mathbf{\Omega}^T \tag{A-3}$$

where

$$\mathbf{\Omega} = \begin{pmatrix} \mathbf{v_1} & \mathbf{v}_2 \end{pmatrix} = \begin{pmatrix} v_{11} & v_{12} \\ v_{21} & v_{22} \end{pmatrix} \tag{A-4}$$

is a unitary matrix, and $\mathbf{v_1}$ and $\mathbf{v}_2$ are the eigenvectors of $\mathbf{C}$ corresponding to the eigenvalues λ_1^2 and λ_2^2, respectively, and orthogonal to each other.

Because all soft tissue is nearly incompressible, $\lambda_1^2 = \lambda_2^2$ holds only if the deformation is small. Therefore, in this study where large deformation is typical, it suffices to consider only $\lambda_1^2 \neq \lambda_2^2$. When $\lambda_1^2 \neq \lambda_2^2$, the eigenvectors are uniquely determined to within a factor of 1 or -1 [1]. In continuum mechanics, λ_1 and λ_2 are defined as principal stretches, and $\mathbf{v_1}$ and $\mathbf{v}_2$ represent the principal axes of these principal stretches. Note that the principal axes defined here are bidirectional. That is, $\mathbf{v_1}$ and $-\mathbf{v_1}$ represent the same axis. A principal stretch represents the length ratio of a segment along the corresponding principle axis in the deformed configuration to its original segment along the corresponding principal axis in the reference configuration. That is, $(\lambda_1 - 1)$ and $(\lambda_2 - 1)$ describe how much the original segment shortens (-) or lengthens (+) along the principal axis directions as a fraction of the original lengths. In this study, we use $(\lambda_1 - 1)$ and $(\lambda_2 - 1)$ to characterize cardiac contractility and the principal axes to characterize contraction direction. We label $(\lambda_1 - 1)$ and $(\lambda_2 - 1)$ as the strains based on the principal stretches along the principal axes. They differ from the principal strains.

The commonly used Lagrangian (Green) strain tensor for finite deformation is:

$$\mathbf{E} = \frac{1}{2}(\mathbf{C} - \mathbf{I}). \tag{A-5}$$

$\mathbf{E}$ is a symmetric tensor and can be also decomposed as:

$$\mathbf{E} = \mathbf{Q}\begin{pmatrix} \varepsilon_1 & 0 \\ 0 & \varepsilon_2 \end{pmatrix}\mathbf{Q}^T. \tag{A-6}$$

where ε_1 and ε_2 are the eigenvalues of $\mathbf{E}$ and are called principal strains. They were proposed for view-independent myocardial strain mapping by Zervantonakis [2].

Comparing (A-3), (A-5) and (A-6) further reveals that strains based on the principal stretches $(\lambda_1 - 1)$ and $(\lambda_2 - 1)$ have the same principal axes as principal strains ε_1 and ε_2. However, in general $\varepsilon_1 = \frac{1}{2}\left((\lambda_1)^2 - 1\right) \neq (\lambda_1 - 1)$ and $\varepsilon_2 = \frac{1}{2}\left((\lambda_2)^2 - 1\right) \neq (\lambda_2 - 1)$.

To understand the physical meaning of these parameters, the deformation at a point in a solid body can be illustrated by an infinitesimal 2-D element at that point (Fig. A-1). $\mathbf{X_1}$ and $\mathbf{X_2}$ are the coordinate's axes for the reference configuration. $\mathbf{v_1}$ and $\mathbf{v}_2$ are the principal axes of this 2-D element in the reference configuration. The original size of this element is L_1 by L_2 along the principal axes. After deformation, the element was reshaped into $(L_1 + \Delta L_1)$ by

($L_2 + \Delta L_2$). The principal axes are rotated into $\mathbf{N}_1$ and $\mathbf{N}_2$ in the deformed configuration, as illustrated in Fig. A-1.

The principal stretches and principal strains at this point are written as

$$\lambda_1 = \frac{\Delta L_1 + L_1}{L_1}$$
$$\lambda_2 = \frac{\Delta L_2 + L_2}{L_2} \tag{A-7}$$

$$\varepsilon_1 = \frac{1}{2}\left((\lambda_1)^2 - 1\right) = \frac{1}{2}\left(\left(\frac{\Delta L_1 + L_1}{L_1}\right)^2 - 1\right) = \frac{\Delta L_1}{L_1} + \frac{1}{2}\left(\frac{\Delta L_1}{L_1}\right)^2$$
$$\varepsilon_2 = \frac{1}{2}\left((\lambda_2)^2 - 1\right) = \frac{1}{2}\left(\left(\frac{\Delta L_2 + L_2}{L_2}\right)^2 - 1\right) = \frac{\Delta L_2}{L_2} + \frac{1}{2}\left(\frac{\Delta L_2}{L_2}\right)^2 \tag{A-8}$$

After rewriting Eq. (A-7), we see that

$$\lambda_1 - 1 = \frac{\Delta L_1}{L_1}$$
$$\lambda_2 - 1 = \frac{\Delta L_2}{L_2} \tag{A-9}$$

As shown in Eq. (A-8), principal strains ε_1 and ε_2 will overestimate or underestimate this fractional change of element length in large strain cases, such as the deformation at the end of systole. Therefore, in this study, we use $(\lambda_1 - 1)$ and $(\lambda_2 - 1)$ to characterize cardiac contractility.

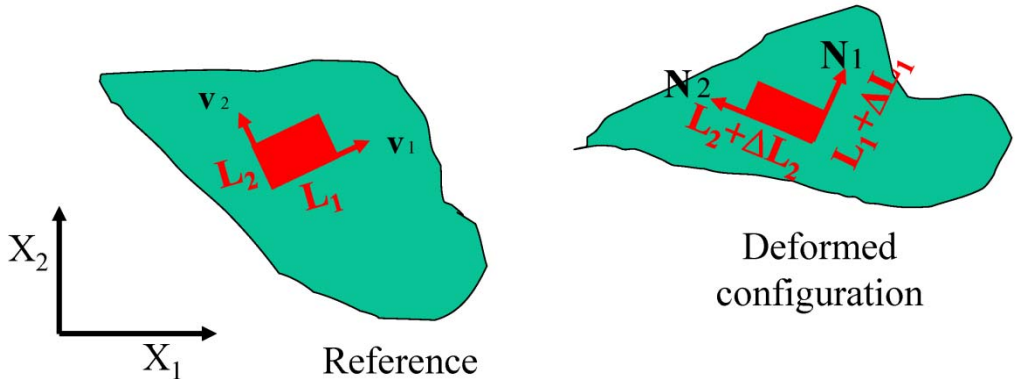

Figure A.1 The deformation of an infinitesimal 2-D element at a point in a solid body illustrated in the reference configuration and deformed configuration. X1 and X2 are the coordinate's axes for the reference configuration. v1 and v2 are the principal axes of this 2-D element in the reference configuration. The original size of this element is L1 by L2 along the principal axes. After deformation, the element was reshaped into (L1 + ΔL1) by (L2 + ΔL2). The principal axes are rotated into N1 and N2 in the deformed configuration.

A.1 References

[1] L. E. Malvern, "Introduction to the Mechanics of a Continuous Medium," 1969.

[2] I. K. Zervantonakis, et al., "A Novel, View-Independent Method For Strain Mapping in Myocardial Elastography: Eliminating Angle- and Centroid-Dependence," Physics in Medicine and Biology, vol. 52, pp. 4063-4080, 2007.

Appendix B Left ventricle Model

The 3-D LV is modeled as an ellipsoid controlled by polate spheroidal coordinates $(\gamma, \theta, \varphi)$ corresponding to the radial, longitudinal, and circumferential directions, respectively[1, 2]. The Cartesian coordinate (x, y, z) can be calculated using the equation

$$\begin{aligned} x &= d\sinh(r)\sin(\theta)\sin(\varphi) \\ y &= d\sinh(r)\sin(\theta)\cos(\varphi), \\ z &= d\cosh(r)\cos(\theta) \end{aligned} \tag{B-1}$$

where *d* is the confocal length and r is a unitless variable. The semi-major axis *b* and semi-minor axis are calculated as

$$\begin{aligned} a(t) &= d(t)\sinh(r) \\ b(t) &= d(t)\cosh(r) \end{aligned}. \tag{B-2}$$

By manipulating the length of two axes at different time instants through a cardiac cycle, LV contraction can be simulated.

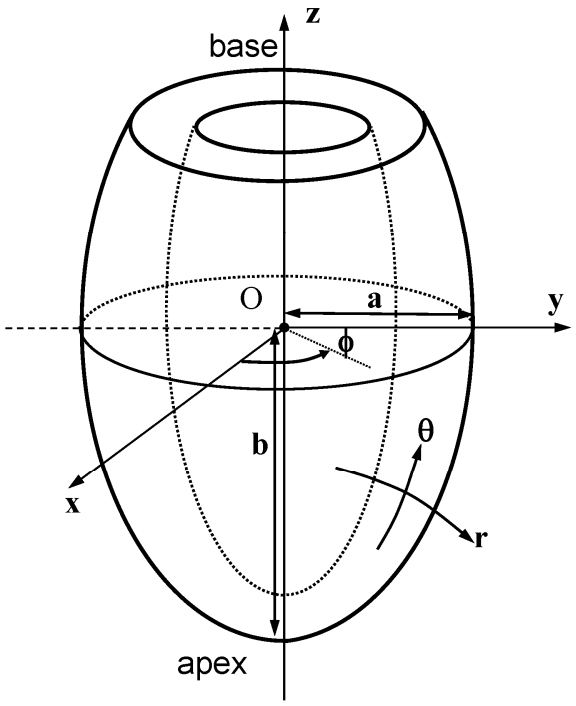

Figure B.1 A sketch of ellipsoidal 3D LV.

B.1 References

[1] S.I. Rabben, A. L. Haukanes and F. Irgens, “A kinematic model for simulat ing physiological left ventricular deformation patterns – a tool for evalu ation of myocardial strain imaging,” *in Proc IEEE Ultrason Symp,* pp. 134-137, 2003.

[2] X. Chen, X. Li, D. Sahn, K. Kim, H. Xie, and M. O’Donnell, “Evalution of 2-D Speckle Tracking Based on Strain Rate Imaging (SRI) Using a 3-D Heart Simulation Model,” *Proceedings of the 2004 IEEE Ultrasonics Symposium*, pp. 2125-2128, 2004.